2007

Activation by Metal Binding of the Anthracis Repressor from Bacillus Anthracis

Kadir Ilker Sen

THE FLORIDA STATE UNIVERSITY

COLLEGE OF ARTS AND SCIENCES

ACTIVATION BY METAL BINDING OF THE ANTHRACIS REPRESSOR FROM *BACILLUS ANTHRACIS*

By

KADIR ILKER SEN

A Dissertation submitted to the
Institute of Molecular Biophysics
in partial fulfillment of the
requirements for the degree of
Doctor of Philosophy

Degree Awarded:
Spring Semester, 2007

The members of the Committee approve the Dissertation of Kadir Ilker Sen defended on Friday, January 12, 2007.

_____
Piotr G. Fajer
Professor co-Directing Dissertation

_____
.
Timothy M. Logan
Professor co-Directing Dissertation

_____
Michael Blaber
Outside Committee Member

_____
Richard Bertram
Committee Member

_____
Hugh Nymeyer
Committee Member

The Office of Graduate Studies has verified and approved the above named committee members.

ACKNOWLEDGEMENTS

First and foremost, my advisors Tim Logan and Peter Fajer deserve my deepest gratitude for being true mentors to me. I am thankful for their patience, guidance, and share of expertise in science and all other aspects of life during the course of my study. I would also like to thank both labs' current and past members, Alla Korepanova, Mariya Semavina, Vedrana Marin, Vijay Rangachari, Wendy Walton, Aga Kasprzak, Nilakshee Bhattacharya, Sumiko Takahashi, Xiaojun Zhang, Nora Hartvig, Likai Song, Mioara Larion, Bruce Bauman, Ken Sale, Regina Stallworth, Tzvetalina Stavreva, Jorge Valdivia, Clement Rouvier, Jean Chamoun, Cecily Oakley, Marco Bonora, Hua Liang, and Brenda Harrison, for their help, support, and friendship.

My acknowledgements extend to the following scientists who had valuable contributions to this work and to my scientific knowledge: Andrzej Sienkiewicz, Brian Bennett, Ewa Bienkiewicz, Michael Blaber, Richard Bertram, and Hugh Nymeyer.

Special thanks to Selda Koydemir, Cengiz Sen, and Ozge Sen for their emotional support and for being there in my times of need.

Finally, I am indebted to my family, Enis, Oya, and Sirma Sen, for the sacrifices they made all these years for my sake. I wouldn't have come so far without their constant encouragement and ever support.

TABLE OF CONTENTS

LIST OF TABLES

LIST OF FIGURES

LIST OF ABBREVIATIONS AND SYMBOLS

°C	Degrees Celsius
3D	three-dimensional
Å	angstrom
Amp	ampicillin
AntR	Anthracis Repressor
B_0	main external magnetic field
C.	diphtheriae Corynebacterium diphtheriae
CW EPR	continuous wave electron paramagnetic resonance
Cα	alpha carbon
DEER	double electron-electron resonance
DNA	deoxyribonucleic acid
DTT	dithiothreitol
DtxR	Diphtheria toxin repressor
E. coli	Escherichia coli
EDTA	ethylenediamine tetraacetic acid aminoethyl ether
EPR	electron paramagnetic resonance
FT	Fourier transform
g_e	g factor of the free electron
HEPES	N-(2-hydroxyethyl)piperazine-N'-(2-ethanesulfonic acid)
IASL	N-(1-oxy-2,2,6,6-tetramethyl-4-piperidinyl)iodoacetamide
IdeR	Iron dependent Repressor
K_D	equilibrium constant
LB	Luria-Bertani
MntR	Manganese Transport Regulator
MSL	N-(1-oxy-2,2,5,5-tetramethyl-4-piperidinyl)maleimide
MTSSL	1-oxyl-2,2,5,5-tertramethyl-Delta3-pyrroline-3-(methyl)methanethiosulfonate
NMR	nuclear magnetic resonance
OD_{600}	optical density (absorbance) at 600 nm
Pdb	protein data bank
R_{scale}	chemical shift scaling factor
SDS	PAGE sodium dodecyl sulfate polyacrylamide gel electrophoresis
SH3	Src homology 3
T_1	longitudinal, spin relaxation time
T_2	transverse, spin-spin relaxation time
UV	ultraviolet
μ_B	Bohr magneton
τ_R	rotational correlation time
ω_e	electron Larmor frequency

ABSTRACT

Anthracis Repressor (AntR) is a Mn(II) activated DNA binding protein that is involved in the regulation of Mn(II) homeostasis in *Bacillus anthracis*. AntR is a member of the Diphtheria Toxin Repressor (DtxR) family of proteins. These proteins function as sensors of intracellular Fe(II) or Mn(II) levels and effect the metal regulated expression of many genes, frequently including virulence related genes. Our studies on AntR focus on metal regulated activation of the protein. We have determined the Mn(II) binding stoichiometry, equilibrium binding constants, and associated kinetic rate constants in AntR using a variety of electron paramagnetic resonance methods. Two divalent manganese ions were observed to bind AntR with positive cooperativity and apparent dissociation constants of 210 ± 18 μM and 16.6 ± 1.0 μM. Binding rates were in the sub-millisecond range, and dissociation rates were characterized by rate constants 35.7 ± 12.1 s^{-1} and 0.115 ± 0.009 s^{-1}. We probed the nature of the metal binding site with EPR for comparison with the crystal structures of homologous manganese transport regulator (MntR) from *Bacillus subtilis*. The spectra were not consistent with a binuclear Mn(II) cluster as seen in MntR structures. Gel filtration, continuous wave EPR, and Pulsed EPR methods were used to investigate possible structural changes in response to metal binding. We found that AntR is exclusively dimeric in absence of Mn(II). Double electron-electron resonance (DEER) was employed to measure spin-spin distance of strategically placed nitroxide spin labels in dimeric AntR. To realize the full potential of DEER, an analysis software with graphical user interface was developed. The data indicated the presence of multiple conformations for each spin label pair in apo-AntR. Metal binding had little effect on these conformations, except near the putative DNA-binding helixes, where metal binding sharpened the distribution of conformers, and decreased the distance between DNA binding regions of AntR dimer. We also showed that the AntR backbone dynamics change considerably upon metal binding. A structure model for AntR was built from homology to MntR, and the experimentally measured distances were simulated. This model only partially agreed with the DEER results, suggesting structural differences between AntR and MntR. These results allow us to develop a model for the Mn(II) induced activation of the repressor

CHAPTER 1
INTRODUCTION

1.1. Study Aims

The main goal of this study is to understand how the Anthracis Repressor (AntR) protein is activated by Mn(II) binding. The pursuit is of particular interest due to the presence of several homologues in pathogenic bacteria, some of which are related to major clinical maladies such as diphtheria and tuberculosis. Our biophysical approach characterizes the thermodynamics of Mn(II) binding and conformational changes associated in the protein during the activation of AntR.

1.2. Iron and Manganese in Bacteria

Iron is an essential element for the growth of bacteria. Average concentration of ferric ions in bacterial cells should at least be about 100 nM for healthy growth and reproduction. Fe(II) is the physiologically relevant oxidation state, however, storage of Fe(II) leads to oxidative damage as Fe(II) oxidizes to Fe(III) *in vivo*. Fe(III) on the other hand, forms insoluble aqua complexes above ~1 nM concentration. In mammals, cytoplasmic proteins store large amounts of Fe(III), and reduce to Fe(II) when required by the organism. Bacteria lack this storage capacity, and have evolved energy driven, high affinity iron uptake mechanisms (Braun, 2001; Braun *et al.*, 1999).

In Gram-negative bacteria, iron uptake is complicated when compared to Gram-positive bacteria due to the presence of an additional lipid bilayer: the outer membrane. Most small molecules pass this barrier via porins. Conversely, iron carrying proteins are generally larger than pore sizes. Iron is acquired at the outer membrane only by specific receptors to iron transporters. For example, heme iron from hemoglobin or myoglobin is acquired via receptors

HpuR and HmbR. Similarly, transferrin and lactoferrin proteins are intercepted with TbpA, TbpB, LbpA, and LbpB proteins (Butler, 2003).

Another iron intake process involves the deployment of low molecular weight, high affinity iron chelators, called siderophores (Braun *et al.*, 1999; Brown *et al.*, 2002a; Ratledge *et al.*, 2000). Siderophores are synthesized inside the bacteria and are secreted for iron scavenging under iron stress conditions. In the host, siderophores chelate iron from transferrins or hemoglobin and transport them to the bacteria. Different types of siderophores are mostly structurally unrelated, however, the most common ones can be grouped into five categories: hydroxamates, catecholates, carboxylates, heterocyclic compounds, and mixed types. For instance, carboxylates group member Carboxymycobactin is an extracellular siderophore that is synthesized in *M. avium*, *M. bovis*, and *M. tuberculosis* (Braun, 2001). FhuA, FepA, and FecA are identified receptors of siderophores in both Gram-negative and Gram-positive bacteria. These are β-barrels possessing strands connected with large loops on the outside of membrane. The channels of these proteins are about three times larger in size than porins.

The process of transferring ferric ions into periplasm is an energy driven process. Nevertheless, there are no energy sources that are immediately available at the outer membrane to the transfer agents. It is thought that protein driven forces supply the energy required. TonB, ExbB, and ExbD in *E. coli*, and similar proteins in Gram-negative bacteria play roles in the transfer of energy from cytoplasmic membrane to outer membrane. A large portion of TonB is present in the periplasm. It has been shown that binding of ferrichrome in vivo increases the formation rate of TonB-FhuA complexes. This and specific interactions between certain residues of TonB and FhuA leads to the hypothesis that the interaction between FhuA and TonB is mediated through the β-barrel on the membrane (Braun, 2001).

When the iron is transferred to the periplasmic area, periplasmic proteins deliver the ion to the receptors at the cytoplasmic membrane. Ferrichrome, for example, is transferred by FhuD in *E.coli*. Unchelated Fe^{+3} is transferred via an ATP-binding cassette (ABC) transporter. Siderophores are generally carried by Fbp's (Ferric ion binding proteins) to the cytoplasmic

membrane. Fbp's belongs to the transferrin super family, and are indeed structurally very similar to transferrins.

The studies on iron uptake are mostly focused on Gram-negative bacteria due to the extra processes and challenges involved. Gram-positive bacteria have very similar systems and high homology at the receptor-transporter proteins (Brown *et al.*, 2002a; Ratledge *et al.*, 2000).

The causative agent of the diphtheria disease, *Corynebacterium diphtheria*, can acquire iron from hemoglobin, hemin, transferrin, and siderophores; basically the same range of substrates as Gram-negative bacteria. Its genome encodes for several different ABC transporters indicating different mechanisms of iron uptake. Among these, iron uptake from hemin and hemoglobin has been studied intensively. An operon consisting of three genes *hmuT*, *hmuU* and *hmuV* is identified in *C. diphtheria* as the encoders of important players in this process. One of the encoded proteins by this operon, HmuT, is a membrane protein that binds hemin and hemoglobin. Following transportation through the cytoplasmic membrane, hemin is degraded by hemin oxygenase, *HmuO*, releasing the ferric ion to cytosol.

The regulator of iron acquisition in *C. diphtheria* is the DtxR (Diphtheria Toxin Repressor) protein. DtxR was initially identified as the inhibitor of Diphtheria Toxin expression. When iron is available, DtxR binds to the *tox* operator and prevents translation of the diphtheria toxin. A number of other genes are also known to be regulated by DtxR (Tao et al., 1992; Tao et al., 1994). These are usually the encoders of the members of iron acquisition system in the bacteria. Hence, the activation and deactivation of DtxR directly regulates the iron uptake. Hemin Oxygenase, for example, is among the proteins that are regulated by DtxR. Others include five separate operons (*irp*1-5) with significant homology to a siderophore uptake system, and a member of the AraC-type transcriptional activators whose products are identified but their roles in the bacteria are unknown. Clearly the regulatory role of DtxR is complex, although the most clear-cut function is the mediation of iron acquisition in bacteria.

A BLAST search reveals a large number of homologues (>100) of the DtxR protein. Among the bacteria that contain DtxR-like proteins are *Brevibacterium lactofermentum, B. linens, Streptomyces lividans, S. pilosus, S. avermitilis, Bacillus subtilis, B. anthracis,*

Mycobacterium leprae, M. bovis, M. flavescens, and *M. tuberculosis.* Homologous sequences can also be found in Gram-negative bacteria such as the Fur protein in *Escherichia coli*, and in a number of extremophilic archaebacteria. Only a few of these proteins are characterized including the Iron Dependent Repressor (IdeR) from *Mycobacterium tuberculosis*, and Manganese Transport Regulator (MntR) from *Bacillus anthracis*.

It seems that against the unfavorable environments where iron is of limited availability, the bacteria have evolved to compensate for their needs. Several pathogens were observed to have no requirement for iron in their metabolism, but need manganese for survival. *B. subtilis* is, for example, one such bacteria which can survive in the absence of iron where manganese is in abundance. Most biological pathways of iron dependent bacteria have mutated to manganese sensitive counterparts in *B. subtilis*. Among the DtxR homologue expressing bacteria, most of the bacterial gene is conserved, despite major differences in metal ion requirements. This extends to the metal ion chelators, and hence leads to a homology between regulator proteins of metal ion homeostasis (DtxR and MntR). These proteins differ slightly in structure and mechanism. DtxR and MntR are the prototypical members representing iron and manganese dependent subfamilies respectively, and are referred to frequently in this study. Following sections summarize previous findings on these repressors.

1.3. Proteins in the DtxR Family

1.3.1. DtxR

The canonical member of the family is DtxR with 226 amino acids and a molecular weight of ~25 kDa. DtxR is a divalent transition metal activated DNA binding protein which represses gene expression downstream of *tox* operator in *Corynebacterium diphtheriae* (Tao et al., 1994). Activation of DtxR protein is achieved by binding of two metal ions per monomer of DtxR to their specific sites. Physiological cation is ferrous ion, however divalent Co, Mn, Ni, Cd and Zn are also reported to bind and activate DtxR in vitro (Tao et al., 1992) with relative affinities $Fe^{+2} \approx Ni^{+2} > Co^{+2} >> Mn^{+2} > Zn^{+2}$. The two metal binding sites are structurally and thermodynamically different, separated by ~ 9 Å (Figure 1-1). One of the sites is absolutely essential for protein's function, whereas the other has minimal affect on activation (Ding et al.,

1996). Once activated, DtxR forms a homo dimer and binds to its recognition site on the genome.

A flexible linker, flanked by a proline rich segment connects the two domains as observed in DtxR's structure (Figure 1-1 A). The C-terminal domain's tertiary structure (Wylie et al., 2003) resembles eukaryotic SH3 domains, however there is no sequence homology. This domain regulates repressor activation by binding the proline rich segment and inhibiting dimer formation in the apo-protein. The C-terminal domain also contributes to metal coordination at the ancillary site in the holo-protein. The N-terminal domain, which is a molten globule in protein's inactive form (Twigg et al., 2001), is responsible for dimerization, DNA binding, and most of the metal binding. The structural data on the apo- and holo- forms of the full length repressor are partly missing and partly controversial. N-terminal domain's crystal structures show very little difference between metal bound and unbound forms of repressor (Qiu et al., 1996) which can not explain why the protein is inactive in the apo- form. Conformational averaging in the apo-protein, revealed by NMR spectroscopy (Twigg et al., 2001), results in broad lines that prevent resonance assignment. Therefore, the exact nature of the apo repressor and the detailed sequence of molecular events from metal binding to active protein are unknown.

The intramolecular regulation of DtxR by specific interaction of the C-terminal domain with the N-terminal domain is of particular interest. A mutation in the C-terminal domain (E175K) is shown to produce a hyperactive protein, which does not require iron for activation, and hence can repress gene expression without allosteric factors. The complete proposed activation scheme of DtxR is summarized in (Figure 1-1 B).

1.3.2. MntR

The majority of DtxR family of proteins contain two domains. However, there is a small subfamily of homologues that have a single domain. Manganese transport regulator (MntR) from *Bacillus subtilis* is the best characterized member of this group (Lieser *et al.*, 2003; Que *et al.*, 2000; Schmitt, 2002). MntR has high homology to N-terminal domain of DtxR, but is selective for Mn(II) rather than Fe(II). The first crystal structure of MntR (Figure 1-2A) shows a dimer interface larger than that of DtxR, extended by an extra helix at the C-terminus. Figure 1-2A also

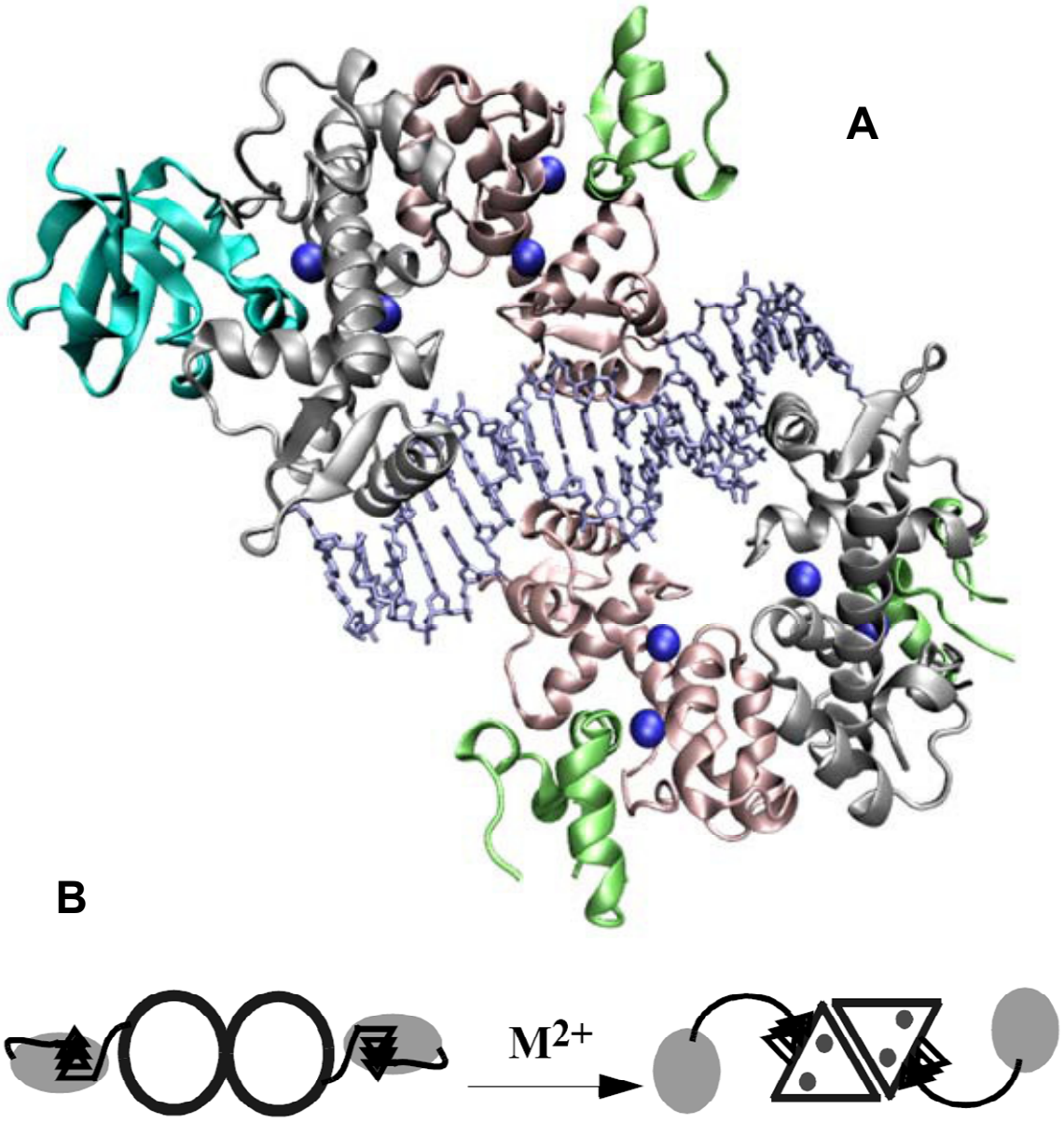

Figure 1-1: Structure of Co activated DtxR bound to its target DNA (A, pdb: 1COW (Pohl et al., 1999)). Two dimers present on opposite sides of the DNA without an evident interaction between dimers. The C-terminal domain is fully resolved in only one monomer and shown in cyan, whereas the partially resolved C-terminal domains are shown in green. The proposed model of activation (B) involves binding of metal ion, which induces interaction of proline rich segment (triangles) with the N-terminal domain, a disordered (black hollow circle) to ordered (triangle) transition in the N-terminal domain, and re-arranging of the C-terminal domain position (grey filled circle (Marin, 2005)).

shows a binuclear metal binding environment rather than two separate sites observed in DtxR and IdeR (Glasfeld et al., 2003). Two residues and a water molecule coordinate both metal ions, which are separated by 3.3 Å. A more recent study (Kliegman et al., 2006) shows a structure where the Mn(II) ions are separated by 4.4 Å (Figure 1-2 B), and report that the conformation of the protein depends on the crystallization conditions. MntR's apo crystal structure also was solved (Smith et al., 2000). The overlaid structures in this study show a multitude of DNA binding domain positioning with respect to the N-terminal. The distance between monomers' DNA binding domain with respect to the dimer interface differs by as much as 1.7 nm between the apo and metal bound forms.

Biochemical analysis on MntR demonstrated aggregation of this protein at concentrations higher than 5 μM and in presence of metal ions Zn(II), Mn(II), and Ni(II) (Lieser et al., 2003). In absence of metal, MntR is found mostly in a dimeric state (Lieser et al., 2003).

1.3.3. AntR

Anthracis Repressor (AntR) is the most recently identified and characterized protein in the DtxR family (Love, 2003). It was cloned from *Bacillus anthracis*, the causative agent of Anthrax. Research on Anthrax disease, the bacteria, and its elements have increased considerably after September 11, 2001, due to the gained consciousness to the rising threat of bioterrorism, although the clinical anthrax has long been feted. Indeed, the first observation of the anthrax disease dates back to 15th century Egypt, where it was identified as an animal disease. Descriptions of human Anthrax were depicted in the literature soon after. The word "Anthrax" is derived from the Greek word for coal. The disease has this name because of the color and appearance of the black eshar on the patient.

B. anthracis is a rod-shaped Gram-positive bacterium. When it enters the host body, spores are produced that are to be phagocytosed by macrophages. Spores then sprout in the phage as vegetative bacteria. This causes the destruction of the host. If the environment does not have the nutrients necessary for spore proliferation, than the spores will remain intact, awaiting for a new host for years to come.

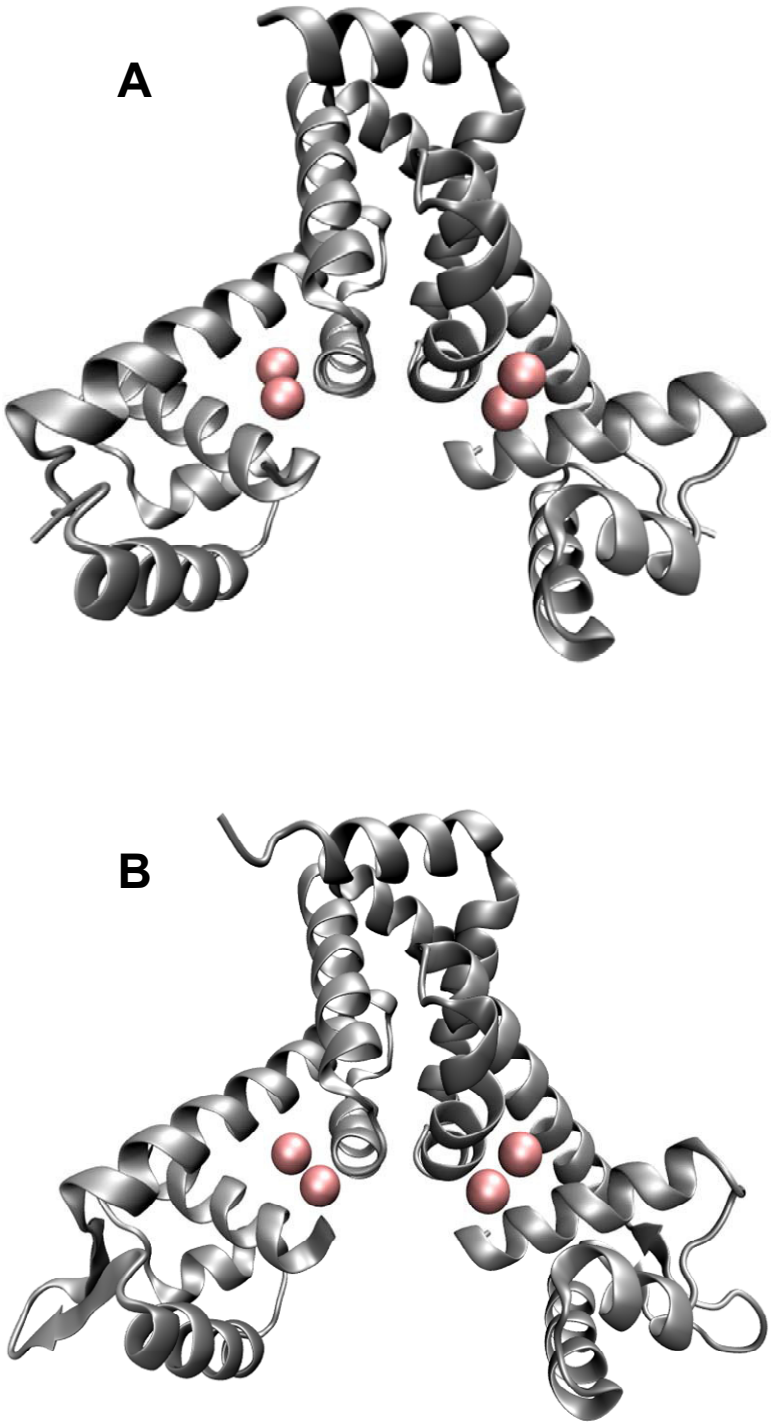

Figure 1-2: Structures of Mn(II) bound MntR, with a binuclear binding site (A, pdb code:10N1 (Glasfeld et al., 2003)) and separate sites (B, pdb code: 2EF1 (Kliegman et al., 2006))

Anthrax toxin is a binary A-B type toxin, where B binds to receptors on the target cell and mediates the entry of A to cell cytoplasm, and A functions only in the cytosol. The protein protective agent (PA, 83 kDa, Figure 1-3 B) is the B unit and A unit is formed by either lethal factor (LF, 90 kDa, Figure 1-3 A) or edema factor (EF, 89 kDa, not shown) proteins. Thus, there actually are two possible forms for toxin: Lethal toxin (LT=LF+PA) and Edema toxin (ET=EF+PA).

The PA protein has four domains: the first contains two calcium binding sites and the cleavage site for activating proteases; the second has a large flexible loop involved in membrane insertion; the third is responsible for heptamer formation; and the fourth domain binds to the receptor on the cell membrane, anthrax toxin receptor protein (ATR). After binding to ATR, PA is cleaved in two by a membrane protease. PA_{20} fragment is released, and PA_{63} fragment oligomerizes, forming $[PA_{63}]_7$ (Figure 1-3 C). This heptamer binds to a maximum of three molecules of LF or EF at its exposed hydrophobic surface, forming either one of the toxins. In fact, LF and EF bind to the interfaces between PA_{63} molecules, making the oligerimization absolutely necessary for pathogenesis. The assembled toxins are endocytosed, and low pH inside the endosomes induces a conformational change at PA_{63}. EF or LF is then released and transferred across the membrane into the cell.

LF is a zinc dependent, four domain, endopeptidase (Figure 1-3 A) which cleaves the N-terminal of mitogen activated protein kinase kinases (MAPKKs). This cleavage leads to fast death of the host. EF on the other hand, is a calcium and calmodulin dependent adenylyl cyclase which floods the cell with cAMP, destroying the balance of intracellular signal pathways, and leading to the malfunction of host defenses. N-terminal domains of both these proteins show sequence homology. This was expected because EF and LF bind to PA via their N-terminus.

The other virulence factor of *B. anthracis* is its poly-D-glutamic acid capsule. The encoding genes for the capsule are found in pX02 plasmid of the bacteria. However, it was shown recently that pX01 plasmid, which normally has the toxin trio encoding genes, strongly affects the capsule formation. It was known that a protein called AtxA regulates the gene expression during infection. The regulation of pX02 plasmid is also mediated by AtxA. This

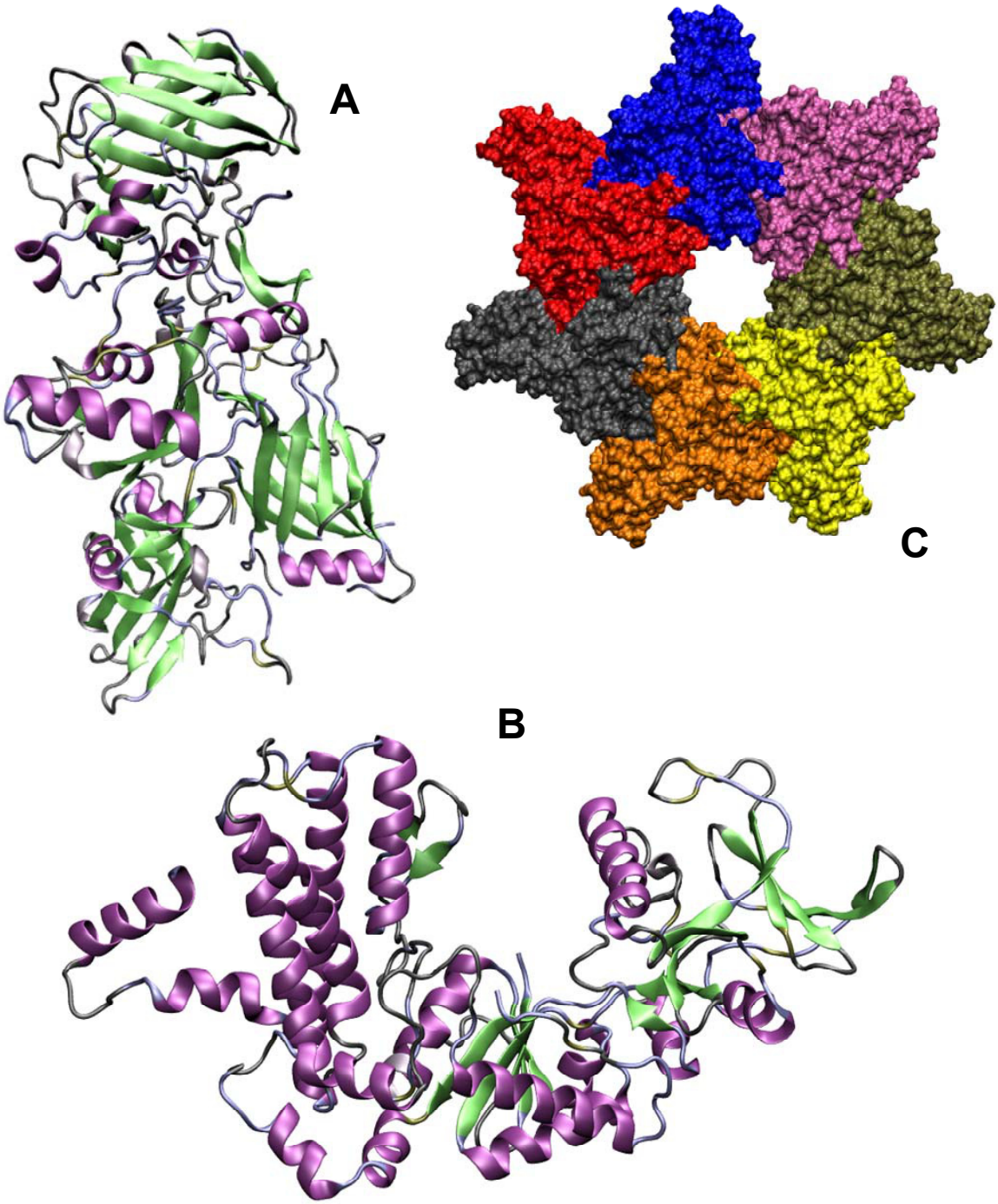

Figure 1-3: LF (A, pdb code: 1ACC (Petosa et al., 1997)), PA (B, pdb code: 1K8T (Drum et al., 2002)), and PA heptamer (C, pdb code: 1TZO (Lacy et al., 2004)) of Anthrax Toxin

indicates the existence of a regulon where AtxA is the regulatory protein acting on genes located on different plasmids. The toxin genes and their trans-activator, AtxA, are expressed within the macrophages after germination.

capA, *capB*, and *capC* genes on pX02 are responsible for the proteinaceous capsule synthesis of *B. anthracis*. *dep* gene is associated with depolymerization of the capsule.The toxins are encoded by genes *cya*, *lef* and *pagA* on pX01. Expression of *capB* is activated by *acpA*, and *atxA* activates the expression of *capB*, *pagA*, *lef*, and *cya*. Very recently, a germination operon gerX located between the pag and atxA genes on pX01 is identified, and analysis of a gerX null mutant indicated that gerX-encoded proteins are involved in the virulence of *B. anthracis*, although the basis is still unknown.

To date, no correlation between the toxicity of *B. anthracis* and the AntR protein is observed. It is postulated that AntR is involved in Mn(II) ion homeostasis because the target operator of AntR is homologous to the *mntH* gene in *B. subtilis,* and *mntH* encodes the Mn(II) transport factors.

There is 82% identity between AntR and MntR proteins, and 89% sequence similarity. Expectedly, AntR is best activated by Mn(II), however, Zn(II) and Co(II) are also observed to activate the repressor (Love, 2003). Ion selectivity of AntR is almost the opposite of DtxR, with relative affinities $Mn^{+2}>Zn^{+2}>Co^{+2}>>Ni^{+2}$. Aside from cloning and in vitro activation studies, no further characterization of AntR was performed prior to this study.

Here, we report manganese and zinc binding affinities to AntR as well binding kinetics (Chapter 3), oligomerization state, distance across monomers in apo and metal bound states, and conformational changes associated with metal induced activation (Chapter 4). The primary technique used is Electron Paramagnetic Resonance (EPR). A theoretical background on the EPR methods used in this work are presented in Chapter 2. Finally, Chapter 5 summarized results and discusses future directions.

CHAPTER 2

THEORETICAL BACKGROUND AND METHODS

We used EPR almost exclusively as the method of analysis for metal binding and conformational change studies. Numerous information can be gained by spectral analysis of conventional continuous wave (cw) experiments on spin labeled proteins, such as correlation times, orientation, and distances between probes in < 2 nm range. Cw EPR has been used extensively for manganese binding studies because of the unique property of Mn(II) discussed in section 2.1.2. For distance measurements, pulsed methods have recently gained popularity due to the long range of sensitivity (< 6-8 nm). In conjunction, cw and pulsed techniques give us an overall perspective in AntR's activation mechanism. In this Chapter, I present a brief overview of EPR theory and methods that are essential for understanding the results presented in this thesis. I start with a discussion of fundamentals of cw EPR, and follow with an introduction to pulsed EPR focusing mainly on the double electron-electron resonance (DEER) experiment, and finally conclude with a description of how the DEER data are analyzed.

2.1. Conventional EPR spectroscopy

2.1.1. Spin Labeled Biopolymers

Spin labels are small molecules that generally have a nitroxide radical attached to a five or six membered carbon ring, and that contain an active site for reaction with the target macromolecule. Usually a cysteine residue is engineered at the desired site on the target biopolymer for the labels' bonding. The commonly used spin labels (SL) are methanethiosulfonate (MTS-), malemide (M-), and iodacetamide (IA-) spin labels. Each have their own unique properties and one has to choose depending on the application. IASL and MSL attach to peptides via covalent bonding of their carbons to cysteine sulfur, whereas MTSSL forms a disulfide bond. Energetically C-S bonds are more stable than S-S bonds and one does not have to worry about the label detaching in the presence of reducing agents such as TCEP (Tris(2-

carboxyethyl)phosphine hydrochloride). On the other hand, in our experience the highest ratio of labeling of AntR is achieved with MTSSL. Molecular sizes are also different between these labels, MSL being the largest with two carbon rings, followed by IASL which has the longest chain. Since the number of rotatable bonds in the chain structure contributes to the spin label anisotropy, for application that requires rigidity, MSL is the best choice with four flexible χ bonds (counting from C_α). MTSSL can take multiple conformations via five bonds, and IASL is the most mobile with six χ dihedral angles. We used all three spin labels on three different sites on AntR for proper distinguishing of backbone heterogeneity from spin label motion.

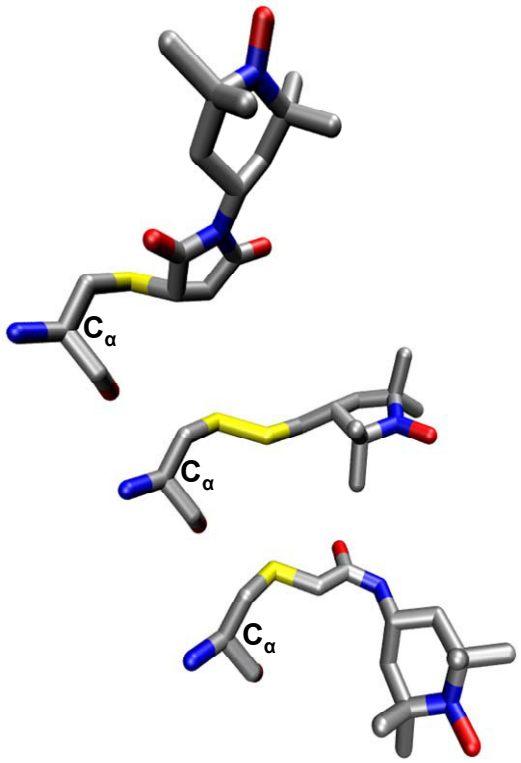

Figure 2-1: Spin label side chain structures. Top to bottom: MSL, MTSSL, IASL

2.1.1.1. EPR Spectra of Nitroxide Spin Labels

The Zeeman interaction of the electron spin (S=½) with the external magnetic field (B_0) is characterized by the g-factor (also referred as Zeeman constant) which relates the angular momentum vector (**S**) to the magnetic moment (**μ**). The unpaired electron of a spin label is found at the 2pπ orbital of the N-O bond. Due to the asymmetric nature of the orbital, the Zeeman interaction is orientation dependent, and hence the g-factor is a tensor of the form:

$$g = \begin{bmatrix} g_{xx} & 0 & 0 \\ 0 & g_{yy} & 0 \\ 0 & 0 & g_{zz} \end{bmatrix} \qquad [1]$$

where the magnetic tensor Cartesian axes system (x, y, z) coincides with the nitroxide principle axis, and is defined with z axis being along the 2pπ orbital and the x axis along the N-O bond. The Effective g-factor of a spin at an arbitrary orientation with respect to the external magnetic field **B** in polar coordinates (θ,ϕ) is given by:

$$g(\theta,\phi) = g_{xx}\sin^2\theta\cos^2\phi + g_{yy}\sin^2\theta\sin^2\phi + g_{zz}\cos^2\theta \qquad [2]$$

Thus, there is a unique orientation (θ,ϕ) of the spin label for every resonance field $B(\theta,\phi)$ in the spectrum (Hemminga et al., 1984). An example is given in Figure 2-2 A. First, an ideal absorption line shape for a system exhibiting all orientations with rhombic symmetry (powder spectrum) was simulated in absence of motion (dotted line). The line shape was then broadened with an arbitrary line width function (solid line). Experimental EPR spectra are the first derivative of the absorption, so the first derivative of the simulated line shape was also shown in Figure 2-2 A (red line). If the system exhibited uniaxial symmetry ($g_{xx}=g_{yy}=g_{\perp}$, $g_{zz}=g_{\parallel}$), we would see two lines instead of three; and if the system was isotropic ($g_{xx}=g_{yy}=g_{zz}=g_{iso}$), we would see a single line as in Figure 2-2 B.

The interaction of the N-O electron spin with the ^{14}N nucleus (I=1) is called the *hyperfine interaction*, and is characterized by hyperfine constant A. This interaction splits each resonance

line into three lines, corresponding to the different nuclear spin manifolds (M_I=-1,0,1). Similar to Zeeman interaction, hyperfine interaction is also orientation dependent and is described by:

$$A = \begin{bmatrix} A_{xx} & 0 & 0 \\ 0 & A_{yy} & 0 \\ 0 & 0 & A_{zz} \end{bmatrix} \quad [3]$$

Consequently, angular dependence in polar coordinates is given by:

$$A(\theta,\phi) = A_{xx}\sin^2\theta\cos^2\phi + A_{yy}\sin^2\theta\sin^2\phi + A_{zz}\cos^2\theta \quad [4]$$

Typically in spin labels, $A_{zz}>A_{xx}\approx A_{yy}$. Figure 2-2 D shows a powder pattern of a system exhibiting rhombic symmetry and anisotropic g and A tensors. Basically, every line in Figure 2-2 C (the case of no hyperfine interaction) is split into three components. At the center of the spectrum some of these features overlap, and cause a challenge in extracting parameters from spectrum.

Thus both g and A tensors give information regarding the orientation of the spin label with respect to the magnetic field. In addition, A is also sensitive to the local environment since a polarity in the medium will alter the partial charges on N and O, affecting the 2pπ orbital of N-O bond. In systems where motion (diffusion) is present, the orientation dependent interactions (g and A) are averaged (McConnell, 1958). Since every orientation results in a different resonant field position, an exchange between possible orientations is considered, with the exchange frequency being the rotational correlation rate ($1/\tau_R$, where τ_R is the rotational correlation time). For instance, let us consider two such spins, oriented so that they resonate with frequencies ω_1 and ω_2 ($\Delta\omega= \omega_2-\omega_1$). In case of slow motion ($1/\tau_R<<\Delta\omega$) the resonances are sharp and separate (Figure 2-3 A). As the correlation rate of motion approaches the frequency difference between the sites ($\Delta\omega$), the resonances broaden, and $\Delta\omega$ decreases (Figure 2-3 B-C). When the exchange rate is moderately fast ($1/\tau_R>\Delta\omega$), the peaks collapse into one broad resonance (Figure 2-3 D). In the fast motion limit ($1/\tau_R>>\Delta\omega$), all anisotropy is averaged, and a single sharp resonance line is observed (Figure 2-3 E)

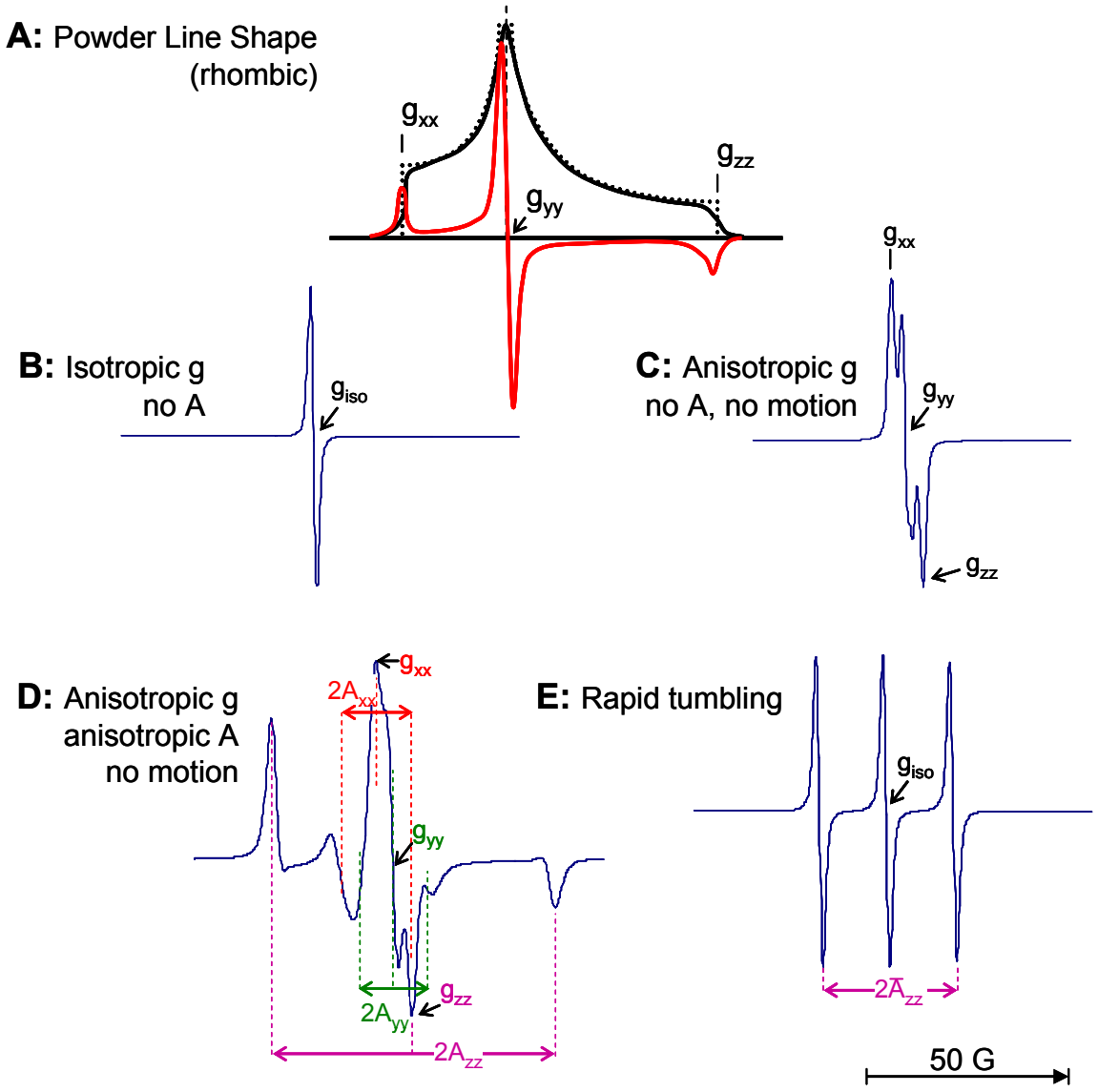

Figure 2-2: Simulated line shapes of spin label continuous wave spectra. **A**: An idealized absorption line shape for a randomly oriented system with rhombic symmetry and no hyperfine coupling (dotted line) is broadened line width (solid black line). EPR spectrum is the first derivative of this line shape (red line). **B**: EPR line shape of a system exhibiting isotropic g tensor without hyperfine interaction. Note that a system with anisotropic g but exhibiting rapid tumbling would also yield this spectrum. **C**: Similar to **A**, an anisotropic system was simulated with typically found nitroxide g tensor values and no hyperfine coupling. **D**: System exhibiting anisotropic g and anisotropic A in slow motion. **E**: In case of rapid motion, g and A anisotropies are averaged, yielding sharp lines as shown. The spectra in B-E were simulated using WinMOMD (Khairy et al., 2006) with parameters: g_{xx}=2.0027, g_{yy}=2.006, , g_{zz}=2.0088, A_{xx}=A_{yy}=7.5 G, A_{zz}=35.5 G, rotational correlation time of 0.1 ns (B and E) and 10 µs (C and D), ν=9.6 GHz, B_0=3420 G, w_{xx}=w_{yy}=w_{zz}=0.5, gib_0=1.3 G

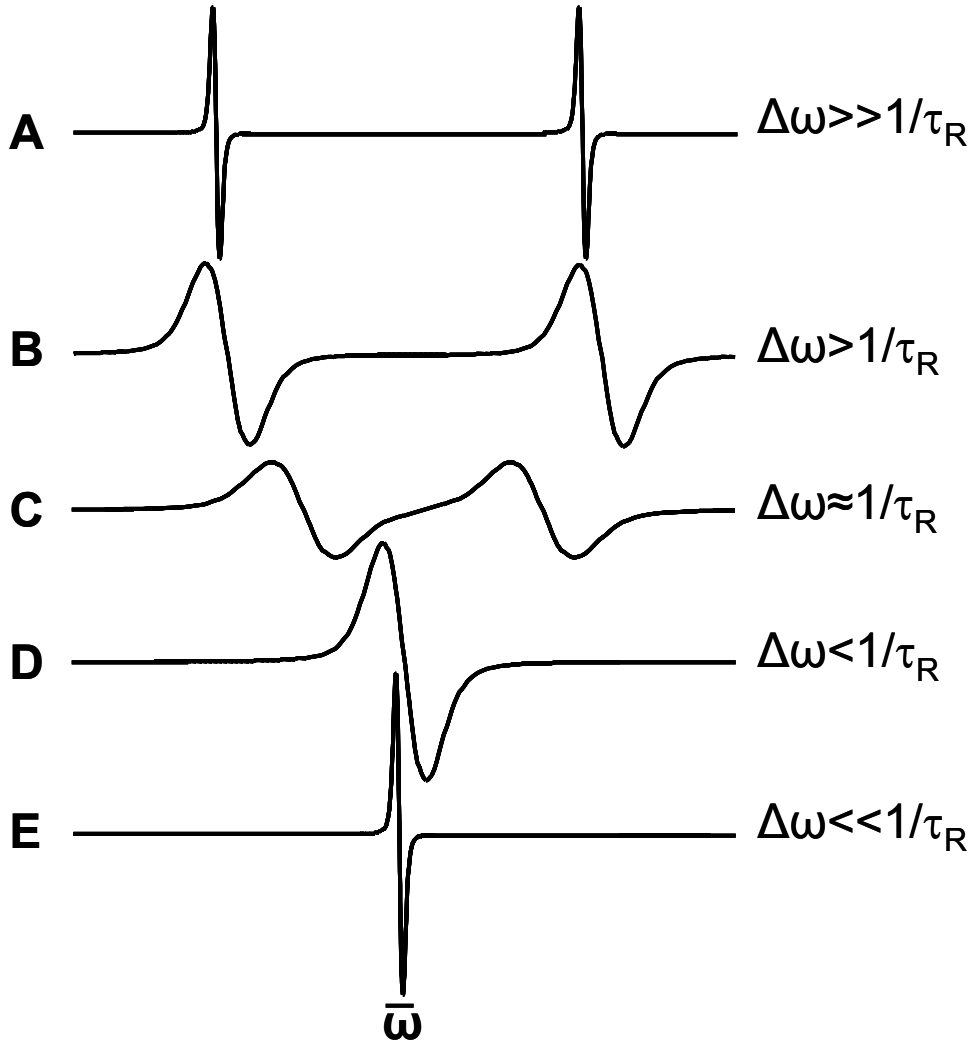

Figure 2-3: Demonstration of exchange interaction between two sites (McConnell, 1958). When the exchange frequency ($1/\tau_R$) is significantly smaller then the resonance frequency difference ($\Delta\omega$), the resonances are unaffected by each other (A). As the exchange frequency approaches $\Delta\omega$, first the individual peaks broaden (B), their resonance frequency changes (C), and eventually collapse into one broad peak (D). Faster exchange narrows this resonance (E). Line shapes are adapted from (Levitt, 2001).

2.1.1.2. Cw EPR Spectra Analysis

Magnetic properties of a spin system can be estimated from cw spectrum via computer simulations of the line shapes. These parameters include anisotropic g and A tensors, axis dependent rotational correlation times, Lorentzian line width denoting homogenous broadening, and Gaussian inhomogeneous broadening. In cases where the spin label motion is restrained by the protein, coefficients describing the volume of allowed diffusion (orienting potential) could be incorporated into the line shape model. Furthermore, when the nitroxide principle axis does not coincide with the magnetic of diffusion axes, Euler angles for the tilt could also be included in simulations. Even in the absence of motion, most of the information that can be gathered from a spin label EPR spectrum are overlapped at the center feature of the spectrum (Figure 2-2 D). In real cases, lines are usually broadened by relaxation effects, Heisenberg spin exchange or dipolar interactions between close unpaired electrons, hyperfine interactions with nearby hydrogens, and presence of multiple conformations of the spin label side chain in the sample (different "sites"). The line shape is complicated by partially averaged rotational diffusion (which could also be anisotropic). Overall, a computer simulation may involve up to 27 parameters with high covariances in order to describe a certain spectrum for a single site. Moreover, some samples may exhibit two or three sites. For optimal analysis of spin labeled AntR spectra (Chapter 4), we employed initial optimization of g and A tensors, followed by rotational correlation time, and Gaussian and Lorentzian line widths. Addition of more variables (orienting potentials, Euler angles) did not improve the fits, although fitting with two sites exhibiting different diffusion rates was employed for most samples. To calculate g and A tensors, the spin labeled protein samples were complexed with diisothiocyanate (DITC) glass beads, and rotational motion of the protein was eliminated. Proteins bind irreversibly to DITC beads via lysine residues, and thus only the spin label motion and backbone dynamics effects are present in the EPR spectra. The g and A parameters extracted from these spectra were used in fitting solution spectra of the same samples. In some cases minor adjustment in the hyperfine tensor was necessary, but otherwise, the tensors were kept constant through samples of same spin labels.

2.1.2. Mn(II) Bound Complexes

In gaseous state, Mn(II) has five unpaired electrons in each 3d orbital, spherically distributed, and energetically degenerate. When the ion is coordinated, the degeneracy is removed and the electrons localize depending on the coordination field geometry and binding strength. In water and most proteins, the ligand field is octahedral, and Mn(II) is found in its high spin S=5/2 state. Coordination removes the degeneracy of the d-orbitals, creating a splitting in the energies between ±5/2, ±3/2, and ±1/2 states in absence of external field. This is called zero field splitting (zfs), and depending on the symmetry of coordination, it may dominate over other terms contributing to the spin Hamiltonian of Mn(II). Proteins usually have non-ideal coordinating sites. Consequently, when Mn(II) is bound to a protein, its room temperature EPR signal disappears due to a broadening via the zfs splitting arising from the disturbances in octahedral ligand field of the bound metal (Figure 2-4). This effect is commonly used to characterize Mn(II) binding to proteins. In frozen samples, zfs does not dominate the spectra and the signal may be recovered. In a typical Mn(II)·6H_2O EPR spectrum at X-band (Figure 2-4), interaction of manganese electrons with ^{55}Mn nucleus results in a six line hyperfine splitting of the electronic transition. Without a strong zfs or exchange interaction, the Mn(II) spectrum is centered around g ≈ 2.005, spanning nearly 700 G.

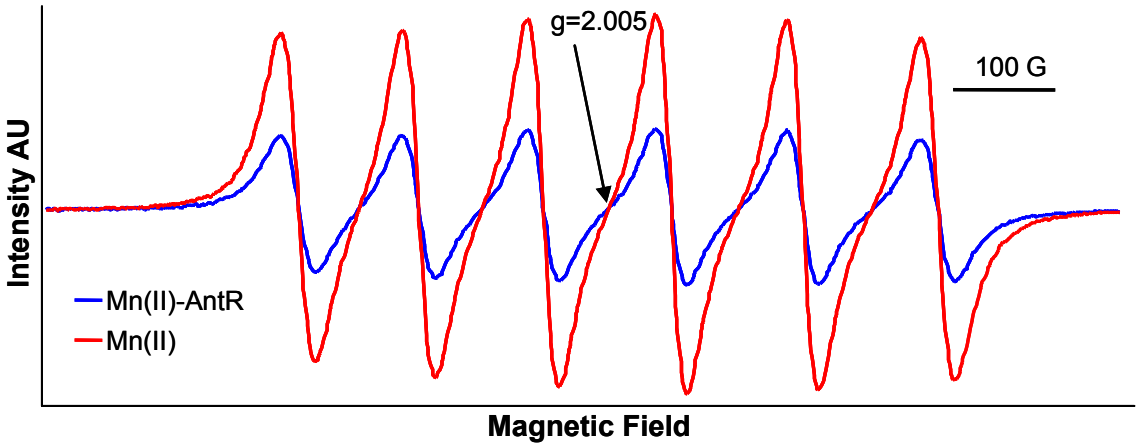

Figure 2-4: Mn(II) signal and the effect of protein coordination. $MnCl_2$ dissolved in 10 mM Hepes, 500 mM NaCl, pH 7.0 (red) signal decreases when AntR is added to the sample at room temperature (blue). The intensity decrease is linear in coordinated manganese concentration, and hence is used to calculate binding stoichiometry.

2.1.3. Experimental Methods

All room temperature (T=293 K) experiments were performed with Bruker EMX series spectrometer (Bruker Biospin, Billerica, MA) equipped with TE_{102} rectangular cavity. Samples were transferred to 50 μL glass capillaries (VWR International, PA) and sealed. At lower temperatures, all samples were transferred into protein buffer containing 30% Ethylene Glycol for cryo protection and glass formation. Ethylene glycol is commonly used with protein samples, and does not inhibit metal binding. 100 μL of each sample was transferred to 4 mm O.D. 3.2 mm I.D. quartz capillaries, and fast frozen by dipping into liquid nitrogen before inserting into the pre cooled resonator. Pulsed EPR spectra were recorded on Bruker Elexys 680 spectrometer equipped with a Bruker dielectric ring resonator (model MD-5).

2.1.3.1. Spin label Methods

Spin labels possess a stable unpaired electron in the N-O 2pπ orbital. Due to the nature of the tether that attaches the nitroxide to the reactive residue on the protein, spin labels have intrinsic mobility that effect the EPR spectra. In order to distinguish backbone and spin label motion, we used three spin labels that differ in tether length in AntR labeling: MTSSL, MSL, and IASL. Their structures are shown in Figure 2-1. Spin labeling of purified protein was carried out by incubating at room temperature (T=293 K) overnight at four-fold molar excess over 500 μM AntR monomer in 10 mM HEPES, 500 mM NaCl, pH 7.0). Unreacted label was removed by dialysis against 4 L protein buffer, replacing three times in 4-6 hour intervals.

Experimental parameters for spin labeled samples' continuous wave EPR spectrum acquisition were as follows: 9.6 GHz microwave frequency, 2 mW microwave power, 1 G modulation amplitude, 100 kHz modulation frequency, 41 ms conversion time, 41 ms time constant, and 1024 points acquisition within 120 or 200 G field sweep.

The efficiency of labeling was calculated from spin concentration determined from the second integral of EPR spectra using free spin label standards of known concentration, and from protein concentration determined by UV absorption at 276 nm using predicted extinction

coefficient of 18450 M^{-1} cm^{-1}. Typical spin labelings were ~98% for MTSSL, ~95% for MSL, and ~90% for IASL. AntR124C was the only construct that was : MSL and MTSSL.

2.1.3.2. Manganese Methods

Stock solutions of $MnCl_2$ and $ZnSO_4$ (Sigma-Aldrich, St. Louis, MO) were prepared in Chelex (Biorad Inc.) treated, degassed protein buffer immediately before using. Titration for binding curve was performed by direct injection of $MnCl_2$ from 5 mM stock solution into 2.5 mL of 71 μM AntR in 4-20 μL increments. Cw EPR spectra were recorded within 2 minutes of mixing. Equilibrium competition experiments with Zn(II) were performed similarly; 0-400 μM Zn(II) was titrated into AntR·Mn sample containing 18.5 μM AntR and 500 μM Mn(II). Spectra were recorded at 9.6 GHz, using 10 mW microwave power, 10 G modulation amplitude, 100 kHz modulation frequency, 41 ms conversion time per point, and 41 ms time constant at T=293 K.

For low temperature acquisitions, Mn(II) bound AntR was prepared by mixing 1:1.85 AntR to Mn(II) molar ratio at 300 μM AntR concentration and by incubating for half an hour at room temperature before freezing. Zn(II) bound samples were prepared similarly but by using 1:4 AntR to Zn(II) ratio.

$[(Me_3TACN)_2Mn(II)(l\text{-}OAc)_3]BPh_4$, a model compound containing a Mn(II)-Mn(II) binuclear cluster, was a gift of Dr. K. Wieghardt (Mülheimer Max-Planck-Institute, Germany). The powder was dissolved in dry, oxygen free 50:50 CH3CN:DMF, transferred to quartz EPR tubes in an argon filled glove box, and flame sealed. Spectra of the model compound and Mn(II) bound AntR were recorded at several temperatures between 10 K and 70 K using microwave power of 0.02-0.2 mW, modulation amplitude of 5 G, modulation frequency of 10 kHz, time constant of 40 ms, and conversion time of 81 ms per point . Background from the dielectric resonator was recorded at these temperatures with protein buffer in 30% ethylene glycol as present in the protein sample, and subtracted from manganese spectrum.

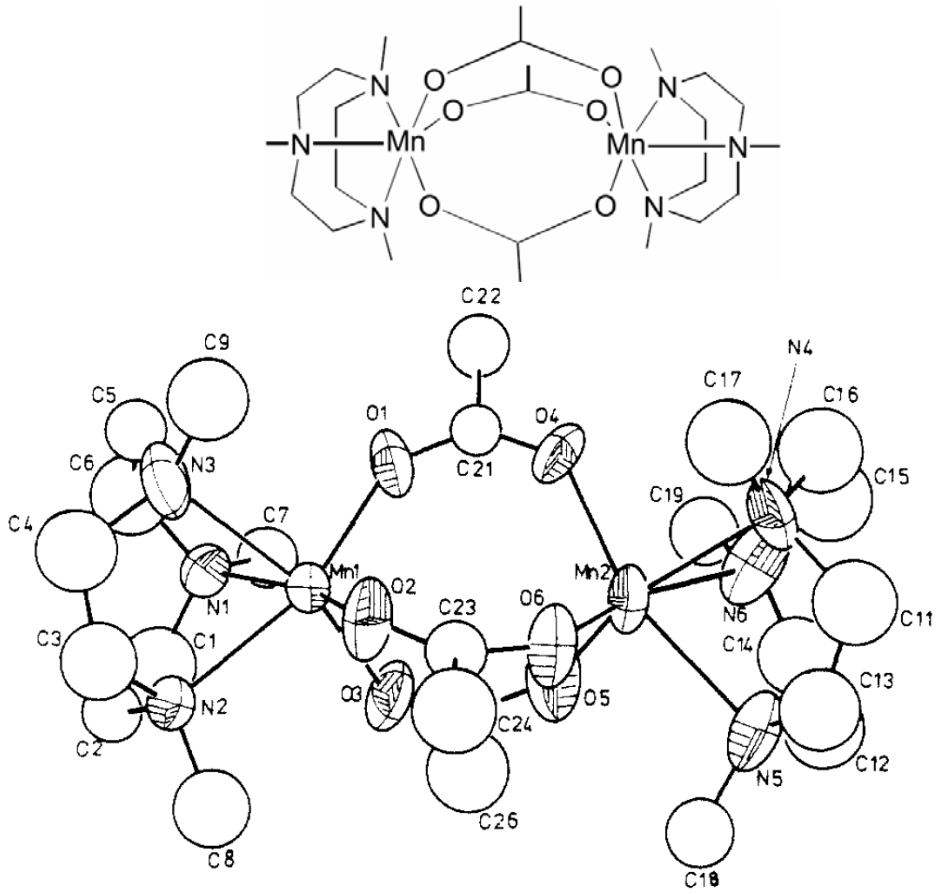

Figure 2-5: Schematic representations of the dimanganese compound[$(Me_3TACN)_2Mn(II)(l\text{-}OAc)_3$]$BPh_4$ adapted from top: (Golombek *et al.*, 2003), bottom: (Wieghardt *et al.*, 1988).

2.1.3.3. Stopped Flow EPR

The stopped-flow interface to the Bruker EMX spectrometer consisted of Model 1100 Syringe Ram and Model 715 Syringe Controller (Update Instruments, Inc., Madison, WI). A home-built dielectric resonator (Sienkiewicz et al., 1999) was affixed with the Wiskind mixer (a T-jet mixer followed by a grid mixer; also from Update Instruments). The dead volume of the assembly was estimated from construct to be ~ 3 μL.

One 6 mm I.D. glass syringe was loaded with Mn(II) saturated AntR solution (175 μM AntR, 750 μM $MnCl_2$) in protein buffer (10 mM HEPES, 500 mM NaCl, pH 7.0), and an identical syringe with $ZnSO_4$ (750 μM or 1500 μM) freshly prepared in the same buffer. For each transient, 60 μL from each syringe was injected into the mixer at 600 μL/s. To minimize

spectral artifacts arising from mechanical instabilities in the mixing chamber, all the original rubber O-rings attached to the syringe pistons were replaced by custom-made Teflon seals (Figure 2-6).

Magnetic field was fixed at the lowest field Mn(II) transition, and kinetic transients were recorded during and after flow with 2 mW microwave power, 9.52 GHz microwave frequency, 10 G modulation amplitude, 100 kHz modulation frequency, 5.12 ms time constant, 5.12 ms conversion time per point, and 8192 acquisition points. At the end of each kinetic experiment, cw EPR spectra of AntR-Mn-Zn were collected 30, 60, and 120 minutes after the mixing to ensure binding-dissociation equilibrium.

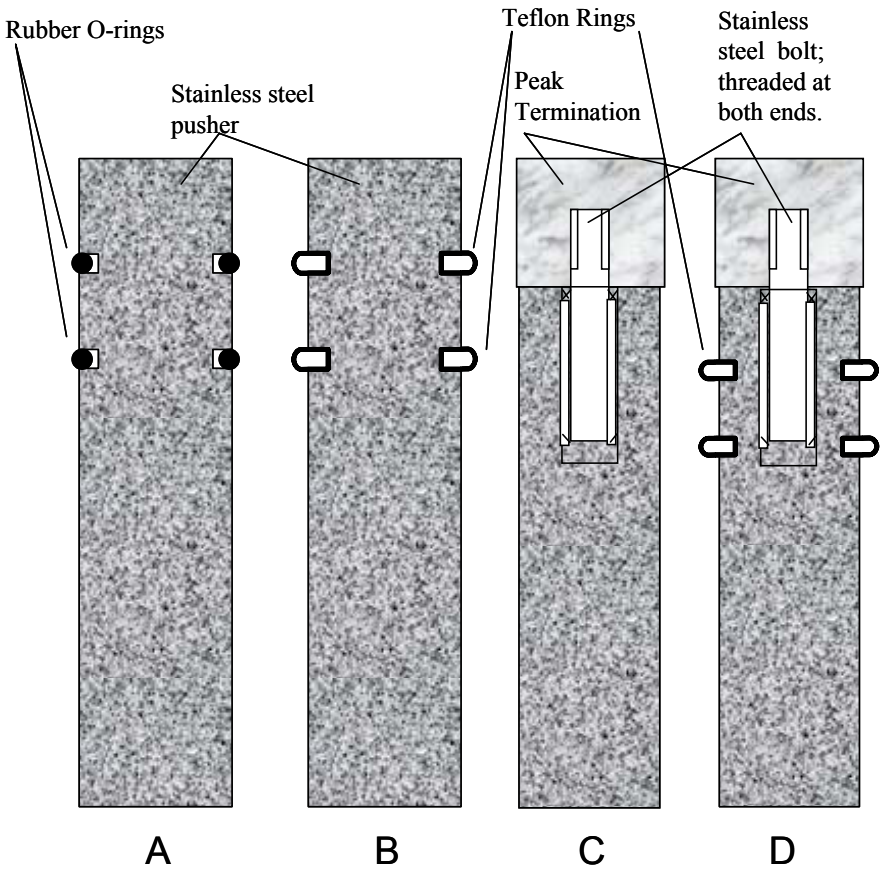

Figure 2-6: Design of new plungers for stopped flow syringes. Manufacturer provided steel plunger with rubber o-rings is shown in A. Fabricated plungers shown in B and C are more durable, but suffer from short lifetime or leaking. Dual Teflon rings and a peak termination as shown in D (designed by Dr. Andrzej Sienkiewicz and produced in National High Magnetic Field Laboratory, Tallahassee, FL) makes a durable plunger and has low friction.

2.2. Pulsed EPR

2.2.1. General Aspects of Pulsed Spectroscopy

Due to the recent developments in microwave electronics, pulsed EPR spectroscopy has gained popularity within the past decade (Schweiger *et al.*, 2001). There are several advantages of using pulsed EPR rather than continuous wave: resolution of high frequency interactions (eg. interactions between electrons and nearby paramagnetic nuclei are ~1-15 MHz, and are inhomogenously broadened in cw line shape) can be achieved with pulsed experiments (e.g. ESEEM and HYSCORE). When of measuring distances, the information obtained via pulsed experiments spans a longer range than in cw EPR. The dipolar coupling could be separated from other interactions in the spin system by a double electron-electron resonance (DEER) technique (Milov et al., 1984). Improving sensitivity by dead time elimination was established with a 4-pulse variant of DEER (Pannier et al., 2000), and model free data analysis have recently been reported (Jeschke et al., 2002). In this work, the optimal parameters for our instrument were standardized, and a model dependent method was interfaced with statistical error analysis. Below, the details of the experiment, practical considerations, and the analysis method are described.

2.2.2. The DEER Experiment

Distances in the range of 2 to 8 nm can be measured with the 4-pulse DEER experiment by isolating the dipolar interaction between two electrons. This is established by exciting two separate populations of spins in a sample, using two pulses at different frequencies ν_0 and ν_1 (Figure 2-7) as detailed below.

Initially, the external magnetic field B_0 is along the z-axis, and all spins are aligned producing the net magnetization $\mathbf{M}=M_z$ at the rotating frame of reference (Figure 2-7 A1). At time $t=0$, the microwave pulse with frequency ν_0 is turned on. Maximum pulse bandwidth is limited, and only a portion of the absorption spectra can be excited by ν_0. The spins that are resonating with this frequency are called A-spins. These spins experience a torque along the axis

orthogonal to the M_z and B_1 vectors which rotates the magnetization as long as the B_1 field is present. The pulse is characterized by the total resulting rotation angle and the direction at which the pulse is applied. For example, an electromagnetic pulse applied along the x-axis which rotates the magnetization by 90 degrees is referred as a $(\pi/2)_x$ pulse.

Immediately after a $(\pi/2)_x$ pulse is applied at frequency ν_0, the magnetization vector is oriented along the -y axis (Figure 2-7 A2). The local magnetic field experienced by each spin differs slightly due to inhomogeneous broadening (mostly caused by unresolved hyperfine interactions) and leads to a resonance offset (Figure 2-7 A3). After a certain time -characterized by T_M relaxation- the spins loose their coherence completely and the magnitude of overall magnetization vector on the xy plane averages to zero. A second pulse, $(\pi)_x$, is applied at $t=\tau$ (Figure 2-7 A4), which reverts the resonance offset of each spin(Figure 2-7 A5), and restores the coherence at exactly $t=2\tau$ (Figure 2-7 A7). At this point an echo is formed, which is later ($t= 2\tau+T$) refocused by another $(\pi)_x$ pulse (Figure 2-7 A10). The refocused echo at $t=2\tau+2T$ (Figure 2-7 A12) is our observation point. The intensity of the echo depends on many factors such as the relaxation times, the delay times τ and T, and the number of excited spins. The refocused echo intensity is smaller than the primary echo because of spin-spin relaxation and spectral diffusion. In case of dipolar interactions, the echo intensity also depends on the strength of dipolar coupling, which is related to the distance between the spins, and hence is of interest. In order to quantify this interaction, the spin system is manipulated by applying a fourth "pump" pulse $(\pi)_x$ at a different frequency ν_1 (Figure 2-7 A8) between the two $(\pi)_x$ pulses along ν_0. When ν_0 and ν_1 are adjusted so that the excitation widths do not overlap, this pulse excites a different population of spins (B-spins) than the initially excited (A-spins). Consequently, the magnetization of B-spins is inverted, and the local magnetic field experienced by the A-spins due to dipolar interaction changes its sign. The dipolar coupling is therefore not completely refocused.

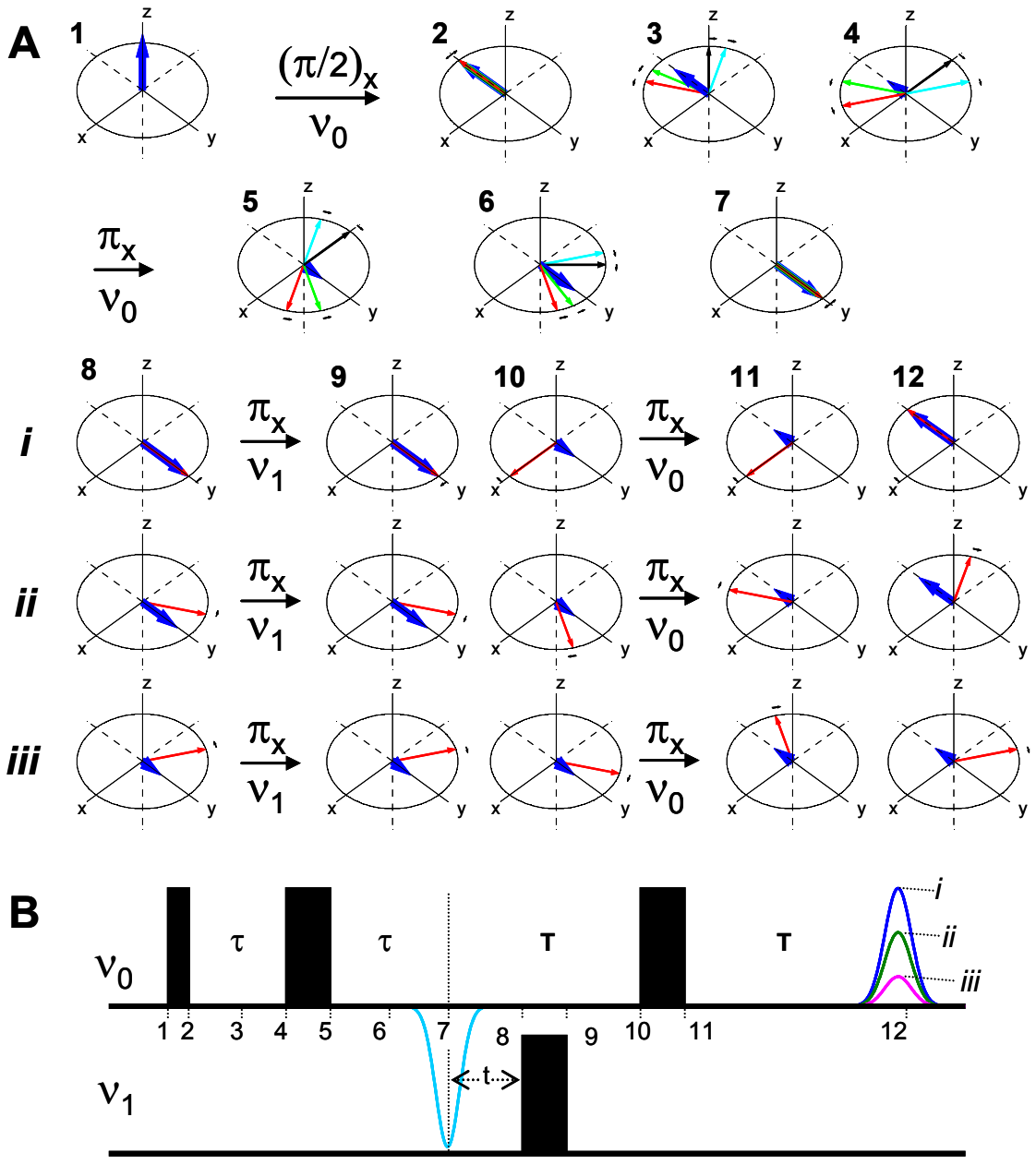

Figure 2-7: 4-pulse DEER pulse sequence (B,(Pannier et al., 2000)) and evolution of macroscopic magnetization in the rotating frame (A 1-12). Numbers 1-12 in A correspond to respective time positions in B. Net magnetization is shown in blue, and the magnetization of individual spins experiencing slightly different local magnetic fields are shown with red, green, black, and cyan lines. Small arrows represent the direction at which that particular spin packet is rotating. For simplicity, only the red spins and the net magnetization are shown in A 8-12, although other spins are still present in the system. The evolution of magnetization in A-i, -ii and -iii correspond to different values of t which denotes when the pulse at frequency ν_1 is applied, and the resulting net magnetization at 12 produces the echoes with different intensities shown in B . The DEER experiment is performed by keeping delay times τ and T constant and recording echo intensity at 12 by varying t (8) between 7 and 10.

By varying the time at which ν_1 is applied (t, Figure 2-7 Ai-iii), the echo intensity is modulated by a cosine function depending on the non-refocused spins' y-axis component, which in turn depends on the dipolar coupling ω_{AB} (Milov *et al.*, 1984):

$$I_{\text{intra}} = \cos(\omega_{AB} t) \qquad [5]$$

where, t is the time interval between the first echo and the applied pumping pulse (Figure 2-7 B) and ω_{AB} is the dipolar coupling which is defined as:

$$\omega_{AB} = \frac{\mu_B^2 g_A g_B}{2\pi\hbar r^3}(3\cos^2\theta - 1) \qquad [6]$$

where μ_B is the Bohr magneton, ħ is the reduced Planck's constant, g_A and g_B are the g values of the electrons excited by the observation and pump pulses respectively, θ is the angle that the inter-spin vector makes with the external magnetic field, and r is the distance between spins. In the case of observing distances between two spin labels, g_A and g_B could be approximated to be equal to the g value of a free electron, and hence $g_A.g_{B=} g^2$. The intensity of the overall signal can be described as:

$$I_{\text{DEER}} = I_{\text{inter}} I_{\text{intra}} \qquad [7]$$

where I_{intra} is the echo intensity due to localized spins within 1.7 nm - 8 nm range, and I_{inter} is the intermolecular background signal due to the interacting spins that have non specific distance. In a liquid sample where the spins are distributed homogenously in three dimensions, the background can be estimated by an exponential decay function $I_{\text{inter}} = Ae^{-kt}$ where parameter A characterizes the concentration of spins, and k depends on the g-values of A and B spins, and the number of excited B spins. The latter is an instrumental variable, depending on the pulse excitation bandwidth, and exact flip angles (Klauder *et al.*, 1962).

The depth of the modulation with respect to the total echo intensity (Δ) is a function of the fraction of coupled spins (f_Δ) within DEER sensitivity (1.7 nm < r < 8 nm)

$$\Delta = 1 - e^{\frac{f_\Delta}{C}} \qquad [8]$$

where C is the modulation depth constant which depends on the temperature, the type of the spin system, hyperfine anisotropy, and instrumental variables. C can be calculated for a nitroxide biradical where f_Δ is 1.

In non-rigid samples (e.g. spin label attached proteins), the distance *r* does not have a singular value, but is rather distributed around a certain mean. If we assume this distribution function to be *G(r)*, then the observed echo modulation is a result of overlapping signals of all distances defined by *G(r)*. Moreover, in a liquid sample, the inter-spin vectors are distributed homogenously in three dimensional space, and hence an integration over the angle θ in Eq. 6 is required. The final signal could then be described by a double integral over all values of θ and *r* in the sensitivity range:

$$I_{\text{intra}} = \int_{r_{\min}}^{r_{\max}} \int_{0}^{\frac{\pi}{2}} G(r) \sin\theta \cos\left[\frac{\mu_B^2 g_A^2}{2\pi\hbar r^3} (3\cos^2\theta - 1) t \right] d\theta dr \qquad [9]$$

Figure 2-8 illustrates the signal dependence on *G(r)* by showing simulated DEER echo modulation corresponding to Gaussian shaped distance distribution functions mean r and full width at half maximum w.

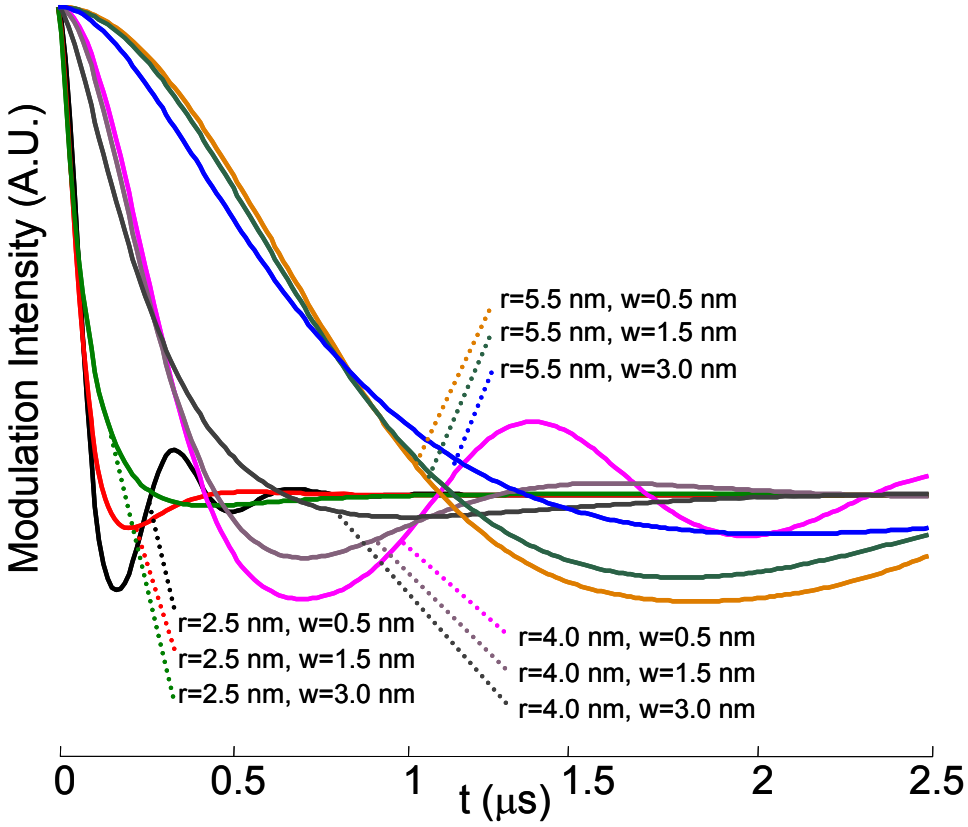

Figure 2-8: Simulated DEER signal at various distances (r) and distribution widths (w) showing only modulation of the echo without background. The signal was simulated using the DEFit program routines (section 2.2.4.)

2.2.3. Optimal Experimental Parameters of DEER

Due to the lower end limit of the microwave pulse lengths (12 ns on our instrument), only a fraction of the spin label spectra can be excited by the observe (ν_0 in Figure 2-7 B) and pump (ν_1) pulses. The weak signal requires extensive averaging, possibly over several hours. The spectrometer stability prevents signal to noise ratio improvement after ~12 hours of averaging, and even so, the experiment becomes costly. Optimization of experimental parameters is critical to acquire the highest signal to noise ratio in the shortest acquisition time.

Tests of signal to noise dependence on various factors were performed on a protein sample with reasonably strong signal: MTSSL labeled AntR15C dimer. The sample had final

concentration of 300 μM protein with 98% labeling, in 10 mM HEPES, 500 mM NaCl, 30% Ethylene Glycol, pH 7.0.

A low temperature is desired in DEER experiment for two reasons: 1) in order to extend the spin-spin relaxation time and thus bringing the resulting echo to an observable range (on the orders of ~100 ns), and 2) to decrease the number of spins in the ground state which are populated by the Boltzmann distribution, and thus increasing the number of spins excited by a single pulse. Conversely, the optimal repetition time of a single pulse pattern (SRT: shot repetition time) depends on T_1 since the system has to return to the equilibrium state before the pulse sequence is repeated. Previously (Fajer *et al.*, in press-b; Song, 2005), temperatures around 65 K were shown to yield best results for spin labeled proteins in sucrose. We used a different matrix (ethylene glycol), and hence repeated the temperature test. Using the same acquisition time, we measured standard deviation of the noise at temperatures 55 K, 65 K, and 85 K, adjusting SRT for each case so that the ~99% of the spins return to equilibrium after each measurement (Figure 2-9 A). Lowest noise was observed at 65 K, where SRT of 2 ms was used.

Two parameters are used for averaging the signal: shots (repeated pulse sequences) per point (h) and the number of time domain signal averages (n). Theoretically, the signal to noise should be independent of the variance between the two, as long as $n \times h$ is constant. However, instrument stability plays a role (probably due to phase cycling) and among the tested numbers where $n \times h = 500$, $n = 10$ resulted in the lowest noise (Figure 2-9 B).

The user has the option of recording the intensity of the echo peak or recording the integral of the echo. In the second case, a question arises as to how to define the integration interval. For an echo with full width at half maximum (w) of 62 ns, we scanned integration windows between 20 and 108 ns (Figure 2-9 C). We found that and an integration window equal to w (where ~75% of signal is present) produces lowest noise.

If the coupled spin concentration in the sample is above 1 mM the separation of DEER signal into pure modulation and homogenous background is not longer possible, since the inter molecular interactions become dominant in the DEER range (~2 nm to ~6 nm). This in turn invalidates the analysis method (Jeschke *et al.*, 2002). Most protein samples can hardly reach this

concentration without precipitation. Thus, the higher the concentration of the sample, the better for the DEER experiment. With regard to the choice of spin label, there has been cases (Song, 2005) where flexible spin labels which exhibit a high degree of spectral averaging resulted in large distance distributions, and vice versa. This study, on the contrary, showed (Chapter 4) that among MSL, MTSSL, and IASL, the mobility of the label at room temperature does not correlate with the distance distribution. This is probably due to the relatively slow freezing rate (in millisecond range) with respect to the dynamics (nanoseconds to microseconds), which may allow the spin label to take a single low energy conformation during freezing.

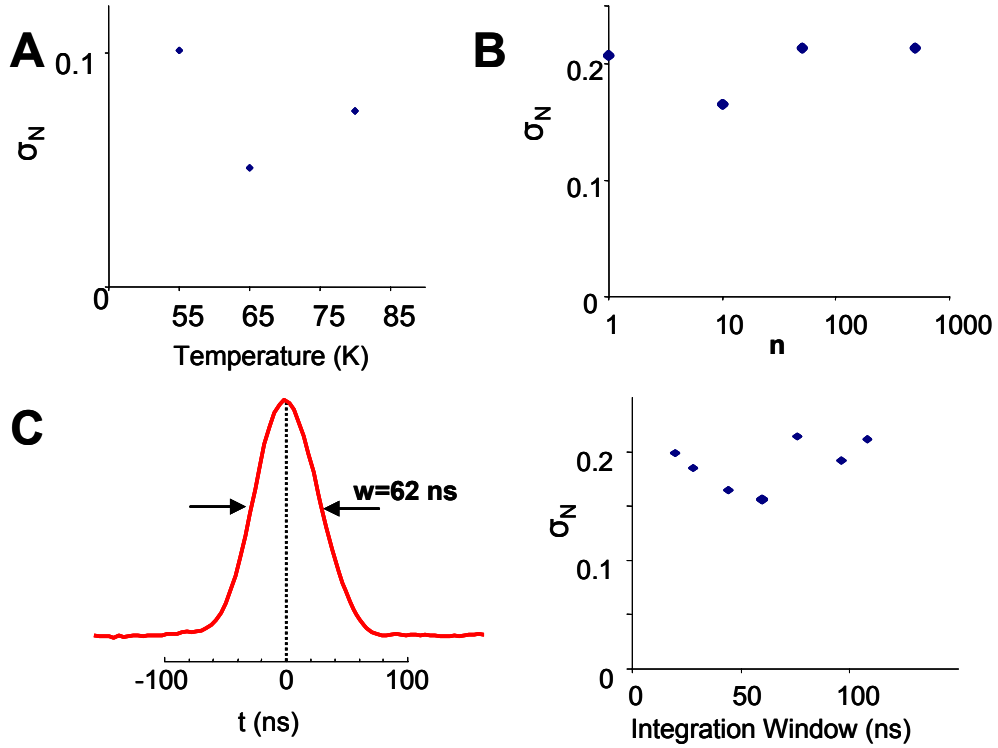

Figure 2-9: Standard deviation of the noise at the baseline (σ_N) depending on the temperature (A), number of time domain averages (n) when $n \times h$ is constant (B), and the width of integration window over the shown echo (C).

2.2.4. DEER Data Analysis

Several methods describing conversion of dipolar evolution to distances have been described (Jeschke et al., 2002). Despite their general applicability and model independent solution algorithms, these methods lack error analysis and fail to inform about the uniqueness of a solution. This is especially important when the real-life medium-to-high noise experimental data are being analyzed. When the data are noisy, algorithms try to compensate the noise by high frequency modulations. Only the modulations corresponding to distances shorter than 1.5 nm, can be artificially suppressed in analysis. Another problem arises when the distances are long (4.5 nm < r < 8 nm) and distributions are broad (w > 1 nm). Within the time domain data, the distance information of long and broad populations doesn't differ considerably from each other (this point is substantiated with results presented in Chapter 4), and the direct conversion of time domain data to distances does not inform about the uniqueness of the solutions.

We addressed this absence of error analysis in our dipolar evolution analysis program (DEFit). The software is model-dependent: distance distributions that contribute to dipolar signal were assumed to be Gaussian shaped, i.e. probability of finding a distance is approximated by a normal distribution.

For biological samples which often exhibit heterogeneity one can assume a normal distribution in the distance between two spin labels. Distribution shapes deviating from a Gaussian can be approximated by overlapping Gaussian curves. We developed a curve fitting program that tries several random initial parameter sets and optimizes the least squares using Simplex algorithm. This combined Monte Carlo/Simplex approach is being regularly used for fitting procedures in our lab (Fajer, 1994; Fajer *et al.*, 1990a; Fajer *et al.*, 1990b; Li *et al.*, 1994; Sale *et al.*, 2002; Sen *et al.*, 2006). DEFit uses the same fitting strategy and is coupled with a user friendly graphical interface and numerical integration.

In DEFit, initial parameters of the Gaussian functions (distance, width, and amplitude) were randomly chosen and varied while Simplex fitting the corresponding simulated dipolar

spectrum to the experimental data. The physical model used to generate distance distribution is one to four overlapped Gaussian populations, each of which is defined as:

$$G(r) = A_0 \frac{1}{\sigma\sqrt{2\pi}} e^{-\frac{(r-r_0)^2}{2\sigma^2}} \quad [10]$$

where the 3 parameters are: mean distance, r_0, standard deviation, σ, which is related to the full width at half maximum w by $w = 2\sigma\sqrt{\ln 2}$, and the amplitude, A_0. The Gaussian curves are normalized to $\frac{1}{A_0}\int_{-\infty}^{\infty} G(r)dr = 1$, so the amplitudes are actually the areas under the curve. The dipolar spectrum is then simulated using Eq. [9].

The least squares fitting is performed within boundaries of r_0:(1.7-8) nm, ω:(.1-4.5) nm, A_0:(0-0.02). This process is repeated for the specified number of Monte Carlo (MC) Steps, and the result of each iteration is shown to the user. Best result is plotted on the time and distance domains (red lines in Figure 2-11 and Figure 2-12).

DEFit then moves on to two Gaussians, $G(r) = G_1(r) + G_2(r)$, and repeats the MC fitting. Before it processes three Gaussians the program compares the results of one and two Gaussians by calculating the statistical *F* and *P* values. *F* is defined as the ratio of χ^2 of the two models:

$$F = \frac{\chi_2^2}{\chi_1^2} \quad [11]$$

where subscript 2 refers to the more complicated model (two Gaussians), and χ^2 is defined as

$$\chi^2 = \frac{1}{v}\sum\left(\frac{y_{data} - y_{fit}}{\sigma}\right)^2 \quad [12]$$

where ν, the degrees of freedom, is defined as the number of data points minus the number of parameters in the fitting function. *F* value itself can not be used to decide if "the decrease in χ^2 is worth the cost of additional parameters", however, it is used to calculate a probability (the *P* value) which answers the question: If the simpler model is really correct, what is the chance that you would randomly obtain data (for instance with a repetition experiment) that fits the more complicated model better? If the *P* value is low, DEFit concludes that the more complicated model is significantly better than the simpler model. If the *P* value is greater than the accepted threshold of 5% (Gonick *et al.*, 1993; Hoel *et al.*, 1971), DEFit decides that the previous model was "better". If *P* <5%, the program moves on to three Gaussians, and repeats every step thus far. The maximum number Gaussians tested is 4, which is rarely the desired model.

In order to describe the error surface DEFit generates a large family of solutions in the user-defined neighborhood, and calculates the χ^2 for each of the solutions. The surface of minimum χ^2 is then used to estimate the plausible solutions within the desired confidence limit (68% is used in this study).

This program was developed in Matlab 7.04 environment, and is available with source code at http://fajerpc.magnet.fsu.edu. The companion of DEFit is CWdipFit, which analyzes the dipolar broadening in a cw spectrum. CWdipFit uses identical fitting algorithm and is also available on the website.

2.2.5. Description of the Display

It is worthwhile to provide the description of the output of spectral analysis from DEFit on a real example, such as the DEER spectra found in Chapter 4. We chose two of the presented data, namely MTSSL labeled AntR protein on site 124, in its apo- and Zn(II) bound states (Figure 2-11 and Figure 2-12). Figure 2-11 A displays the background subtracted data (blue points) and the fit (red line); the resulting distance distributions are shown in Figure 2-11 B, and the goodness of fit surface is shown in Figure 2-11 C. This surface consists of the χ^2 values corresponding to the mean distance (r) and width (w) of the Gaussian curve it represents. In this

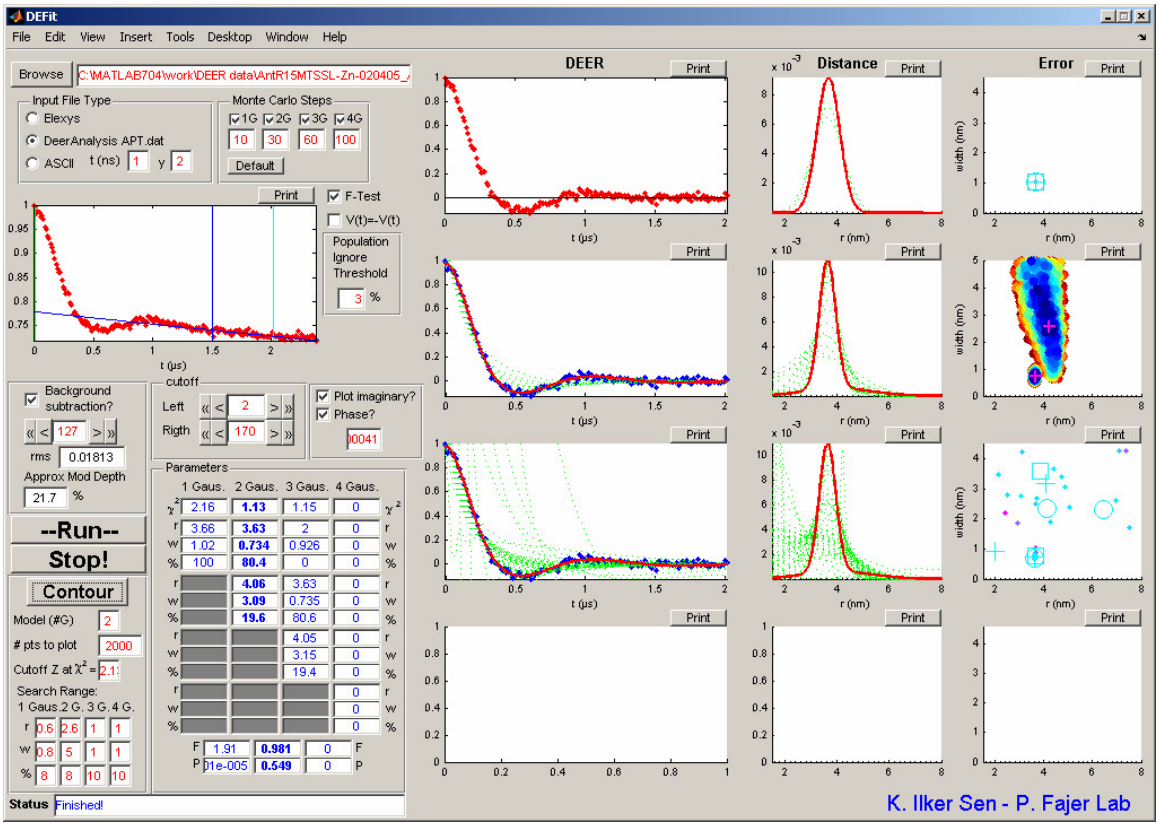

Figure 2-10: Screenshot of DEFit.

figure, χ^2 surface has one minimum because the distance distribution has only one Gaussian curve. The width of the minima in r and w axis's represent the uniqueness of this solution. χ^2 surface in Figure 2-12 C has two minima, since the solution has two Gaussian populations as shown in Figure 2-12 B. The population with the shorter mean distance (~3 nm) has a narrow χ^2 distribution, and hence it represents a well defined solution. On the other hand, the second Gaussian is not as well defined, especially in the width of the Gaussian population. Please note that although the width of the second Gaussian is not well defined the mean distance is. In fact all points in the χ^2 surface plots correspond to solutions within a certain statistical significance level (68%). Because the χ^2 calculation is normalized to degrees of freedom, the 68% confidence limit is defined between χ^2_{min} and $\chi^2_{min}+1$. Encoding of the relative fraction of each of the populations in the error plots is achieved by adjusting the transparency of the error surfaces As seen in the Figure 2-12 C the second population of AntR124MTSSL-Zn is at 1/3 transparency value of the first population to reflect 77% and 23% fractions of each populations.

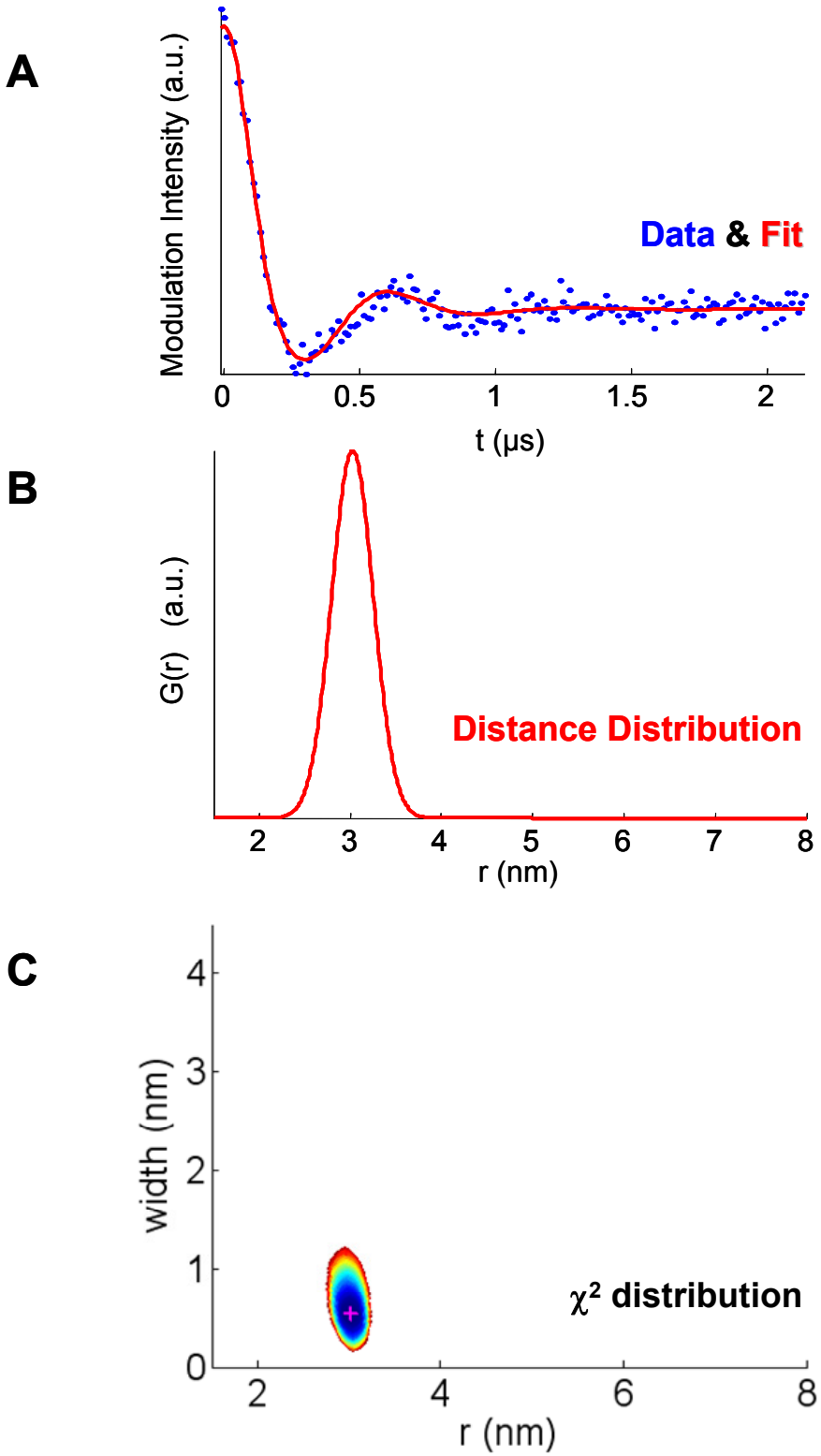

Figure 2-11: DEER time domain data (A-blue), the fit (A-red), the resulting distance distribution (B), and the χ^2 error surface of the fit (C) of AntR124MTSSL-apo. The magenta cross in C denotes the location of the best solution (lowest χ^2). Dark blue points correspond to lower χ^2 values and red to higher.

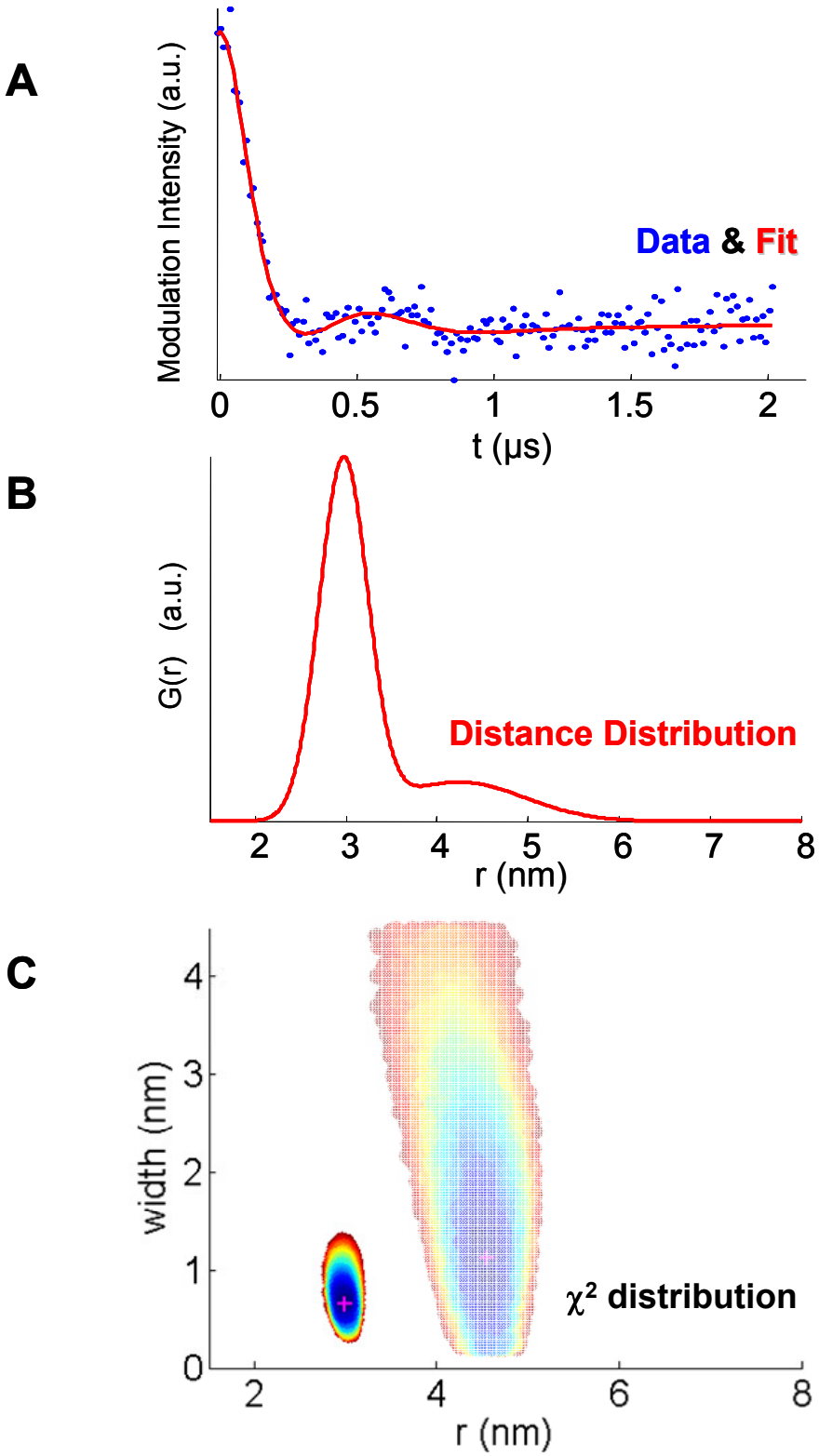

Figure 2-12: DEER time domain data (A-blue), the fit (A-red), the resulting distance distribution (B), and the χ^2 error surface of the fit (C) of Zn(II) bound AntR124MTSSL. The magenta crosses in C denote the location of the best solutions, and the transparency reflects the relative fractions of population, as discussed in the narrative.

CHAPTER 3

MN(II) BINDING BY ANTR

3.1. Study Aims

AntR binds to its cognate DNA sequence and represses gene activity only in presence of certain metal ions. Divalent Mn is presumed to be the physiologically relevant cation due to similarity searches of the encoding gene sequence, and shown to activate AntR best *in vitro*. Metal binding is one of the initial, and perhaps the most crucial step in AntR's activation. Here, we try to characterize the binding of divalent manganese to AntR, by measuring the binding stoichiometry, equilibrium binding constants, kinetic rates of binding, and examining the metal coordination environment. [Reproduced with permission from "Sen, K.I., Sienkiewicz, A., Love, J.F., vanderSpek, J.C., Fajer, P.G., and Logan, T.M. 2006. "Mn(II) binding by the anthracis repressor from Bacillus anthracis". Biochemistry 45(13):4295-4303." Copyright 2006 American Chemical Society.]

3.2. Materials and Methods

3.2.1. Preparation of Wild Type and Mutant AntR Constructs

AntR's DNA sequence was received from Dr. J. R. Murphy as an insert in pET11b vector. This plasmid contains ampicillin resistance factor and was previously used in DtxR studies (Marin et al., 2003; Rangachari et al., 2004; Twigg et al., 2001; Wylie et al., 2003; Wylie et al., 2005), yielding high expression levels. The plasmid was transformed into *E. coli* DH5α strain for amplification. Cells were grown over night on ampicillin (amp) containing Luria-Bertani (LB) plates at 37 ºC. One colony was transferred to 3 mL LB-amp media and was grown at 37 ºC until optical density of 0.6 at 600 nm (OD_{600}) was reached. Plasmid DNA from the

grown cells was extracted and purified using QIAGEN Plasmid Midi Kit (QIAGEN Inc., Valencia, CA). Intact AntR DNA sequence was confirmed by direct sequencing of the plasmid.

Primers for cysteine mutants of AntR were purchased from Integrated DNA technologies (IL). The nucleotide sequences are tabulated in APPENDIX A. The mutants were constructed using QuikChange kit (Stratagene, CA). Each mutant's DNA sequence was verified via sequencing after plasmid amplification.

3.2.2. Protein Expression

BL21-CodonPlus(DE3)-RIL (Stratagene, CA) strain of *E. coli* bacteria was used for large scale expression of recombinant AntR. AntR inserted pET11b plasmid was transformed into competent cells and grown on LB-amp plates at 37 ºC over night. Four to five colonies were transferred to 3 mL LB-amp media, grown in a shaker at 37 ºC until $O.D_{600}$ =0.6 is reached and transferred to 1 L terrific broth(TB)-amp media containing $MgSO_4$ (1 mM), "NPS" (25 mM $(NH_4)_2SO_4$, 50 mM KH_2PO_4, 50 mM Na_2HPO_4), and "5052" (0.5% glycerol, 0.05% glucose, 0.2% α-lactose). This media recipe was introduced in (Grabski et al., 2003) and promotes the self-induction for expression. In short, the cells grow until the glucose in the media is depleted. There on lactose update is facilitated. Once entered the cell, lactose displaces the lac repressor on the promoter and allows the continuous transcription of the protein. After 20-24 hours of growth in 37 ºC incubated shaker, cells were harvested via centrifugation at 10000x g for 20 minutes at 4 ºC. The pellets were resuspended in 50 mM Tris pH 8.5 (80 mL buffer per liter of media), and stored in -20 ºC freezer. Expression of AntR is confirmed via sodium dodecyl sulfate polyacrylamide gel electrophoresis (SDS PAGE).

3.2.3. Purification

Frozen cells were thawed at room temperature and lysed with high pressure micro-fluidizer (Microfluidics Co, MS). Cell lysate was filtered first via centrifugation at 40000x g, then with 0.2 μm syringe filters. AntR was purified via anion exchange chromatography using a HiPrep 16/10 Q FF column (25 mL bed volume; Amersham Biosciences, NJ) pre-equilibrated

with 50 mM Tris pH 8.5 (Buffer A) on fast protein liquid chromatography system (ÄKTA FPLC, Amersham Biosciences, NJ). Approximately 30 mL of clarified sample was loaded at 2 mL/min flow speed. Protein was eluted using a stepwise salt gradient. AntR eluted at 450-500 mM NaCl. A typical chromatogram is shown in Figure 3-1.

Purified AntR was identified on SDS PAGE by comparison to molecular weight standards (Figure 3-2) and demetallated by addition of 20 mM ethylenediaminetetraacetic acid (EDTA) and 3 M Urea. For cysteine mutants of AntR, 20 mM dithiothereitol (DTT) was also added, and the sample was incubated at 37 ºC water bath for 30 min to reduce disulfides to the reactive thiol form for spin labeling. All buffers used from this point on were degassed and demetallated via treating with Chelex resin (Bio-Rad Inc, CA). All glassware were demetallated by acid washing with 1 N nitric acid. AntR sample was exchanged into 10 mM Hepes, 500 mM NaCl pH 7.0 (protein buffer) by dialysis against 2 L of this buffer. The buffer was replaced with fresh four time every 4-6 hours.

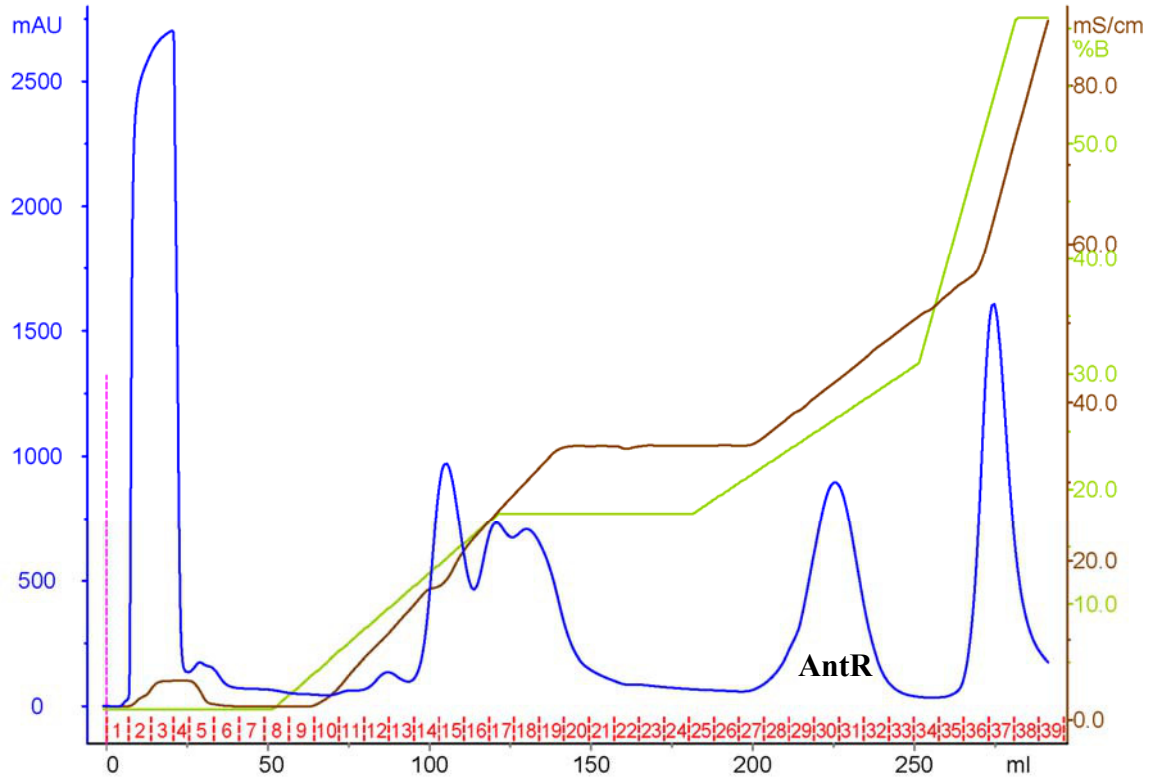

Figure 3-1: Anion exchange column chromatogram of AntR. UV absorbance at 280 nm wavelength is shown in blue, percentage of buffer B is in green, conductivity in brown, and the collected fractions are in red.

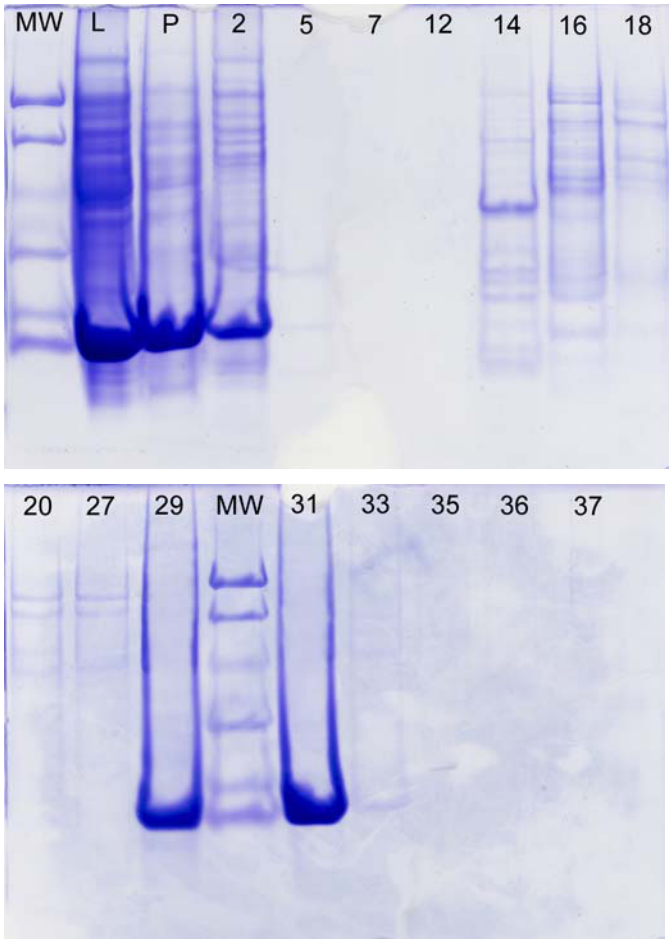

Figure 3-2: SDS-PAGE gel of anion exchange column. Molecular weight (MW) standard consists of globular proteins with molecular weights 97.4, 66.2, 45.0, 31.0, 21.5, and 14.4 kDa, top to bottom. The numbers (2-37) correspond to fractions shown with red in the chromatogram in Figure 3-1. L is the sample that was loaded to the column, and P is the lysis pellet. Based on this gel and chromatogram in Figure 3-1, fractions containing AntR (28-32) were collected.

Trace amounts of EDTA and DTT were removed with a desalting column (HiPrep 26/10 Desalting, Amersham Biosciences, NJ) on FPLC system using protein buffer and 1 mL/min flow speed Figure 3-3. The column was pre-washed with EDTA.

Purified and demetallated AntR's concentration was determined via UV absorption in 6 M guanidine hydrochloride at 276 nm wavelength using calculated extinction coefficient of 18450 $M^{-1}cm^{-1}$ (Gasteiger et al., 2003). Samples were finally concentrated to ~500 μM with a

stirred cell (Amicon Model 8200-200 mL and 8200-10 mL (Millipore Co., MA)) using EDTA pre-washed 10 kDa molecular weight cut-off membrane.

The expression and purification protocol typically yield 25-40 mg of purified recombinant AntR from 250 mL of culture. The metal content of apo AntR was measured with Inductively Coupled Plasma Mass Spectrometry (ICP-MS) by Dr. Vincent Salters at National High Magnetic Field Laboratory, FL. Total transition metal ion concentration of 500 μM protein in 10 mM Hepes, 500 mM NaCl, pH 7.0 was less than 0.1 μM, and that of buffer only was less than 0.03 μM. The largest contaminant was zinc with 0.09 μM in protein and 0.01 μM in buffer. Hence this protocol yields apo protein for all practical aspects.

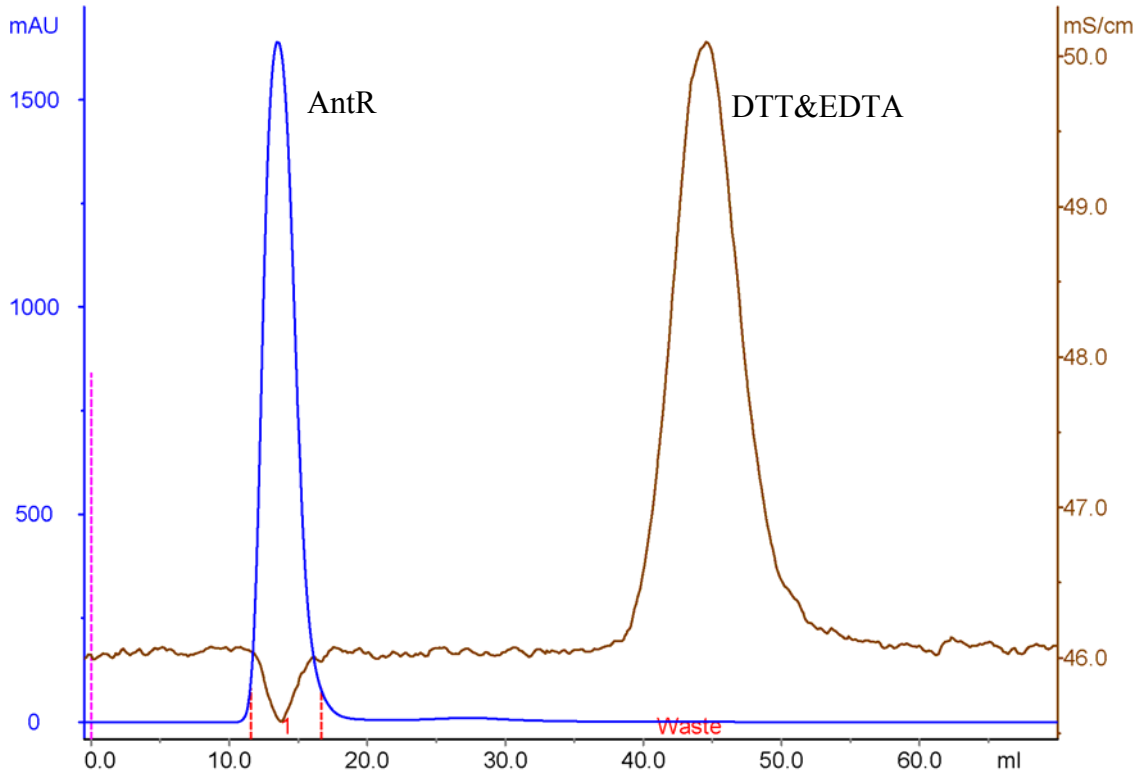

Figure 3-3: Desalting column chromatogram of purified AntR. UV absorbance at 280 nm is shown in blue and the conductivity is shown in brown (please note the scale). The positive peak in the conductivity graph is due to remnant EDTA and DTT.

3.2.4. EPR

The basic theory and the methods used for the EPR studies presented here were described in detail in section 2.1. .

3.3. Results

3.3.1. Stoichiometry of Mn(II) binding to AntR and the Binding constant

Mn(II) resonances observed in room temperature solution EPR spectra in the presence of varying concentrations of AntR arise only from unbound Mn(II) ions free in solution, and the amplitude of Mn(II) signal can be used to determine binding energetics.

The binding stoichiometry was calculated directly from the decrease of the free manganese signal intensity upon addition of a fixed amount of AntR and corresponded to two Mn(II) ions bound per AntR molecule. The binding curve exhibits a weak sigmoidal character (Figure 3-4). Quantitative estimates of binding parameters were obtained from curve fitting using the following binding models: **1**) two independent sites with identical dissociation constant; **2**) two independent sites with individual dissociation constants and stoichiometries; **3**) two sites exhibiting a finite positive cooperativity; and **4**) two sites with infinite cooperativity, e.g., both ligands binding simultaneously and no singly ligated species. Binding equations for these models, the resulting apparent dissociation constants, and the normalized sum of squared differences between data and fit (χ^2) are shown in Table 3-1. For Mn(II) binding, statistical analysis between infinite cooperativity (simpler model) and consecutive binding (more complex model) yielded an F-test result of F=2.9 and P-value of <5%. Thus, model **3** (consecutive binding with positive cooperativity) yields the best result, with apparent K_D's equal to 210 ± 18 μM and 16.6 ± 1.0 μM for the two binding sites. Transforming the binding data into a Scatchard representation (Figure 3-4 top-inset) indicated a concave-downward plot, confirming the positive cooperative nature for Mn(II) binding by AntR.

Table 3-1: Mn(II) and Zn(II) binding models, and fitting results.

Models		Mn(II) binding		Zn(II) binding	
Name	**Fraction bound**	**K_D(μM)**	**χ^2**	**K_D(μM)**	**[1]χ^2**
Identical	$r = \frac{2[Mn]_f}{K_D + [Mn]_f}$	49 ±10	0.74	123 ±139	0.78
Distinct	$r = \frac{n_1[Mn]_f}{K_{D1} + [Mn]_f} + \frac{n_2[Mn]_f}{K_{D2} + [Mn]_f}$	73 ±20 73 ±20 $n_1+n_2=2.3$	0.32	123 ±139 123 ±139 $(n_1+n_2=2.0)$	0.78
Consecutive	$r = \frac{K_{D2}[Mn]_f + 2[Mn]^2_f}{K_{D1}K_{D2} + K_{D2}[Mn]_f + [Mn]^2_f}$	210 ±18 16.6 ±1.0	0.03	5×10^7 $\pm1\times10^{12}$ 4×10^{-4} ±9	0.19
Inf. Coop.	$r = \frac{2[Mn]_f^{\,2}}{K_D^2 + [Mn]_f^{\,2}}$	53.9 ±18	0.08	152 ±47	0.16

[1] due to the absence of baseline in Zn(II) binding curve (Figure 3-4), χ^2 values for the fits are not normalized and are simply the sum of squared differences between data and fits.

3.3.1.1. Zn(II) binding

The apparent affinity of AntR for Zn(II) was determined by a competitive binding assay. Zn(II) is a structural analog of Mn(II) and activates AntR for DNA binding, but is diamagnetic and EPR silent. Zn(II) was titrated into Mn(II) saturated AntR, and the increase in Mn(II) signal intensity as a result of displaced ions was monitored using EPR. The resulting curve has a sigmoidal character and all bound Mn(II) was quantitatively displaced at 1:1 Mn(II) to Zn(II) molar ratio (Figure 3-4). The binding curve was modeled as described in Table 3-1, using $r^{Mn} = 2 - r^{Zn}$, where 2 denotes the total number of binding sites, and r^{Zn} is the number of bound Zn(II) per AntR. It is assumed that $[Zn(II)]_{free} \approx [Zn(II)]_{total}$. From the models considered in section 3.3.1. the infinitely cooperative binding model (**4**) was statistically the best with an apparent K_D of 152 ± 47 μM and χ^2 of 0.19.

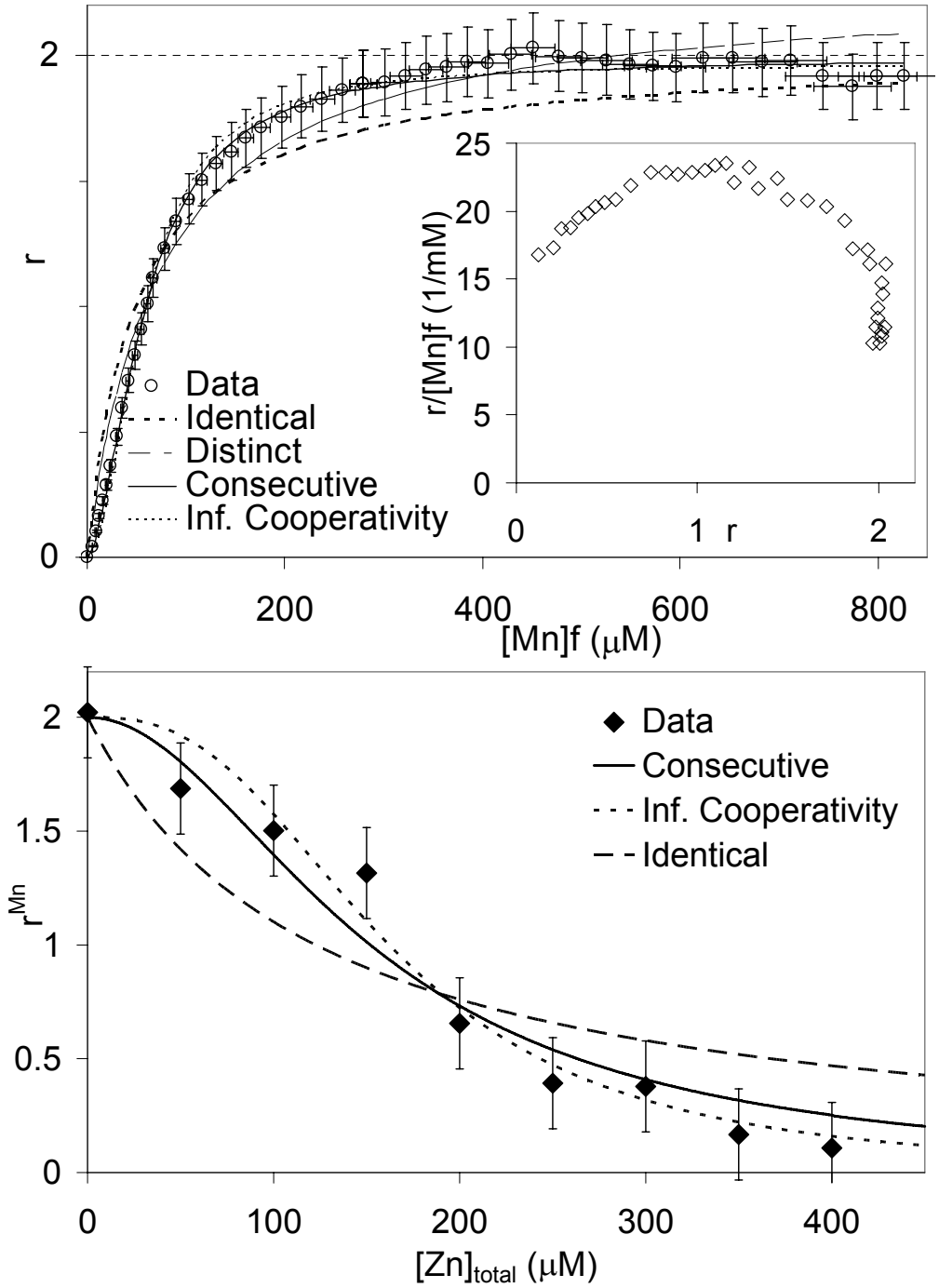

Figure 3-4: Equilibrium binding of manganese and zinc to AntR. Top: Fraction of Mn(II) bound to AntR (r) is calculated from the signal intensity of the lowest field transition and plotted against the free Mn(II) concentration. Individual data points represent the average of three independent observations with one standard deviation indicated by the error bars. The data were fit to specific binding models as described in the text. Top-Inset: Scatchard representation of the same data. Bottom: Fraction of bound Mn(II) with increasing Zn(II) concentration, and fits.

3.3.2. Binding Environment

The initial crystal structure of MntR showed a binuclear Mn(II) binding site. Since AntR does not have a crystal structure, we tested the hypothesis of having a di-Mn(II) site by EPR spectroscopy. Mn(II) has a complicated electronic system due to many anisotropic effects contributing to the Hamiltonian such as the Zeeman interaction, hyperfine interaction, zero field splitting (zfs), dipolar and possibly exchange interactions. Spectra are usually analyzed by exhaustive simulations involving many assumptions, at several temperatures, different EPR detection modes, and by comparison with the published model systems (Golombek *et al.*, 2003).

The cw spectra of Mn(II) bound AntR are dominated by six transitions centered at $g \approx 2$ with average hyperfine coupling of 9.1 mT (Figure 3-6). Additional signals within this six-line multiplet arise from forbidden transitions ($\Delta m_I=1$) at low temperatures. There was no significant change in the spectra recorded between 10 K and 70 K, nor was there evidence of a 4.5 mT coupling that would indicate the presence of a spin exchange interaction as in the case of dimanganese model compound (Figure 3-5). EPR spectra recorded in parallel resonator mode (where the magnetic component of the applied microwave is parallel to the external magnetic field, rather than perpendicular as in conventional EPR) of Mn(II)-loaded AntR exhibited residual perpendicular mode transitions at $g \approx 2$ and a broad featureless transition centered at $g \approx 4.9$. A similar transition was observed previously and attributed to S=1 spins in a dimanganese cluster *(Golombek et al., 2003)*. However, the S=1 transitions in parallel mode spectra are expected to increase in intensity between 0 and ~15 K, and decay slowly as the temperature is increased (D'Souza V et al., 2005), whereas the signal for Mn(II)-loaded AntR shows a relatively weak temperature dependence.

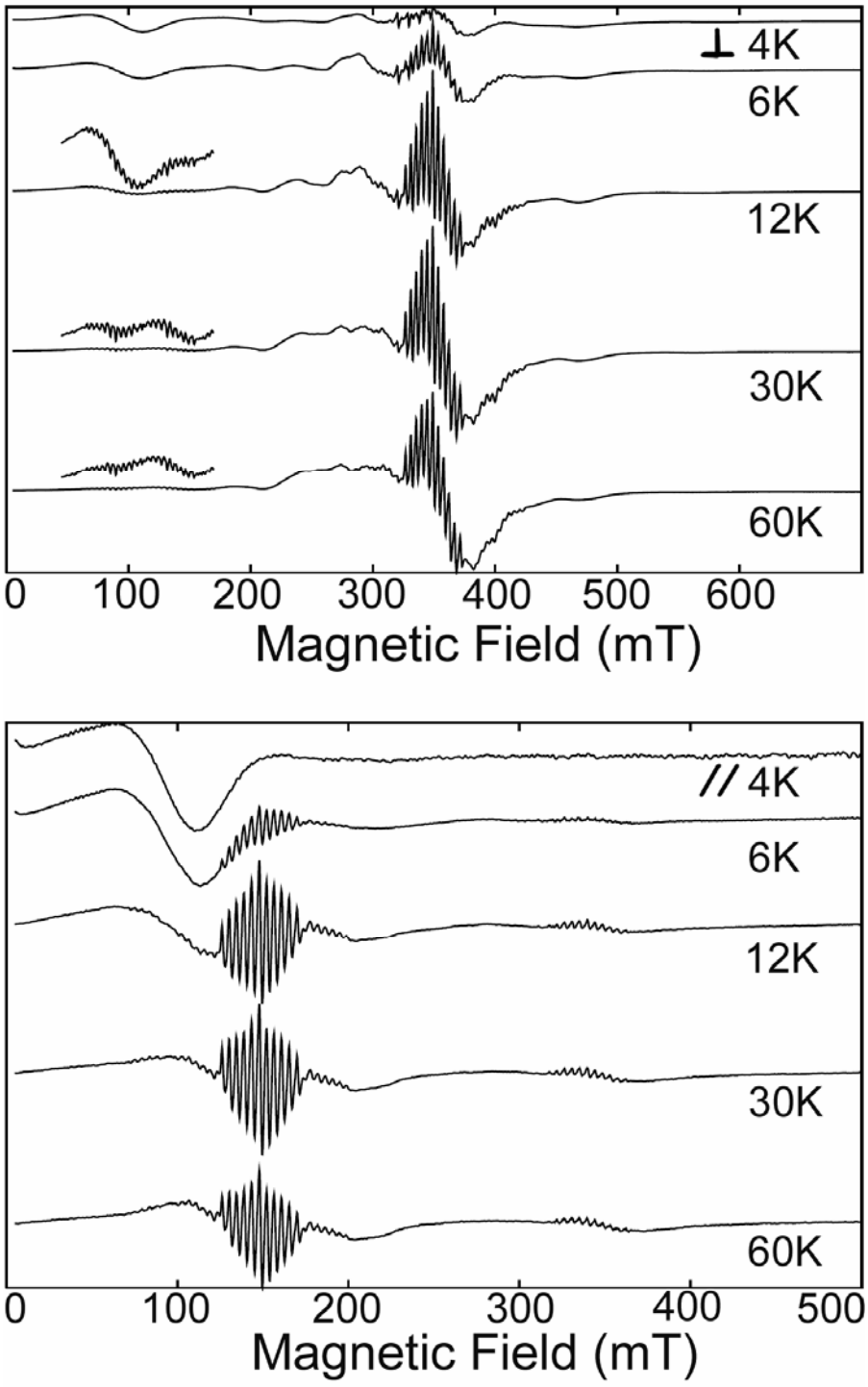

Figure 3-5: Cw EPR spectra of dimanganese model compound at indicated temperatures (4-60 K), at perpendicular (top) and parallel (bottom) resonator modes. Parameters for this experiment is given in section 2.1.2.

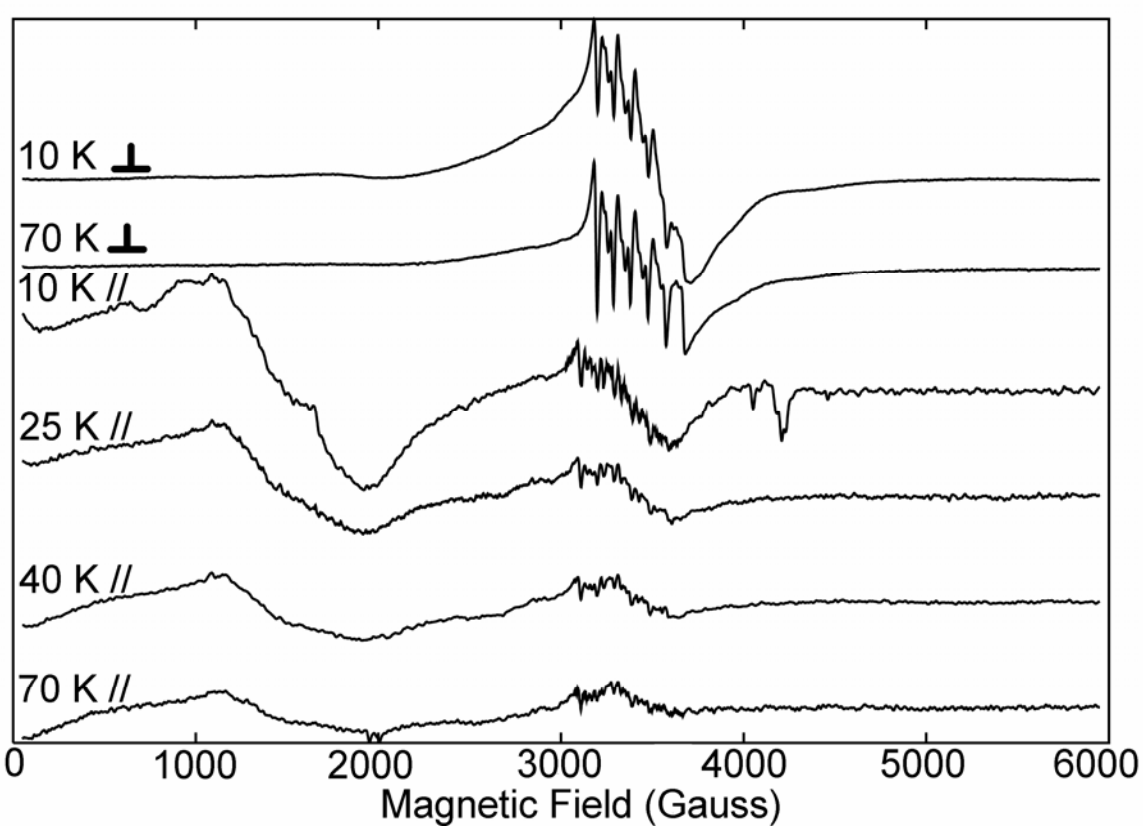

Figure 3-6: Cw EPR spectra of manganese bound AntR at indicated temperatures (10-70 K) and resonator modes (// perpendicular or ⊥ parallel). Parameters for this experiment is given in section 2.1.2.

3.3.3. Time Resolved Mn(II) binding and dissociation

The binding kinetics was investigated using a rapid mixing apparatus coupled to the EPR resonator. Experiments performed to measure the on-rate at saturating Mn(II) levels showed a time invariant signal, indicating that binding went to completion during the dead-time of the instrument, and yielding $k_{on} > 1000\ s^{-1}$ (not shown). The dissociation kinetics were measured by introducing Zn(II) and observing the time course for the increase in Mn(II) signal intensity. Upon mixing Mn(II)-saturated AntR with Zn(II) to a final molar ratio of 1:1 Mn:Zn, the intensity increased in a biphasic manner with each phase exhibiting approximately equal amplitudes (Figure 3-7). The transient was described by a double exponential decay function:

$$y = y_0 - A_1 e^{-k_1 t} - A_2 e^{-k_2 t} \qquad [14]$$

yielding apparent kinetic rate constants k_1 and k_2 of 35.7 ± 12.1 s^{-1} and 0.115 ± 0.009 s^{-1} respectively. A two-fold increase in Zn(II) concentration showed very similar rates (29.7 ± 15.6 s^{-1} and 0.117 ± 0.004 s^{-1}). Further increase resulted in protein precipitation. Conventional scanned cw EPR spectra were recorded immediately prior to and 30 minutes after mixing with Zn(II), indicating the endpoints of the kinetic experiment. The absolute signal intensity change in these spectra demonstrated that the two phases in the kinetic trace account quantitatively for the total signal change, signifying the absence of burst or slow kinetic phases for metal exchange.

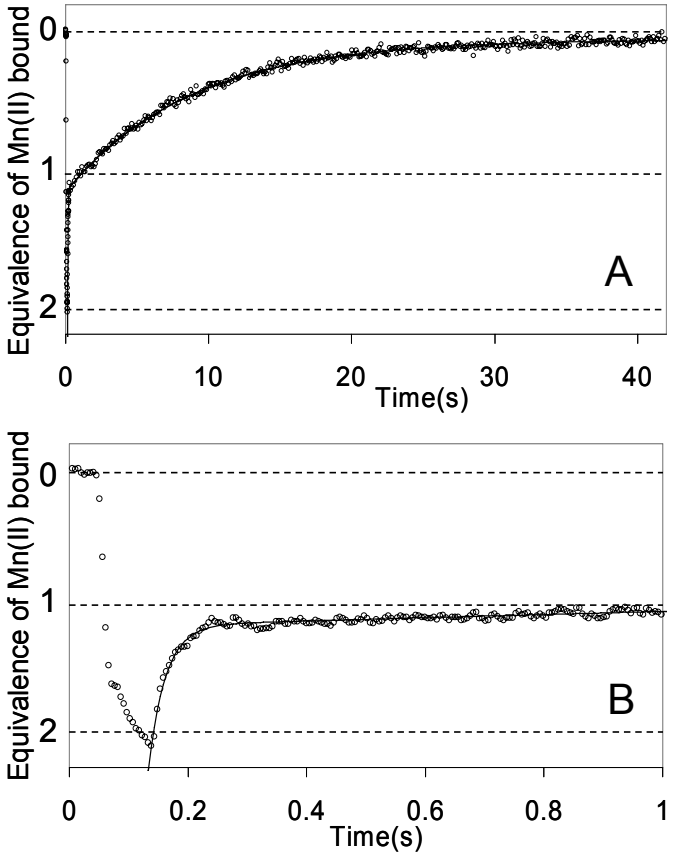

Figure 3-7: Kinetics of dissociation of Mn(II) from AntR at room temperature. (A) Time dependence of the Mn(II) EPR signal (data points) following mixing of Mn(II)-saturated AntR with an excess of Zn(II), and the fit (solid line). (B) Expansion of the early time points of the kinetic transient shown in panel A. The signal level at time zero is the equilibration point which will eventually (t ~ 60 s) be attained after mixing. During mixing (15 ms < t < 135 ms), the signal rapidly reaches that of a Mn(II)-bound AntR solution in one of the syringes, and when the flow is stopped (t =135 ms), the intensity increases in a biphasic manner due to Mn(II) being replaced in AntR.

3.4. Discussion

The DtxR family can be divided into proteins having one or two domains; DtxR and IdeR contain a C-terminal SH3 like domain and belong to the latter category whereas AntR and its homologue MntR lack this SH3-like domain and belong to the former. The two subfamilies exhibit homology in the amino acid residues participating in metal binding, DNA binding, and in dimerization. The SH3-like domain regulates the energetics of metal activation by affecting the dimerization state in the apo-repressor (Wylie et al., 2005) and by coordinating the metal in the ancillary metal binding site in the holo-repressor (Pohl et al., 1999). Further evidence for the regulatory nature of the SH3-like domain comes from the single site mutation in the SH3-like domain of DtxR and IdeR that results in a hyperactive repressor (Love et al., 2004; Manabe et al., 2005; Sun et al., 1998).

Despite the sequence homology, a recent crystal structure of metal-bound MntR revealed unexpected differences in metal coordination between the single and two domain proteins (Glasfeld et al., 2003). In DtxR and IdeR metals are coordinated in two structurally and functionally distinct sites, separated by ~9 Å. This coordination is relatively insensitive to the specific metal being bound (Qiu et al., 1996). On the other hand, MntR binds two equivalents of Mn(II) in a pH-dependent binuclear cluster containing two bridging carboxylate and one water ligand with inter-nuclear distance of 3.3 Å (Glasfeld et al., 2003), or a crystallization condition dependent non-binuclear site with ions separated by 4.4 Å (Kliegman et al., 2006). Given these differences, it is of particular interest to investigate metal binding and activation in single domain members of this family.

Mn(II) binding by AntR was characterized in this study using a combination of pulsed and cw EPR methods. AntR binds two equivalents of Mn(II) as shown by the equilibrium ligand binding studies, which saturate at 2 equivalents of Mn(II) (Figure 3-4 top). The concave-downward Scatchard plot (Figure 3-4 top inset) provides unambiguous evidence for positive cooperative binding of Mn(II) ions by AntR. A more quantitative estimate of the ligand binding energetics was obtained by fitting the data to a variety of binding models including independent and interacting sites. Curve fitting using models having noninteracting sites yields high χ^2 values

and nonrandom residuals. In contrast, fitting the data to models that include interacting sites improves the fit (Figure 3-4 and Table 3-1). Despite the fact that both cooperative binding models fit within the error range of the experiment, consecutive binding improves the fitting significantly, as confirmed by an F-test. The binding model based on sequential binding of the ligands with positive cooperativity also provides the more realistic model, yielding apparent equilibrium dissociation constants of 210 ± 18 μM and 16.6 ± 1.0 μM for the low and high affinity states, respectively.

Cooperative metal binding has not been directly characterized in DtxR family of proteins. Recent studies of IdeR clearly demonstrated positive cooperativity for metal-linked DNA binding *(Chou et al., 2004; Semavina et al., 2006)*. Since IdeR contains two tryptophans and metal-induced fluorescence changes arise not only from metal-quenching but also from metal-induced conformational changes, analysis of metal binding cooperativity was complicated. Target DNA binding by metal-activated DtxR and IdeR is cooperative (Chen et al., 2000; Chou et al., 2004), as the binding of the first dimer enhances the binding of the second. Cooperative metal binding in AntR may be an evolutionary step compromising for the lack of SH3-like domain, which has a regulatory role in DtxR (Wylie et al., 2005).

It is striking that DtxR and MntR coordinate metal in fundamentally different ways given the near conservation of the metal coordinating residues between the two proteins. Therefore, we were particularly interested to determine whether AntR coordinates the Mn(II) ions in a manner resembling DtxR or MntR. Here, we used variable temperature multi-mode cw EPR spectroscopy to investigate the hypothesis that spin exchange coupling exists in the manganese-bound state of AntR. The presence of spin-exchange coupling would provide clear evidence that the two Mn(II) ions are forming a binuclear cluster in AntR, as suggested from the MntR structure (

Figure 1-2). This approach has been used to identify the formation of a binuclear Mn(II) cluster in aminopeptidases (Brown *et al.*, 2002b; D'Souza *et al.*, 2000), concanavalin A (Antanaitis et al., 1987), phosphatase (Reiter et al., 2002), thiosulphate-oxidase (Cammack et al., 1989), arginase (Reczkowski *et al.*, 1992), phosphotriesterase (Chae et al., 1993), and enolase (Poyner

et al., 1992). As shown in Figure 3-6, our low temperature cw EPR spectra lack the spectral signatures associated with spin-exchange coupling, and therefore are not consistent with formation of a binuclear manganese cluster in AntR. Spin exchange coupling is strongly dependent on the metal-metal distance, the chemistry of the bridging atoms and their coordination geometry (Khangulov et al., 1995). The simplest explanation for the absence of a spin exchange coupling between the two bound Mn(II) ions in AntR is that the two metals are separated by more than ~4 Å. This does not exclude the possibility that the Mn(II) ions are bound within 4 Å of each other but are coordinated such that the spin exchange coupling is quenched. However, to our knowledge, there are no examples of such Mn(II)-containing proteins or compounds where the two Mn(II) ions are separated by < 4 Å and do not exhibit spin-exchange coupling.

The kinetics of metal binding or dissociation has not been previously reported for any DtxR homologue. The binding rate was faster than the resolution of our instrument ($k_{on} > 1000\ s^{-1}$). The dissociation rate was measured by displacement of bound Mn(II) with Zn(II). The EPR-silent Zn(II) is a good analog of Mn(II) as the Zn-bound AntR is capable of recognizing and binding to the cognate AntR promoter sequence (Love, 2003). Furthermore, equilibrium studies indicated that Zn(II) can quantitatively replace bound Mn(II) ions (Figure 3-4 bottom) and the displacement kinetics did not depend on Zn(II) concentration (over the two-fold concentration range). Hence the kinetics were determined by the Mn(II) dissociation from AntR and not by the binding of Zn(II) to the protein. Linking the kinetic rates to equilibrium binding constants at this stage is complicated by the cooperative nature of metal binding and by uncertainty regarding the molecular identity of the intermediate species formed during Mn(II) replacement by Zn(II). These intermediates may include, for instance, AntR species with one site occupied by Zn(II) and the other with Mn(II), species where one site is occupied by metal (either Mn(II) or Zn(II)) while the other site is unoccupied, both sites unoccupied, exchange of metal between sites, etc. We can, however, hypothesize that the binding of second Mn(II) with apparent dissociation constant $K_D = 16.6\ \mu M$ exhibits a rapid on ↔ off equilibrium where k_{off} is ~36 s^{-1}, and k_{on} is faster than 1000 s^{-1}.

Manganese is required for several metabolic enzymes and, as a cofactor for superoxide dismutase, is involved in the bacterial oxidative stress response (Cornish-Bowden, 1995). Bacteria must be able to accurately sense intracellular manganese concentrations and mount appropriate responses to fluctuations in the steady state concentration of Mn(II). *E. coli*, for instance, maintains 10-100 μM of manganese in the cell (Jakubovics *et al.*, 2001). The intracellular manganese concentration in *B. anthracis* is not known, however, *B. subtilis* requires at least 80 μM Mn(II) within the cell for sporulation (Finney *et al.*, 2003). Eisenstadt *et al*. have reported that in a controlled culture medium where the added Mn(II) is under 1 μM, *B. subtilis* accumulates 90% of the external Mn(II), and the manganese content of the cell is proportional to external Mn(II) concentration (Eisenstadt et al., 1973). The free Mn(II) concentration during bacterial growth and early sporulation could be as much as 300 μM. These values for intracellular free manganese are precisely in the range of AntR metal affinity. Our biophysical results indicate that AntR would respond rapidly and linearly to fluctuations in manganese concentration in this range by cycling between partially and fully ligated states. Thus, like MntR, AntR may provide the molecular signal transducer that regulates manganese homeostasis in *B. anthracis*.

CHAPTER 4

CONFORMATIONAL CHANGES OF ANTR UPON ACTIVATION

4.1. Study Aims

In the DtxR family of repressors, metal binding initiates the activation of the protein and leads to DNA binding and inhibition of gene transcription. The change of protein's state from apo to holo triggers a structural switch that elevates the binding affinity of the appropriate domain to the target operator. It would be particularly interesting to induce these kind of structural changes artificially, and possibly without the need for activating metal ions. Such an example is the hyperactive mutant (E175K) of the DtxR protein (Sun et al., 1998) which was shown to bind its DNA target in an iron depleted environment (Love et al., 2004). The knowledge of the 3D structure of a protein in its various states is often thought as a prerequisite for a rational design of therapeutic agents. Several X-ray structures of metal bound DtxR, IdeR, and MntR have been solved (Ding et al., 1996; Pohl et al., 1998; Pohl et al., 1999; Pohl et al., 1997; Qiu et al., 1996; Schiering et al., 1995; Sun et al., 1998; Twigg et al., 2001; Wylie et al., 2003), however, apo- structures are scarce (Pohl et al., 1998; Schiering et al., 1995; Smith et al., 2000). The crystal structures of DtxR in apo and metal bound states are identical giving little insight to the mechanism of metal regulated activation of the protein. There is a strong possibility that the crystallization either induced a similar structure or stabilized a similar structure from an array of different conformations. The NMR study of apo-DtxR (Twigg et al., 2001) differs from the x-ray structure (Pohl et al., 1998; Schiering et al., 1995). Extremely broad NMR resonances of the N-terminal domain of apo-DtxR imply unstructured, molten globule like conformation.

Another question bearing relevance on the mechanism of repressor activation is its oligomerization state. The two-domain members of the DtxR family (DtxR, IdeR) are dimeric in the active, metal bound form (Spiering et al., 2003; Tao et al., 1995), whereas the single domain members (MDR1, MntR) are already dimers in the apo- form (Bell et al., 1999; Lieser et al., 2003). AntR is homologous with MntR and apo state dimerization is highly probable.

Our aims were to address both questions: the oligomerization state of the repressor, and the conformational changes induced by metal binding. We thus characterized the metal induced changes in the local dynamics, measured distances between the monomers, and established the oligomerization state of the protein.

4.2. Materials and Methods

4.2.1. Size Exclusion Chromatography

Pre-packed Superdex 75 column (Amersham Biosciences, NJ) was calibrated with low molecular weight gel filtration calibration kit provided by the manufacturer (Figure 4-1) on ÄKTA FPLC (P-920, UPC-900, M-925, INV-907, Frac-900, Amersham Biosciences). The elution flow rate was 0.5 mL/min. The kit contained ribonuclease A (14.6 kDa), chymotrypsinogen A (20.3 kDa), ovalbumin (47.6 kDa), and bovine serum albumin (67 kDa). Blue Dextran 2000 (~2000 kDa) was used to determine the void volume (V_0 = 7.5 ml). Partition coefficient (K_{av}) was calculated with the formula:

$$K_{av} = \frac{V_e - V_0}{V_t - V_0} \qquad [15]$$

where V_e is the elution volume of each protein, V_t is the manufacturer specified total column volume (V_t = 24 ml). K_{av} has a linear dependence on the log of molecular weight of a globular protein, hence the constructed standard curve was used to calculate AntR's molecular weight. The estimated error in K_{av} determination of the standards was 10-25% according to the kit manufacturer. In oligomerization studies, AntR samples (10 μM) were prepared as described in Chapter 3, in 10 mM Hepes pH 7.0, and 0-500 mM NaCl. Samples (50 μl) were loaded on the

Superdex column which was pre-washed with 2 column volumes of 10 mM EDTA and equilibrated with 5 column volumes of the same buffer as the sample.

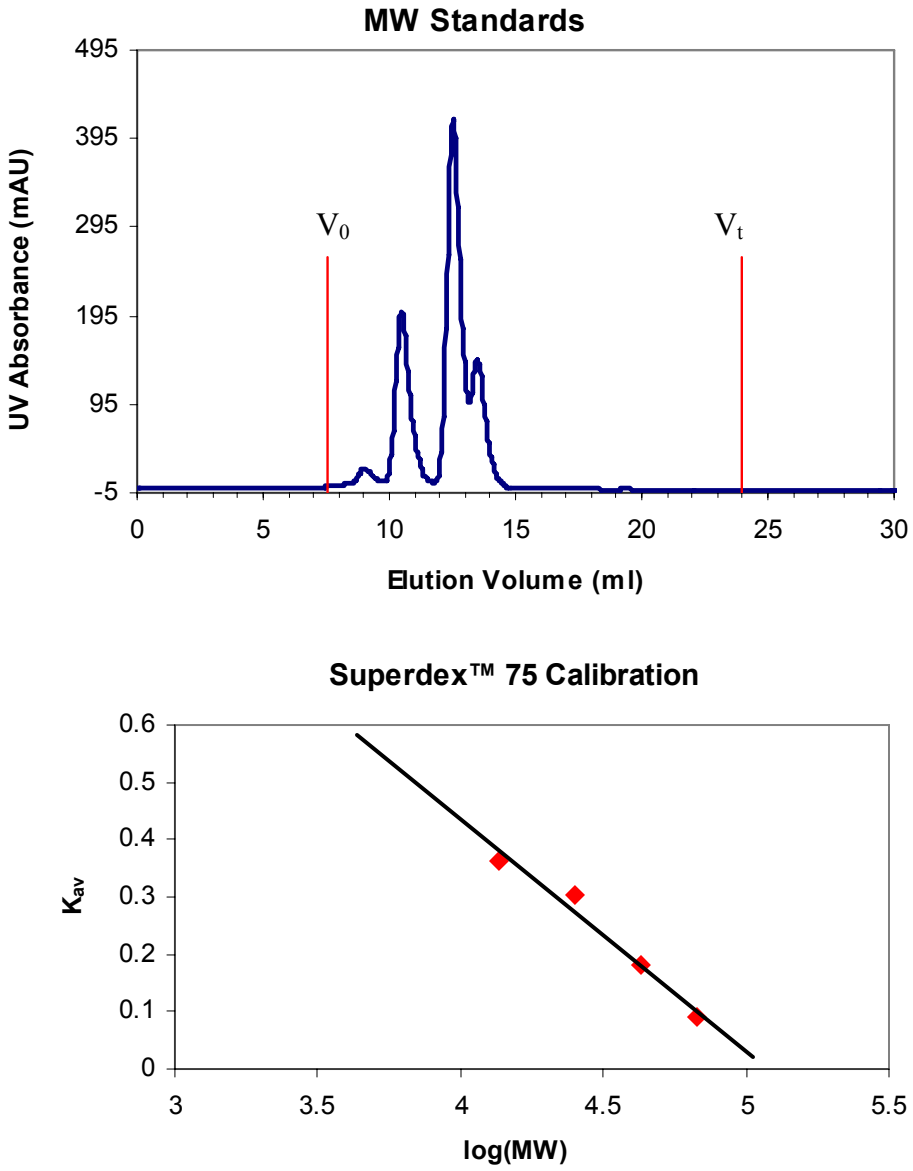

Figure 4-1: Chromatogram of Superdex 75 column calibration kit (top) and the standard curve (bottom). The partition coefficient (K_{av}) of four globular proteins of 14.6, 20.3, 47.6, and 67 kDa molecular weights were calculated using $K_{av}=(V_e-V_0)/(V_t-V_0)$, where V_0 was the void volume estimated from elution of Blue Dextran (~2000 kDa), V_t was the total volume of the column provided by the manufacturer, and V_e was the elution volume of the proteins.

4.2.2. Spin Labeling of AntR Mutants

Assuming that AntR's structure would be similar to its homologue MntR, we selected following sites for spin labeling: residue 15 close to the metal binding sites (Figure 4-2), residue 37 in the DNA binding domain, and residue 124 on a helix at the dimer interface. Single cysteine mutants of AntR (the wild-type does not contain a native cysteine) were prepared using QuikChange kit (Stratagene) in Molecular Cloning Facility at Florida State University's Department of Biological Sciences using primers shown in Appendix 0. Expression and purification were performed as described in Chapter 3. After the protein was clarified with anion exchange column, 20 mM DTT was added together with EDTA before dialysis and desalting. All buffers used in the subsequent steps were degassed. Protein yields were similar to wild type AntR (100-160 mg/L). Spin labeling with IASL, MSL, and MTSSL was carried out overnight at room temperature (T=293 K) at four-fold excess of spin label over 500 μM AntR monomer in protein buffer (10 mM HEPES, 500 mM NaCl, pH 7.0). Excess label was removed by dialysis against Chelex treated protein buffer. The efficiency of labeling was calculated from spin concentration determined from the second integral of EPR spectra using free spin label standards of known concentration, and from protein concentration determined by UV absorption at 276 nm using predicted extinction coefficient of 18450 M^{-1} cm^{-1}. All samples were labeled 90-98%. Binding to the cognate DNA of each spin labeled mutant was confirmed by DNA shift assay (Figure 4-3). BAmntHO DNA strand (200 nm)(Love, 2003) and AntR (20 μM) were loaded on 6% polyacrylamide gel in 40 mM Tris borate buffer pH 7.0. $MnCl_2$ was added to sample, gel, and running buffer (final concentration of 200 μM) immediately prior to electrophoresis. Gels were stained with SYBR-Gold fluorescent DNA staining agent and imaged using a Typhoon 9200 imager (Amersham Biosciences, NJ), or stained with ethidium bromide, illuminated with UV light (FBTI-88, Fisher Scientific, PA) and photographed with an electrophoresis system camera (FB-PDC-34, Fisher Scientific). AntR mutants labeled at site 37 showed partial binding to the DNA, probably due to its proximity to the DNA binding motif. The spin labeled sites 15 and 124 bound fully to DNA.

For metal activated AntR, the protein was incubated with $ZnSO_4$ at 4:1 Zn(II) to protein molar ratio. Immediately before the EPR experiments, 30% ethylene glycol was added for cryo-protection and to form frozen glass which prevents protein aggregation during freezing.

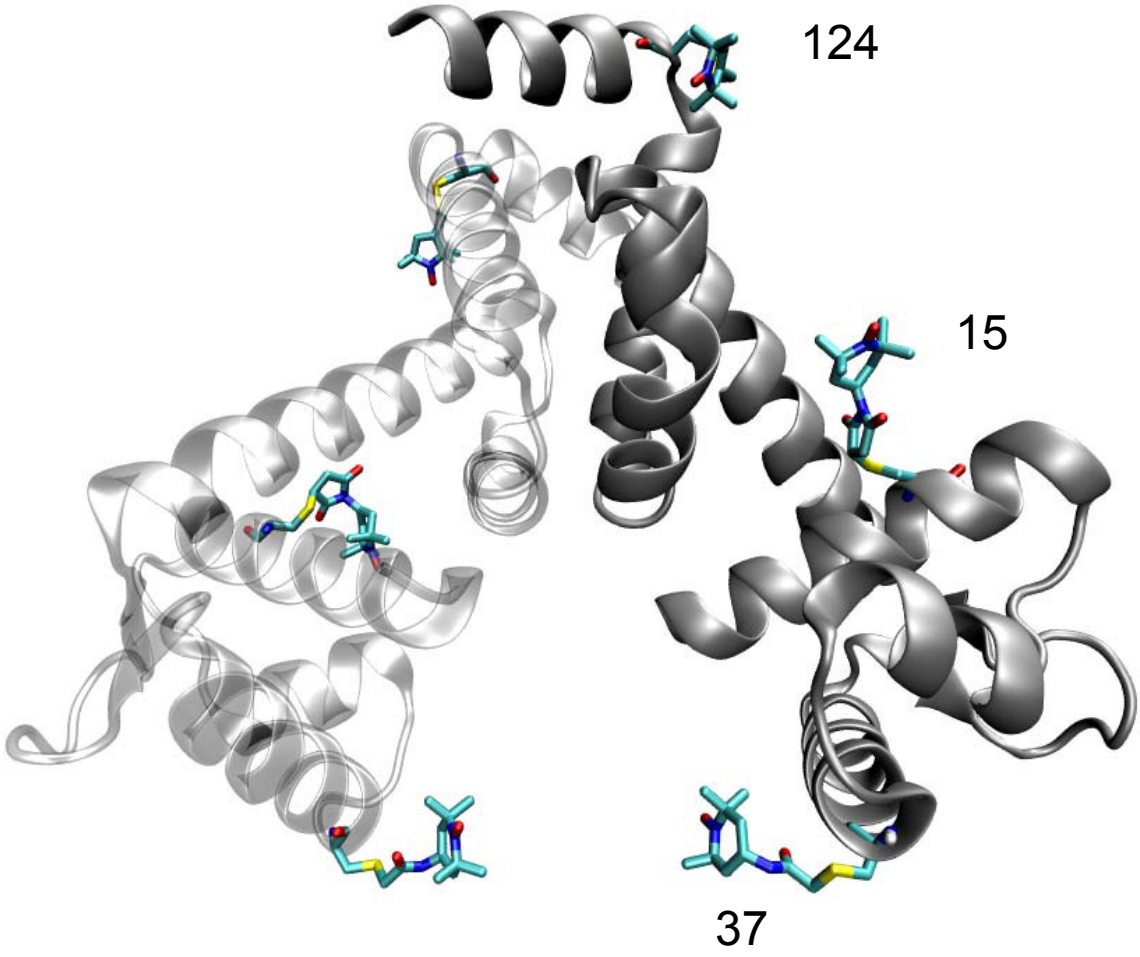

Figure 4-2: Mutation sites with attached spin labels on homology built AntR dimer structure. Sites 15, 37, and 124 were mutated to cysteine and reacted with spin labels IASL, MSL and MTSSL

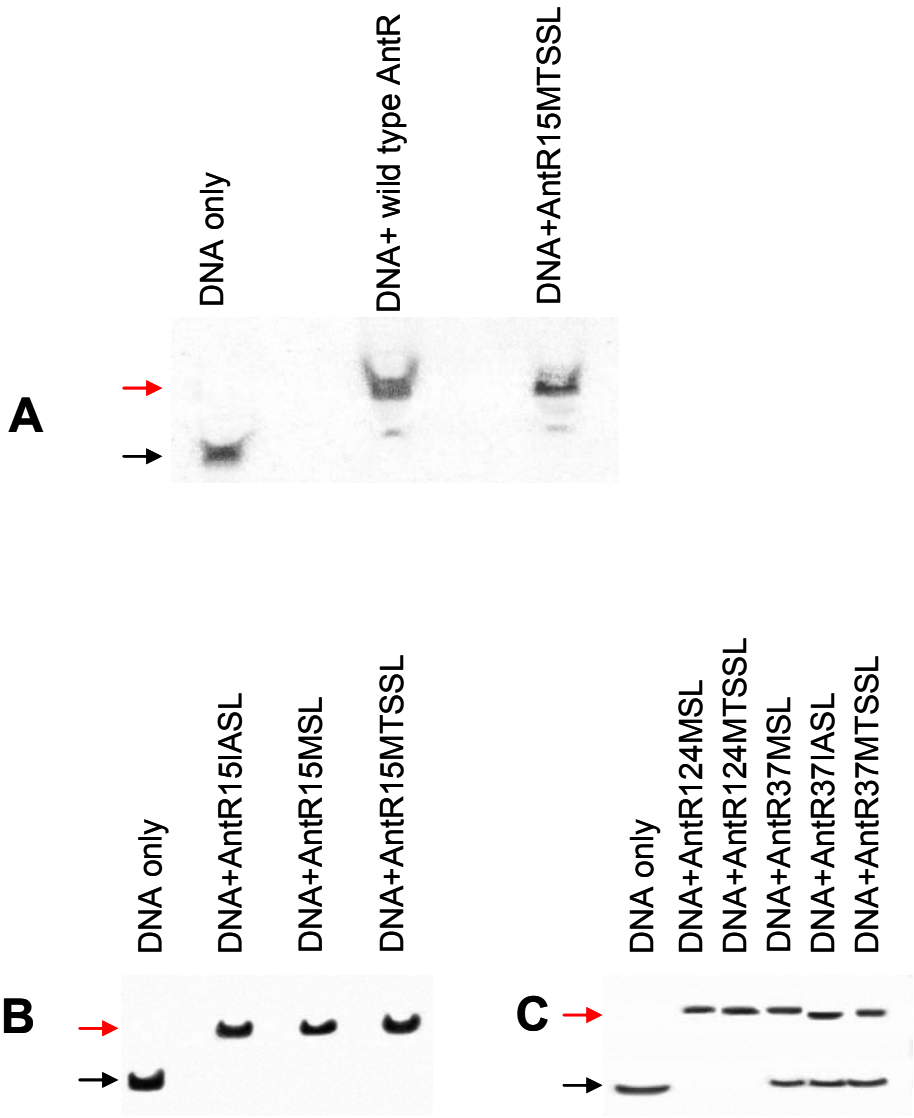

Figure 4-3: DNA shift assay gels, showing double stranded DNA target of AntR, bound (red arrow) and unbound (black arrow) by the wild type and spin labeled repressor A: Binding comparison of MTSSL labeled AntR on site 15 with wild type AntR, showing similar amount of shifting of the DNA target; B: Comparison of all spin labeled AntR15C mutants, all showing full binding; C: Shift assays of spin labeled AntR124C and AntR37C. AntR124MSL and AntR124MTSSL fully shift the DNA target, whereas all spin labeled AntR37C mutants show only partial activity.

4.2.3. EPR

Continuous wave and DEER experiments performed in this study are described in detail in Chapter 2. In all experiments, Zn(II) was chosen as the activating metal of AntR, because Mn(II) is paramagnetic, overlaps with nitroxide spectrum, and changes its relaxation properties. When two paramagnetic centers are close in space, the relaxation time of the slow relaxing species, here the spin label, is enhanced by the fast relaxing spin, such as Mn(II).

4.2.4. Modeling of Spin Label Conformers

All simulations were performed with CHARMM using CHARMM19 extended atom force fields with a distance dependent dielectric constant and topologies described as in (Fajer *et al.*, in press-a). A detailed description of the methods and the scripts used for modeling are available at http://fajerpc.magnet.fsu.edu. AntR's structure was homology built (Lambert et al., 2002) from the structure of Mn(II) bound MntR (Glasfeld et al., 2003) and energy minimized. Residues 15, 37, and 124 were computationally mutated to spin label side chains using the Biopolymer module of InsightII 2000 (Molecular Simulations Inc., CA). The modeling was divided into two stages. First, conformational space of the spin label was searched by a Metropolis Monte Carlo minimization algorithm. An initial structure for the docked spin label was chosen randomly and for each iteration a randomly chosen dihedral angle of the spin label side chain was rotated by a random amount. This conformer was then energy minimized while the entire protein structure is restrained ("rigid cage assumption"). The generated structure was accepted if it had lower potential energy then the previously accepted structure. If not, the Metropolis criterion (Metropolis et al., 1953) was applied at 300 K to determine whether to accept or reject the structure. For each spin label, 1500-2000 minimized structures were generated in order to exhaustively survey the rotamer space. 300 lowest energy conformers were selected for each AntR monomer and dimers were reconstructed by permuting these structures. The distances between spin labels across the AntR dimer were calculated using home written Matlab program. Probability of a given distance was calculated assuming a Boltzmann distribution in the total energies.

The second part is the molecular dynamics where the rigid cage assumption is relieved (Fajer *et al.*, in press-a). This ensures that the nearby side chains' can take different conformations due to the presence of the spin label, and provides a more accurate model of the spin label's local environment. We chose two of the lowest energy conformers in each monomer, constructed the dimers by permuting the structures, and used these as starting structures (seeds) in the simulations. All atoms within 15 Å distance of the spin label were allowed to move. Since the starting structure was stationary (total kinetic energy = 0), the initial step was to slowly heat the protein (12 ps simulation with 2 fs time steps) to T=300 K , and assign kinetic energies to every atom. The structure was then equilibrated for 200 ps with 1 fs time steps, and the production run was performed for 2-4 ns with 2 fs time steps. The distances from trajectories are pooled via home written scripts for VMD software package (Fajer *et al.*, in press-a; Humphrey *et al.*, 1996).

4.3. Results

4.3.1. Dimerization of AntR

To characterize the oligomeric state of AntR, the molecular weight of the protein was estimated using size exclusion chromatography. At and below 100 mM NaCl concentrations (Figure 4-4 A), the AntR elution profile was broad, being distributed between the void volume (V_0) of 7.5 ml and the final elution volume (V_e)of 12.8 ml indicating extensive non-specific protein aggregation. Increasing the NaCl concentration to 200 mM reduced the amount of a protein in the void volume to 2.5% and this remained constant at higher salt concentrations (Figure 4-4 B and Figure 4-5 A).

At 500 mM NaCl,10 μM apo-AntR eluted at a position expected for a globular protein of 34.5 ± 4.4 kDa, in agreement with the molecular weight of AntR dimer (33.2 kDa). The size of the putative dimer was independent of the salt concentration: 34.6 ± 4.0 kDa, 34.2 ± 3.6 kDa, and 32.3 ± 4.2 in buffers containing 400 mM, 300 mM, and 200 mM NaCl concentrations respectively; and importantly, did not depend strongly on the protein concentration. Increasing the latter 30-fold resulted in a major peak at 33.5 ±3.9 kDa with a minor peak at 65.1 ± 7.8 kDa

protein, suggesting an AntR tetramer (Figure 4-5 B). The overall contribution of this oligomeric state in the chromatogram is less than 3%, and hence was considered insignificant.

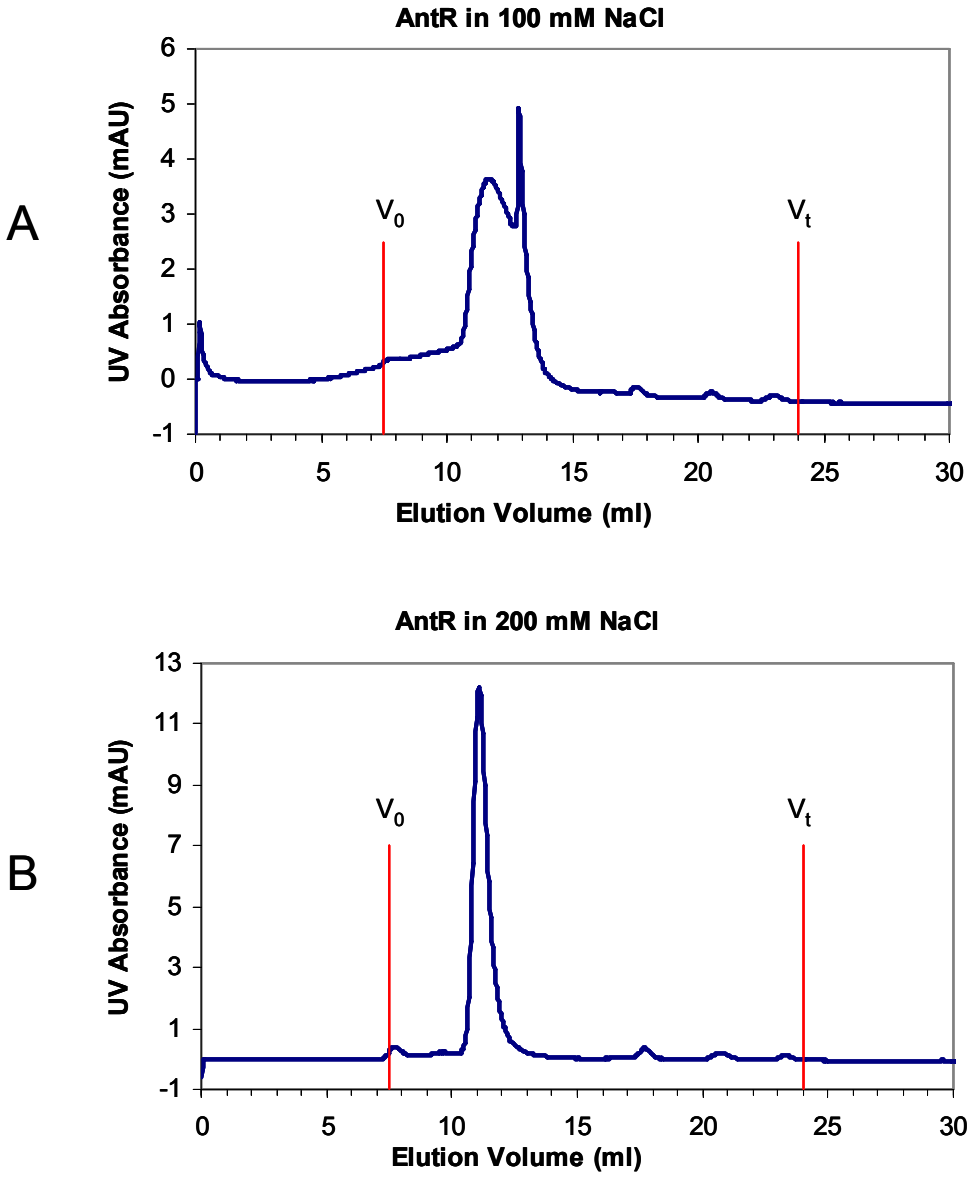

Figure 4-4: Size exclusion chromatogram of 10 μM apo-AntR in 10 mM Hepes pH 7.0 and 100 mM (A), and 200 mM (B) NaCl. The elution peaks in B corresponds to 32.3 ±4.2 kDa globular protein, in agreement with calculated AntR dimer molecular weight of 33.2 kDa.

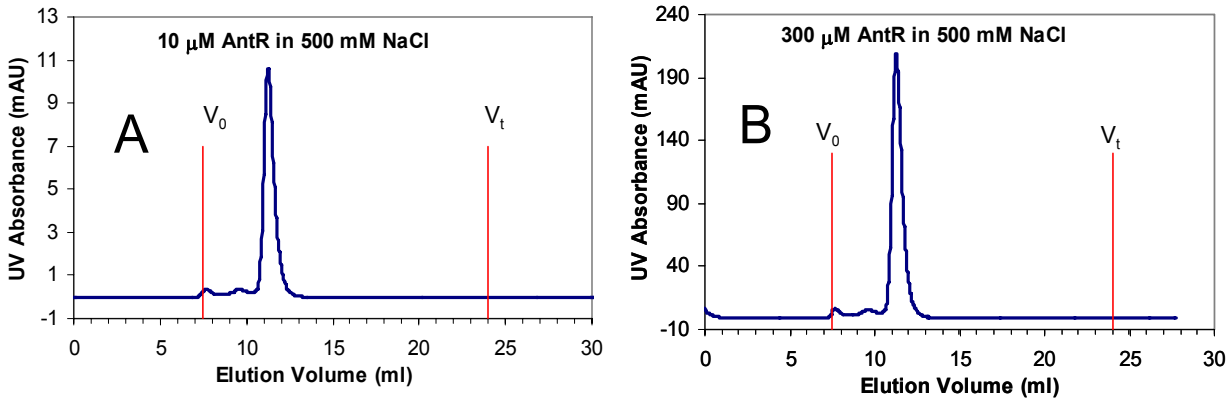

Figure 4-5: Size exclusion chromatogram of 10 μM (A) and 300 μM (B) apo-AntR in 10 mM Hepes pH 7.0 and 500 mM NaCl. The elution peaks in A and B correspond to 34.5 ±4.4 kDa and 33.5 ±3.9 kDa globular protein respectively, in agreement with calculated AntR dimer molecular weight of 33.2 kDa.

4.3.2. Dynamics of AntR

The nitroxide spin label attached to Cysteine side chains is expected to be sensitive to the local conformation and to changes in the environment. To detect these changes, we used EPR which is sensitive to the mobility of the spin labels. The EPR spectra of three different spin labels at three different sites in AntR are shown in Figure 4-6 to Figure 4-14. These vantage points were chosen to report on structural and dynamic properties of the DNA binding helix (37C), the dimer interface (124C), and the metal binding site (15C). The figures illustrates the spectra recorded in the absence of metal (Figure 4-6 A); with bound Zn(II) (Figure 4-6 B), and the metal and DNA (Figure 4-6 C) as well as the spectral simulations. Spectral line shapes were simulated with a Monte Carlo/SIMPLEX algorithm incorporating stochastic Liouville equation (Fajer *et al.*, 1990a). The best fit parameters are given in Table 4-1. The magnetic g and A tensors were determined from protein immobilized on DITC glass beads (Adhikari *et al.*, 1999; Baumann *et al.*, 2001; Li *et al.*, 1994; Szczesna *et al.*, 1995). Protein bound to the glass beads via lysine residues does not exhibit motion and EPR line shapes are described solely by the magnetic tensors and librational motion of the spin label (Figure 4-6). In some cases, the protein is immobilized but the spin label is free to wobble on the protein surface (librational motion). Such

spectra were simulated with two components having the same g and A tensors, but different rotational diffusion tensor, Lorentzian line widths denoting homogenous broadening and Gaussian inhomogeneous broadening (Table 4-1). We ascribe the origin of these two populations to either two local environments or to two different rotamers of the spin label: one immobilized on the protein surface and the other free to move. These populations persist when the protein is free in solution, and thus except for the apo IASL cases (Figure 4-11 and Figure 4-14), all the other EPR spectra can be decomposed in two components of varying rotational rate (denoted with R in Table 4-1). The diffusion rate tensor motion is anisotropic ($R_x \neq R_y \neq R_z$) showing no preferential motion about any principal axis of the magnetic tensor. The simulated line shapes for all spectra were least sensitive to changes in R_z, because the orthogonal (x and y) tensor components overlap with each other in the central feature. Thus we report the average rotational diffusion rate R_{av} as the geometric mean of R_x and R_y.

At site 124, MSL label in the apo state has a fast and a moderately slow component corresponding to R_{av}=8.3 and R_{av}=7.5 respectively. The slower population is in agreement with AntR dimer motion, which has a calculated rotational diffusion rate of R=7.6±0.4 (τ_R=25 ns). Therefore, the fast motion is the spin label libration. When Zn(II) is added to the sample, the fast component remains, however, the second motion rate decreases to R_{av}=6.8. The corresponding effect in the spectrum is broadening at the outer wings (Figure 4-7). DNA binding does not change the rotational motion further, however, the contribution of slower population to the spectra increases by ~20%, although no significant line shape changes are observed (qualitatively) in the spectrum. With a different spin label, MTSSL, at this site, similar dynamics are observed. Two populations at the apo state correspond to R_{av}=7.8 and R_{av}=7.4, slowing to R_{av}=7.5 and R_{av}=6.0 respectively with metal binding. DNA binding increases the slower population ratio by ~4%.

Spectral broadening with slowing protein dynamics upon Zn(II) binding is persistent at the other sites (15 and 37) and with all three spin labels (Table 4-1, Figure 4-9 to Figure 4-14), suggesting a globular backbone ordering. DNA binding induced no further changes in protein dynamics, but a small (<20%) increase in population differences in some cases.

Table 4-1: Simulation parameters for spin labeled AntR mutant spectra

Site&label	State	R^1_x	R_y	R_z	Ratio %	g_x	g_y	g_z	A_x	A_y	A_z	w_x	w_y	w_z	gib_0
124	Apo	8.3	8.3	10.5	28.0	a	b	c	7.0	7.0	37.5	0.6	0.1	0.5	1.3
MSL		7.3	7.8	6.8	72.0	``	``	``	``	``	37.5	0.1	1.8	0.1	2.6
	Zn	8.3	8.3	6.0	23.8	``	``	``	``	``	36.9	``	1.4	``	1.3
		7.7	6.0	7.6	76.2	``	``	``	``	``	35.5	``	0.1	``	2.5
	DNA	8.4	8.3	7.7	2.9	``	``	``	``	``	36.9	``	1.4	``	1.3
		7.7	6.0	7.5	97.1	``	``	``	``	``	35.5	``	0.1	``	2.5
124	Apo	7.5	8.1	10.0	49.6	d	e	f	6.0	6.0	35.0	0.5	0.5	0.5	1.3
MTSSL		6.7	8.1	6.0	50.4	``	``	``	7.0	``	``	``	``	``	``
	Zn	6.0	6.0	6.0	13.0	``	``	``	``	``	``	1.0	1.0	1.0	2.5
		7.2	7.9	6.0	87.0	``	``	``	``	``	``	0.6	0.6	0.6	1.3
	DNA	6.0	6.0	6.0	8.6	``	``	``	``	``	``	1.0	1.0	1.0	2.5
		7.3	7.9	7.3	91.4	``	``	``	``	``	``	0.6	0.6	0.6	1.3
15	Apo	7.1	8.4	8.0	40.8	a	b	c	7.0	7.0	36.0		0.3	``	``
MSL		7.2	7.4	10.0	59.2	``	``	``	``	``	35.5		0.6	``	``
	Zn	8.2	7.4	9.6	21.0	``	``	``	``	``	36.0		``	``	``
		7.3	7.2	9.2	79.0	``	``	``	``	``	35.5		``	``	``
	DNA	9.5	7.4	8.0	4.0	``	``	``	``	``	36.0	1.0	1.0	1.0	``
		1.6	6.0	7.8	96.0	``	``	``	``	``	35.5	0.6	0.6	0.6	``
15	Apo	8.1	7.6	8.2	66.2	d	e	f	6.0	6.0	35.0	0.2	0.2	0.2	1.0
MTSSL		6.0	8.1	5.8	33.8	``	``	``	7.0	``	``	``	``	``	1.1
	Zn	7.9	7.5	8.5	87.7	``	``	``	6.0	``	``	0.6	0.6	0.6	1.3
		6.0	7.8	6.1	12.3	``	``	``	7.0	``	``	``	``	``	``
	DNA	6.0	7.9	7.0	66.7	``	``	``	6.0	``	``	``	``	``	``
		8.0	8.0	9.4	33.3	``	``	``	6.0	``	``	``	``	``	``
15	Apo	7.4	8.3	10.0	100	a	g	h	7.5	7.7	35.7	0.2	0.1	0.4	``
IASL	Zn	6.3	8.0	7.8	56.8	``	``	``	``	``	``	0.9	0.4	0.2	1.0
		7.4	8.3	10.0	43.2	``	``	``	``	``	``	2.0	0.1	0.4	1.3
	DNA	6.3	8.0	6.0	19.0	``	``	``	``	``	``	1.8	1.5	0.9	``
		7.9	7.8	8.8	81.0	``	``	``	``	``	``	2.0	0.1	0.4	``
37	Apo	7.8	8.4	10.0	34.0	a	b	c	6.5	8.5	35.5	0.6	0.6	0.6	``
MSL		6.4	7.7	``	66.0	``	``	``	``	7.5	35.3	``	``	``	2.5
	Zn	7.1	8.3	``	32.1	``	``	``	``	``	36.0	``	``	``	1.3
		6.2	7.4	``	67.9	``	``	``	``	``	35.3	``	0.5	0.5	3.0
	DNA	7.2	8.3	``	34.2	``	``	``	``	``	36.0	``	0.6	0.6	1.3
		7.4	6.2	``	65.8	``	``	``	``	``	35.3	``	0.5	0.5	3.0
37	Apo	6.7	6.6	9.8	28.7	d	e	f	7.0	6.0	35.0	``	0.6	0.6	1.3
MTSSL		8.0	7.7	12.0	71.3	``	``	``	``	``	``	``	``	``	``
	Zn	6.0	6.3	7.1	52.1	``	``	``	``	``	``	1.6	1.6	1.6	2.2
		7.3	8.0	7.4	47.9	``	``	``	6.0	``	``	0.6	0.6	0.6	1.3
	DNA	6.0	6.8	6.3	45.7	``	``	``	7.0	``	``	1.6	1.6	1.6	2.5
		6.9	8.3	7.8	54.3	``	``	``	6.0	5.0	``	0.6	0.6	0.6	1.3
37	Apo	8.3	7.5	10.6	45.3	a	g	h	7.5	7.7	35.7	``	0.1	0.1	``
IASL	Zn	8.2	7.5	10.6	54.7	``	``	``	``	``	``	``	``	``	``
		7.2	7.8	7.0	45.7	``	``	``	``	``	``	2.9	0.7	1.6	2.9
	DNA	8.2	7.5	10.6	54.3	``	``	``	``	``	``	0.6	0.1	0.1	1.3
		7.2	7.8	7.0	45.3	``	``	``	``	``	``	2.9	0.7	1.6	1.1
DITC															
37	Apo	6.0	6.0	6.0	66.8	a	b	c	6.5	7.5	35.3	1.7	2.8	2.0	2.5
MSL		7.8	7.3	9.7	33.2	``	``	``	``	``	``	0.6	0.6	0.6	1.3
37	Apo	6.0	6.0	6.0	70.1	d	e	f	7.0	6.0	35.0	0.9	2.4	1.1	2.5
MTSSL		7.5	7.7	6.0	29.9	``	``	``	``	``	``	0.6	0.5	0.1	1.0
37	Zn	6.0	6.0	6.0	75.0	a	g	h	7.5	7.7	35.7	1.6	1.6	2.5	2.1
IASL		7.5	7.8	7.8	25.0	``	``	``	``	``	``	0.1	1.0	0.8	0.3

w and gib_0 are the Lorentzian and Gaussian line widths, R is related to correlation time by: $R=-\log(\tau_R)$, and Ratio % is the contribution to the overall intensity. For simplification, following symbols were used instead of g-values: a=2.009, b=2.007, c=2.0029, d=2.0078, e=2.0065, f=2.0025, g=2.0056, h=2.0021. Values same as the previous row were denoted with ``.

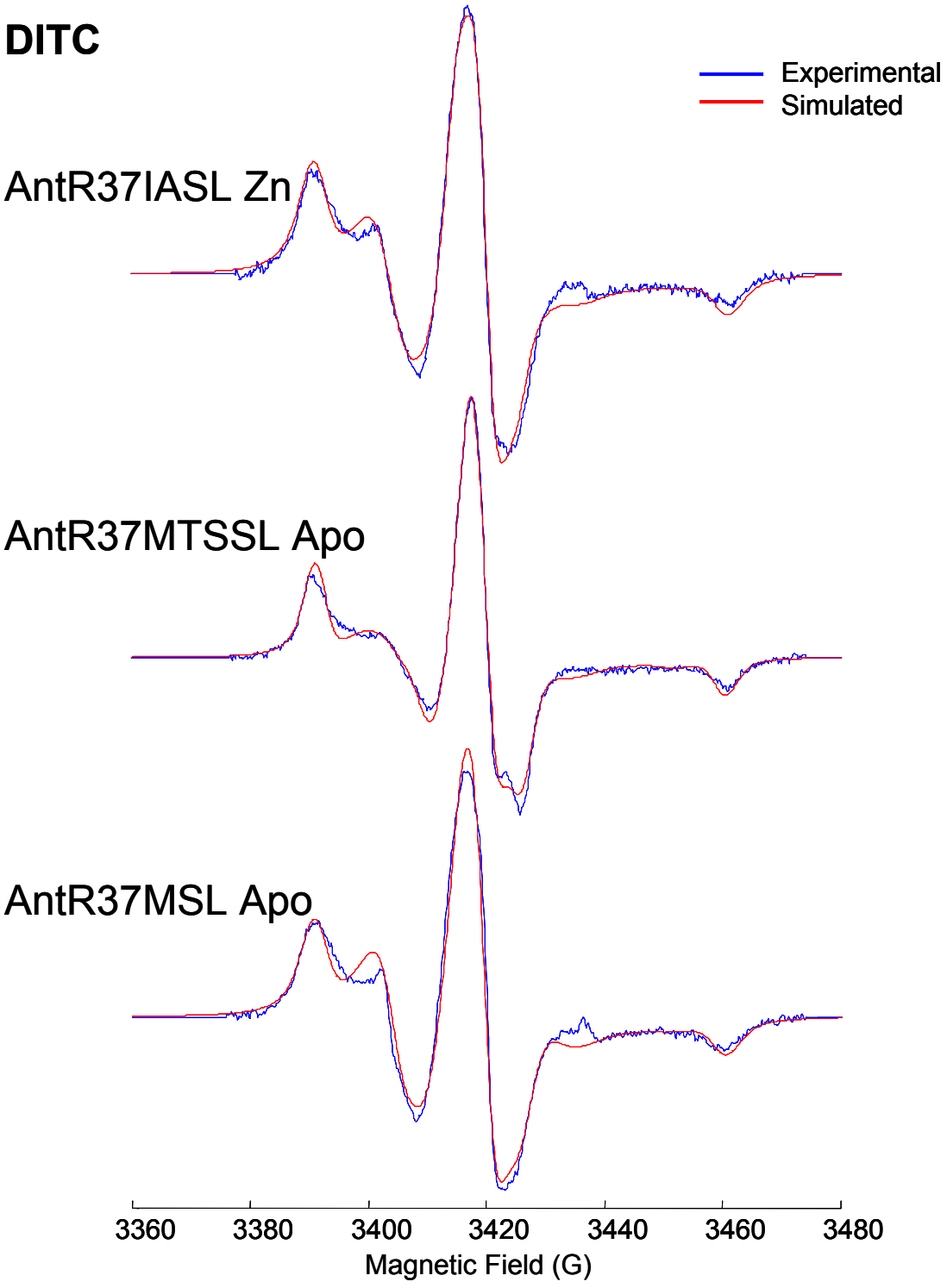

Figure 4-6: EPR spectra of DITC glass beads bound MSL, MTSSL, and IASL labeled AntR37C (red) and their simulations (blue). The g and A tensors extracted from these simulations were used in fitting all other spectra

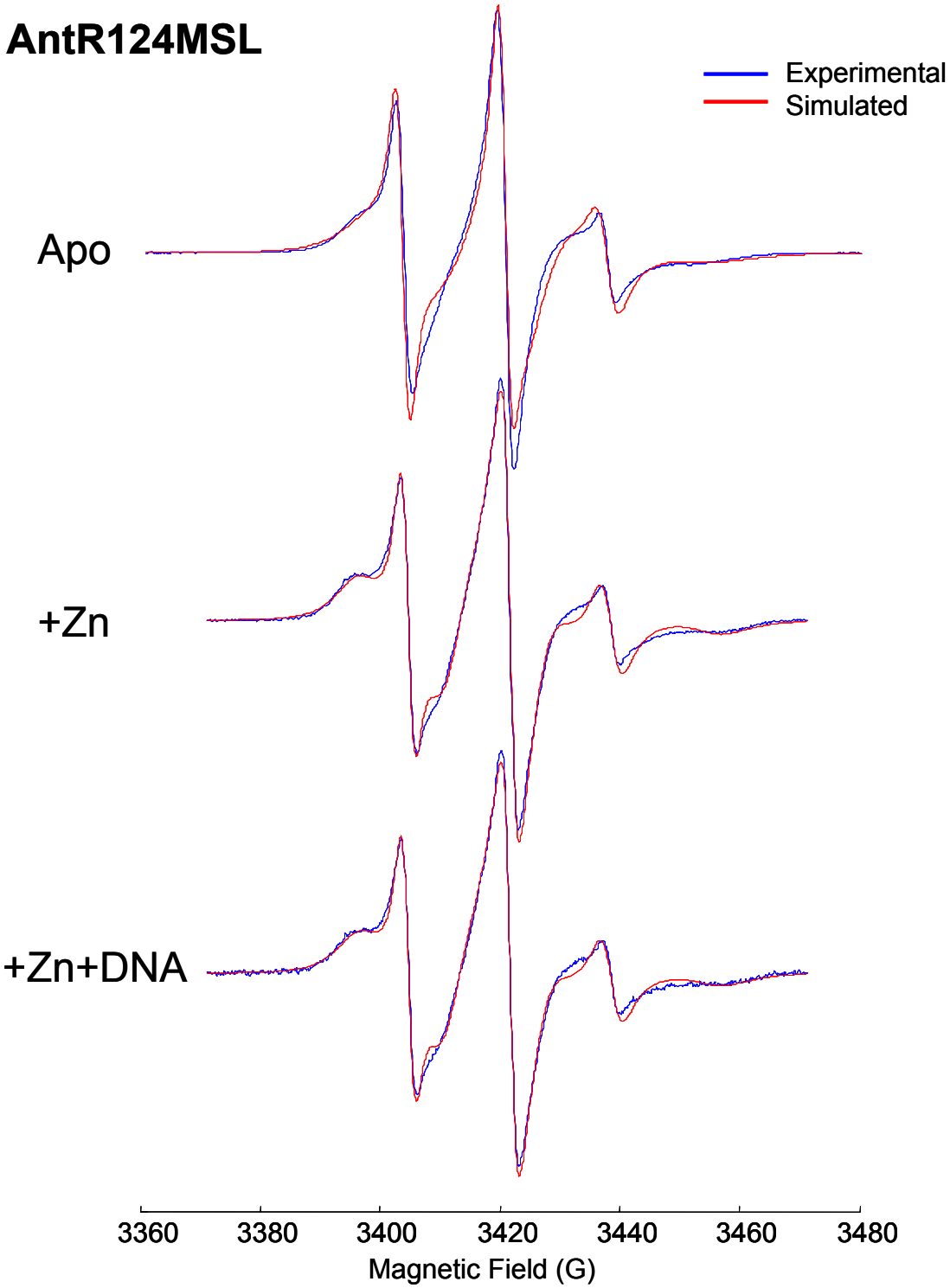

Figure 4-7: EPR spectra of MSL labeled AntR124C samples (red) and their simulations (blue).

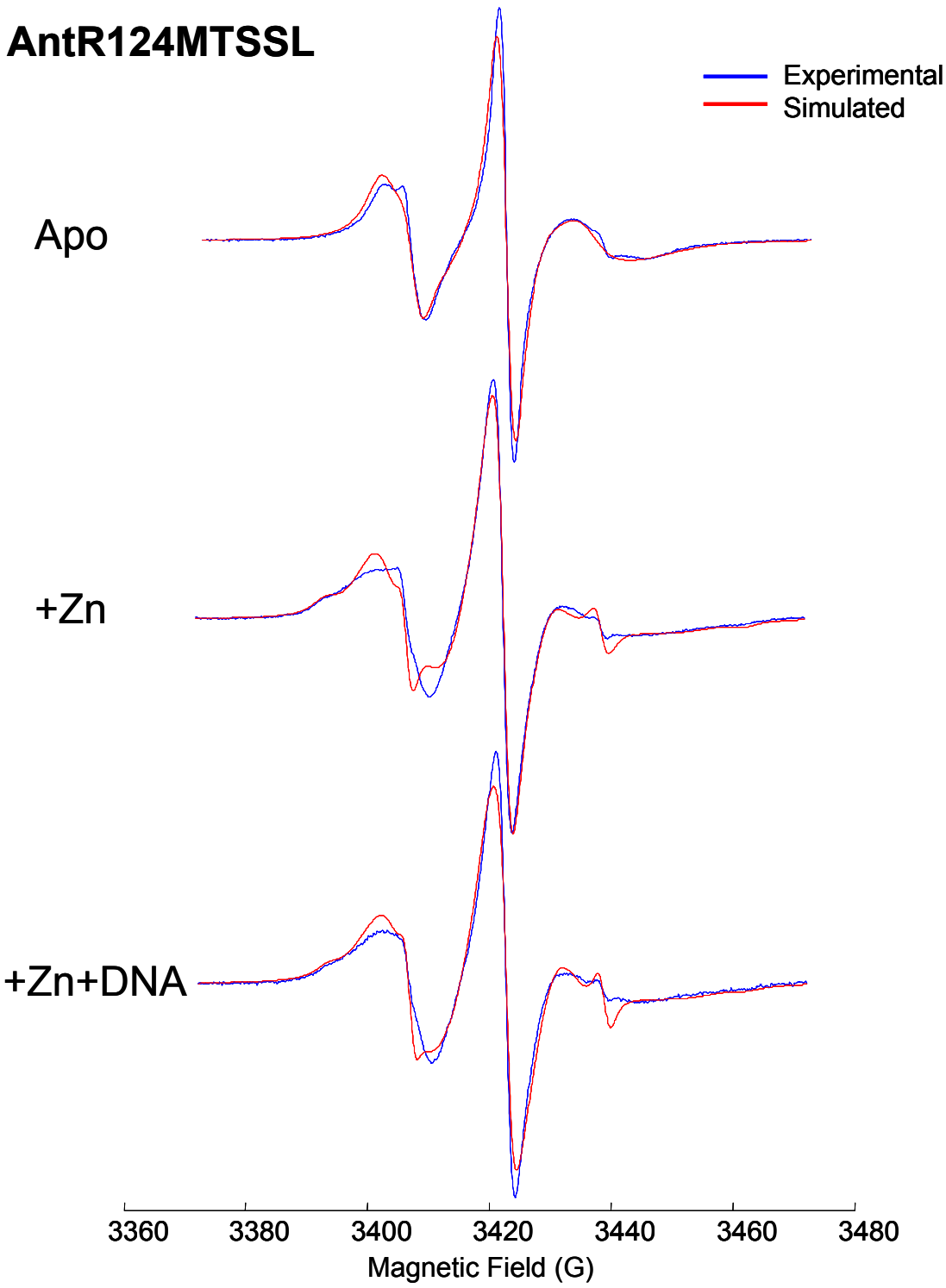

Figure 4-8: EPR spectra of MTSSL labeled AntR124C samples (red) and their simulations (blue)

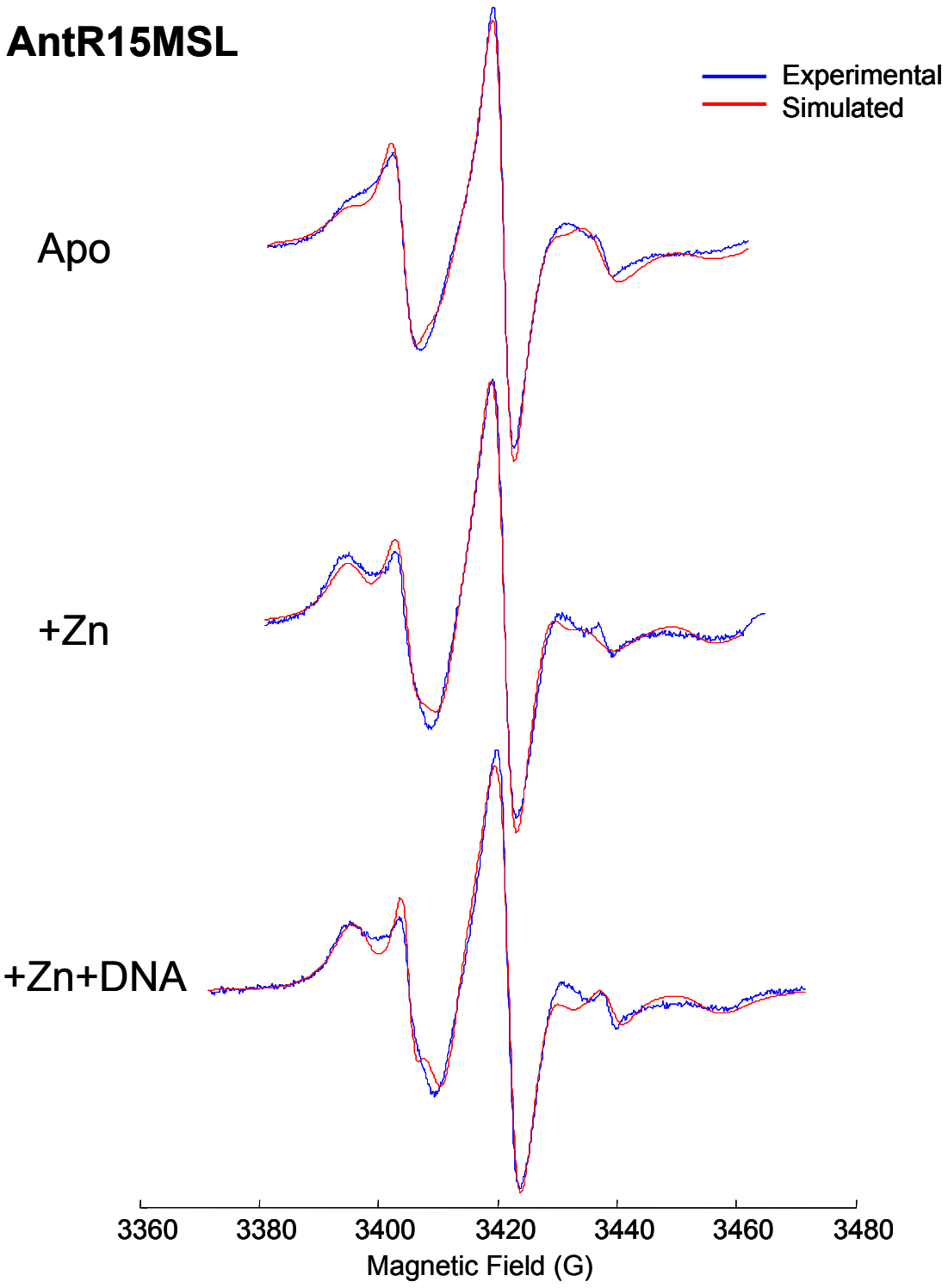

Figure 4-9: EPR spectra of MSL labeled AntR15C samples (red) and their simulations (blue).

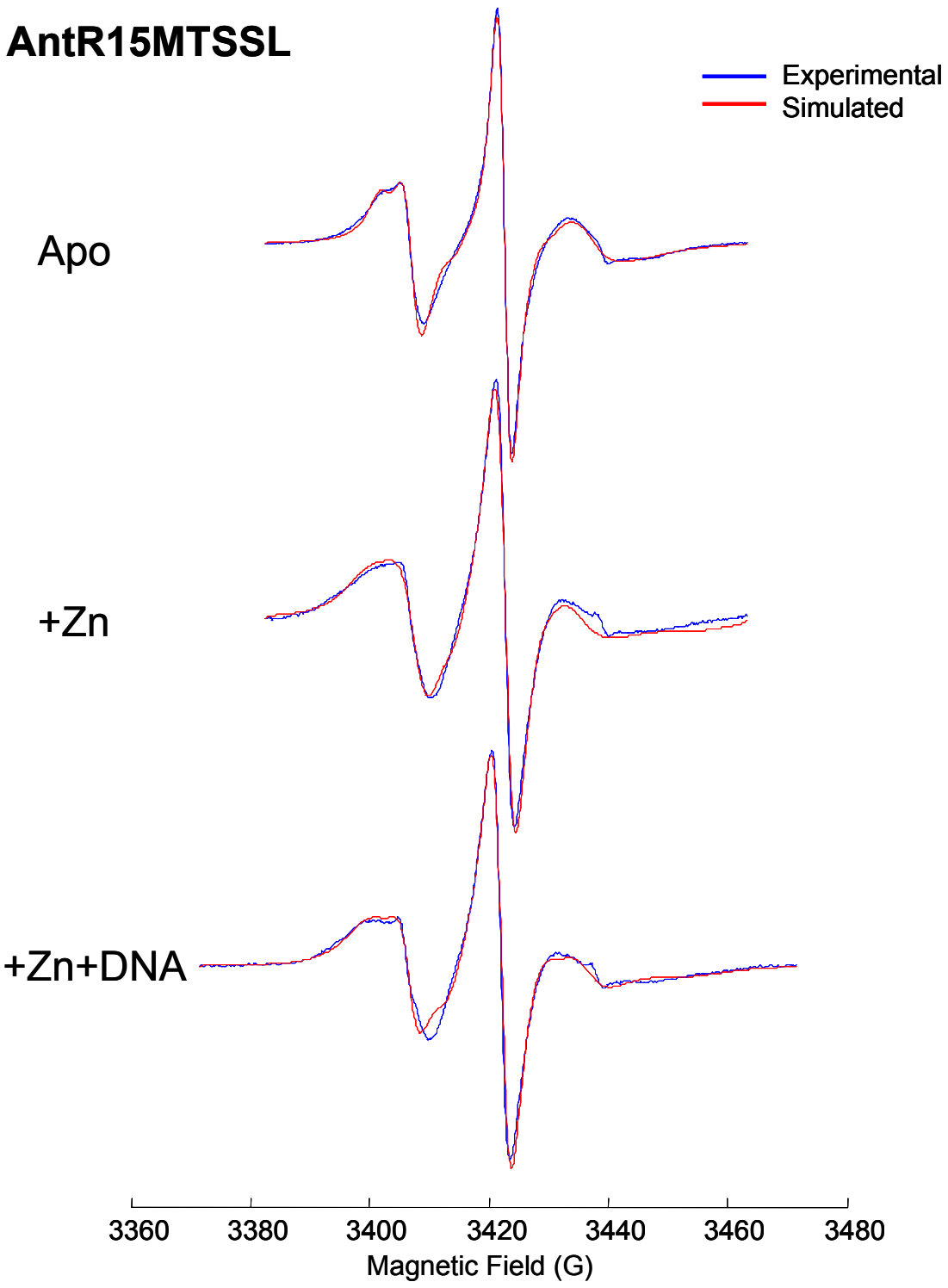

Figure 4-10: EPR spectra of MTSSL labeled AntR15C samples (red) and their simulations (blue).

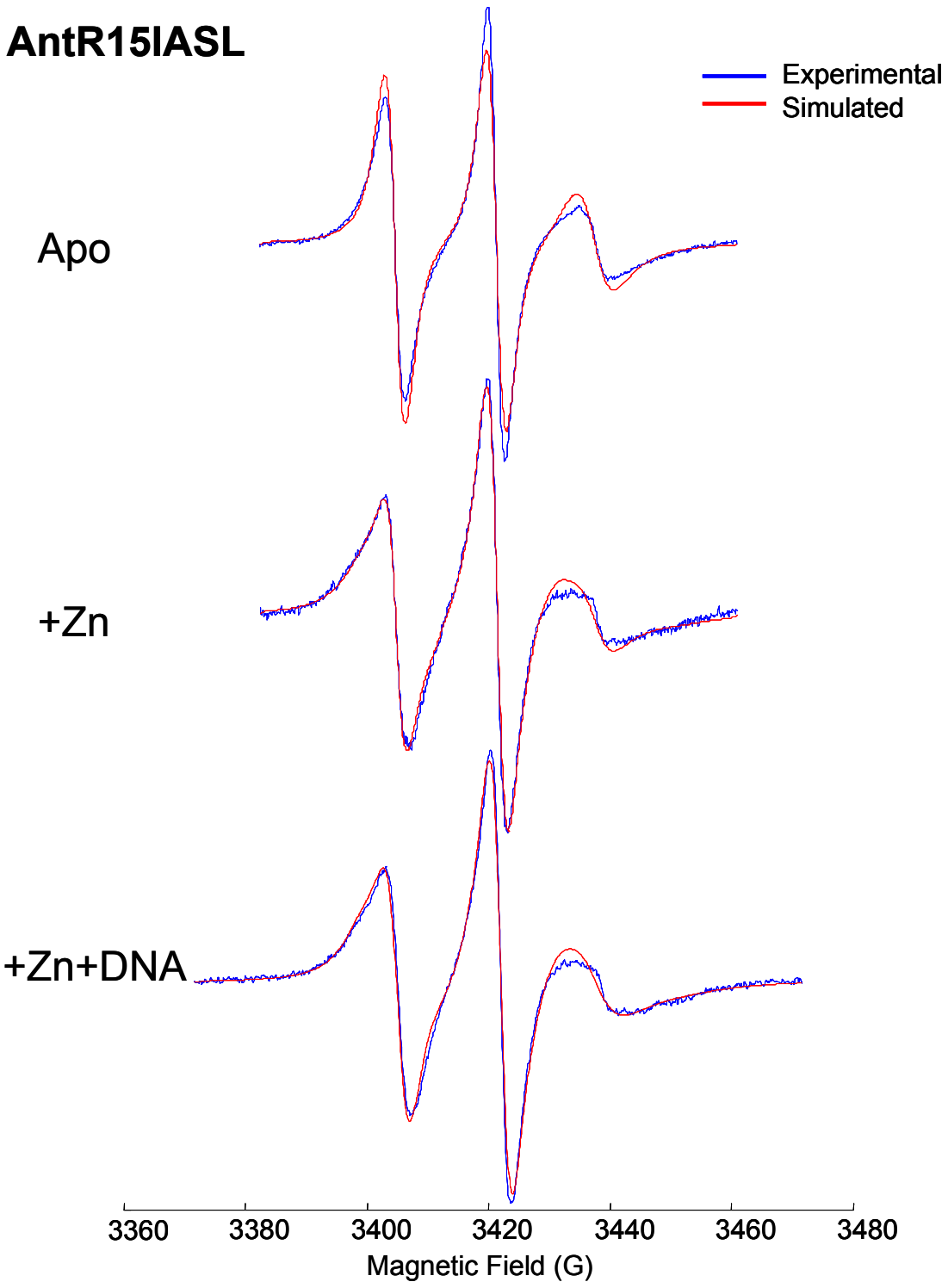

Figure 4-11: EPR spectra of IASL labeled AntR15C samples (red) and their simulations (blue).

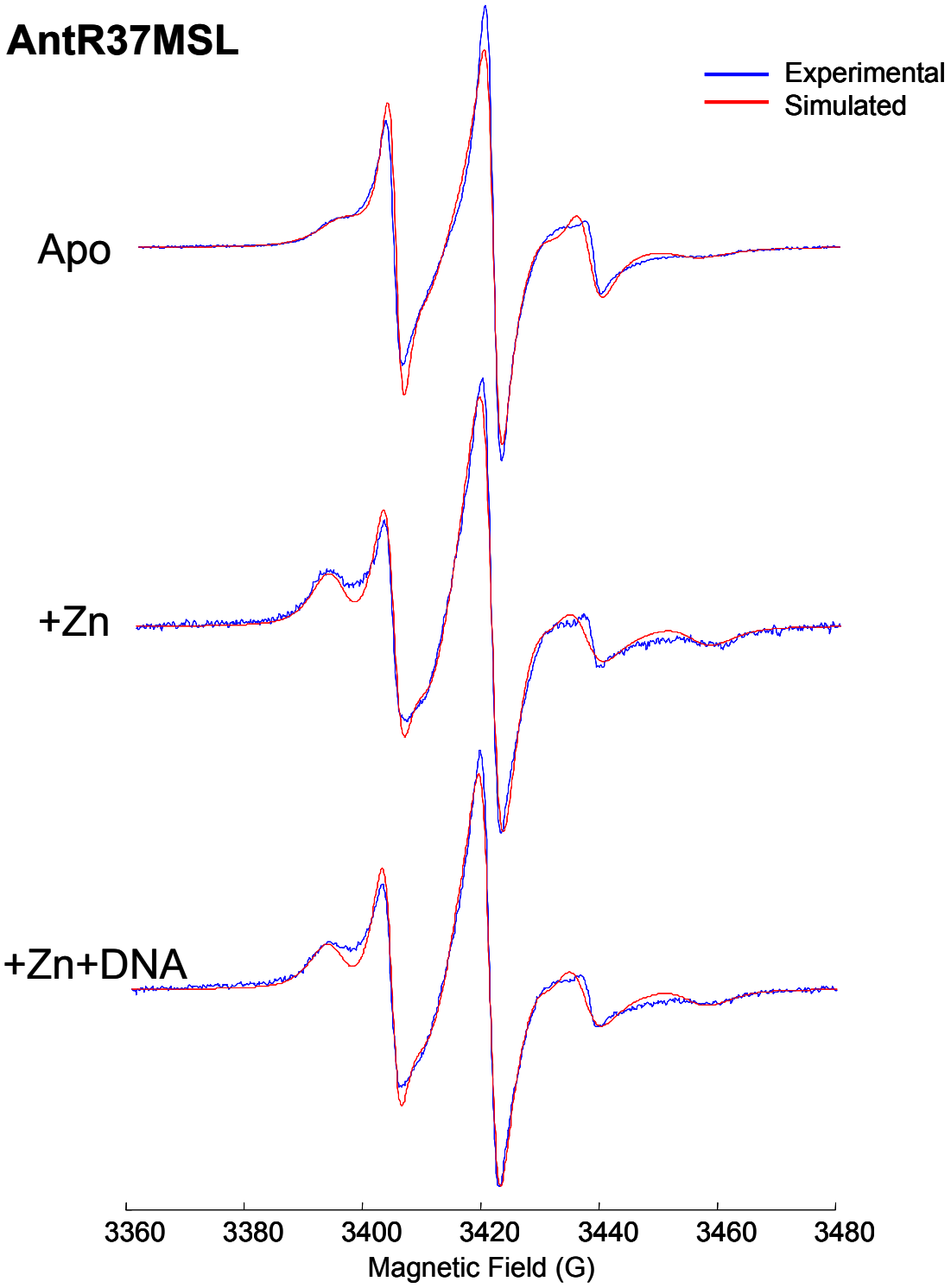

Figure 4-12: EPR spectra of MSL labeled AntR37C samples (red) and their simulations (blue).

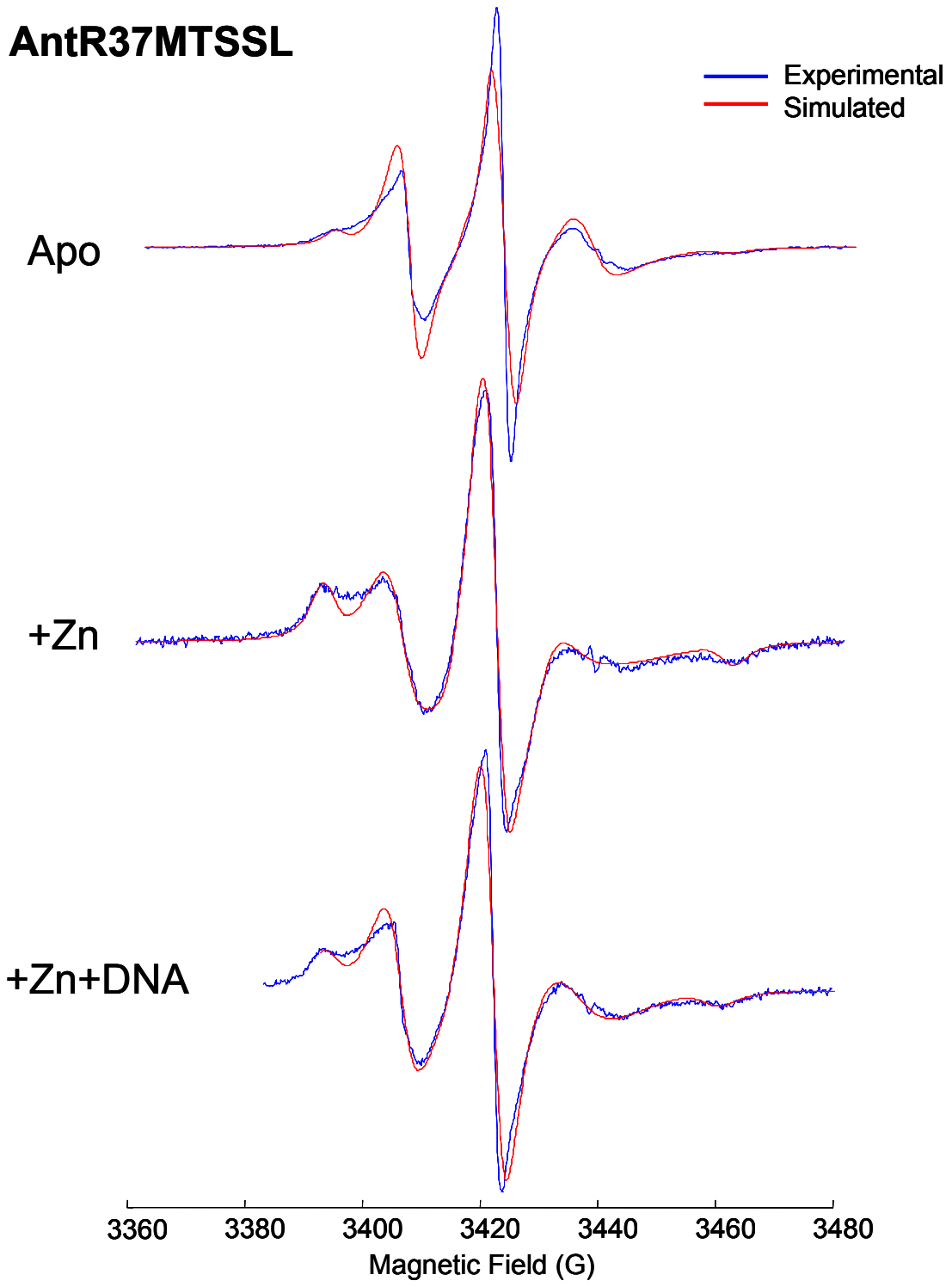

Figure 4-13: EPR spectra of MTSSL labeled AntR37C samples (red) and their simulations (blue).

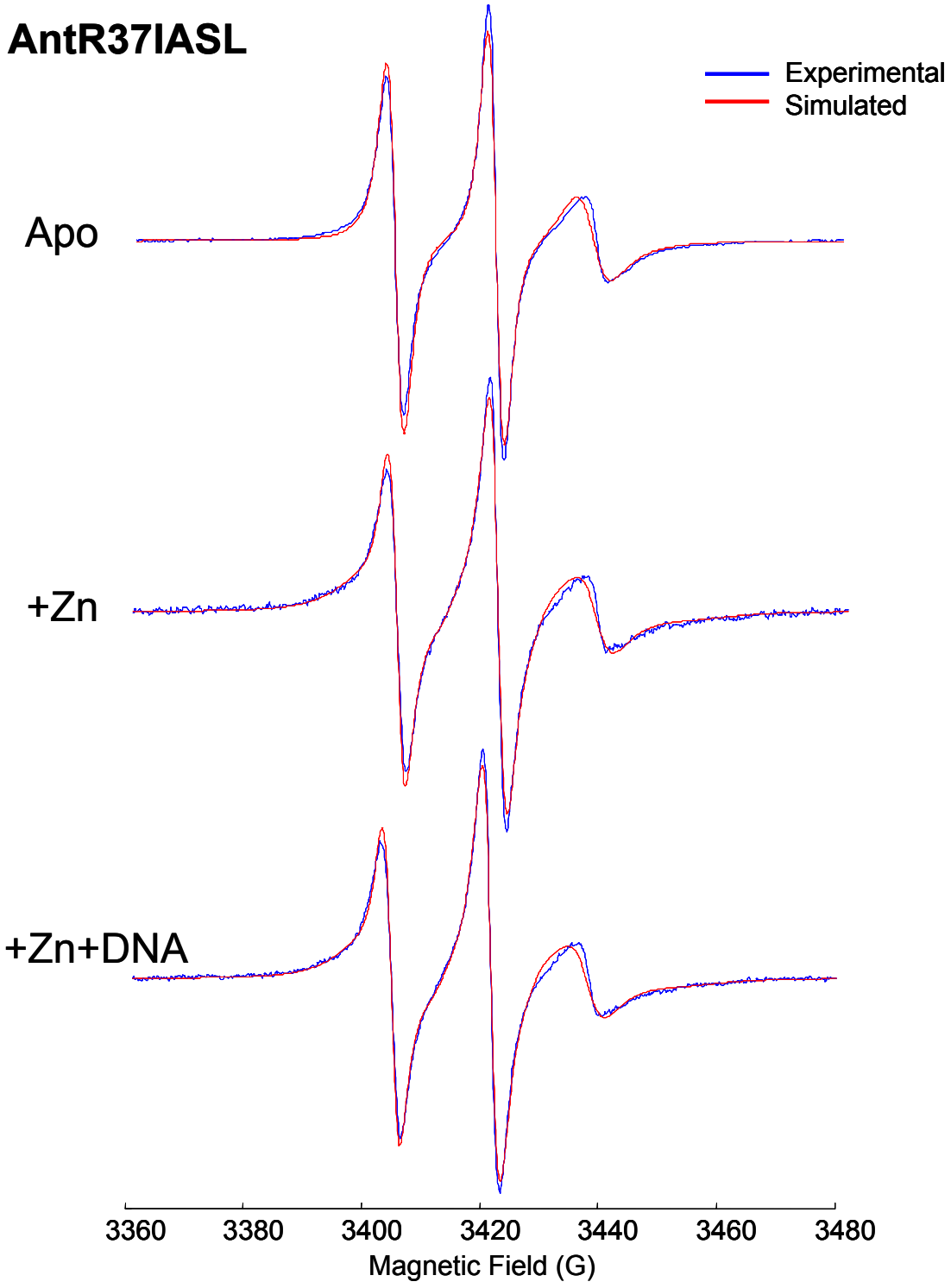

Figure 4-14: EPR spectra of IASL labeled AntR37C samples (red) and their simulations (blue).

4.3.3. Backbone conformations at the DNA binding motif

Structural rearrangement of the monomers in the dimer is subtle and not likely to affect the mobility of the side chains unless they are at the subunit interface. However, the changes in the monomer arrangement can be determined by changes in the inter-monomer distances. The distances between the monomers were estimated from dipolar interactions between the labels at equivalent sites in each monomer using the same three sites as the previous section: 15C, 37C and 124C. Since the distances were longer than 1.8 nm and the dipolar broadening of already broad cw spectra is small and difficult to extract, we used pulsed DEER experiment which is sensitive to only dipolar interactions. The dipolar evolution signals of 4-pulse DEER experiments of spin labeled apo and metal bound AntR mutants as well as the Gaussian population analysis are shown in Figure 4-15 - Figure 4-18. The fit parameters are summarized in Table 4-2. The detailed description of the figure panels is described in Chapter 2.

There are no significant differences between MSL and MTSSL labeled AntR124C distance distributions in both apo and Zn(II) bound states (Figure 4-15). The center distance of the major population (r_1) in these four samples are 3.0 to 3.1 nm (±0.3), and the widths (w_1) vary between 0.5 nm and 0.9 nm, as shown in the central panel. At site 124, MTSSL-labeled holo AntR, and MSL labeled apo and holo AntR have small (< 23%) populations at r_2=4.2 and 5.3 nm respectively, which are broader than the shorter distance (w_2=1.7-3.0 nm). These minor populations are not well defined as reflected in the large error values (±0.7 to ±1.0 in r_2, and ±1.7 to ±2.5 nm in w_2).

In Figure 4-16, the mean distance of the first population for site 15 is 0.6 nm shorter in MTSSL (r_1=3.4 ±0.2 nm for apo and r_1=3.6 ±0.2 nm for holo) than IASL and MSL (r_1= 4.0-4.1 nm), suggesting a unique orientation for this label. Addition of Zn(II) decreases the width of the overall distance distribution by ~0.7 nm, but introduces only small changes in the widths of Gaussians for MSL and IASL (Table 4-2), again suggesting that MTSSL adapts a unique conformation. The major difference between the data in Figure 4-16 is the widths of distance distributions across different spin labels This can also seen directly from the amplitudes of oscillations in the time domain data (left panel in Figure 4-16). IASL yields the narrowest

distance distribution with w_1=0.4 ±0.8 nm (apo) and w_1=0.7 ±0.5 nm (holo), followed by MTSSL with w_1=0.6 ±0.4 nm (apo) and w_1=0.7 ±0.4 nm (holo), and the largest being MSL with w_1=1.5 ±0.4 nm (apo) and w_1=0.8 ±0.7 nm (holo) (Table 4-2). Therefore, the protein backbone heterogeneity at this site has a maximum contribution of 0.4 nm to the distance between spin labels, and any distribution broader than 0.4 nm is due to variety of conformations assumed by spin label.

Comparison of apo and holo states of the protein (Figure 4-16 and Table 4-2) on site 15 revealed no major change in mean distances induced by Zn(II) binding ($|r_1^{apo} - r_1^{holo}| \leq 0.2$ nm, $|r_2^{apo} - r_2^{holo}| = 0.1$ nm). We observed only minor changes in the widths of the populations ($|w_1^{apo} - w_1^{holo}| \leq 0.7$ nm for MSL, $|w_1^{apo} - w_1^{holo}| = 0.1$ nm for IASL and MTSSL, $|w_2^{apo} - w_2^{holo}| = 0.6$, 1.0, and 1.9 nm for MSL, IASL, and MTSSL respectively) that might not be significant in view of large errors (±0.4 to ±0.8 nm for w_1, ±0.3 to ±3.2 nm for w_2). As with site 124, the broad populations on site 15 are associated with large errors (±0.8 to ±2.3 nm for r_2, ±1.9 to ±3.2 for w_2).

Residue 37 is on the DNA binding helix-turn-helix motif of AntR. The structural changes on this region are related directly to the activation pathway for DNA recognition upon metal binding. The spin labels of AntR37C display the most prominent distance changes on binding of metal (Figure 4-17). In the apo form of the repressor, all three spin labels, MSL, MTSSL and IASL, are separated by 4.2-5.5 nm, with broad distribution widths ranging from 4.6 nm to 5.0 nm for the major population. A surface exposed residue such as site 37, which is not restricted by nearby residues or tertiary interactions, is expected to have a large distance disribution. However, spin label side chains are 0.5 to 1 nm in length, and hence may contribute as much as 4 nm to distance distribution width. Larger widths as seen here, must be due to multiple backbone conformations. In the presence of Zn(II), the distances shorten to 3.2-3.5 nm and the widths of distributions narrow significantly (w = 2.7 - 3.9 nm). DNA binding did not induce further changes in distances (Figure 4-18).

Another parameter that is derived from the DEER experiments is the fraction of the coupled spins (f_Δ), i.e. the ratio of dipolarly coupled spins on a protein dimer (that are within an

interaction distance of 1.8 to 6 nm of each other) to total number of spins in the sample. The larger is the coupled population the deeper is the echo modulation with respect to the overall echo intensity (Δ).

The small increase or decrease in Δ (Table 4-2) upon binding of metal does not follow a particular trend. AntR15IASL seems to have very low modulation depths: 5.6±0.2% and 7.9±0.2% in the absence and presence of metal. This low modulation depth suggests that a significant population of the spin labels is separated by distances outside the sensitivity range of

Table 4-2: Distance distribution from DEER experiments

	Δ (%)	f_Δ	r_1 (nm)	w_1 (nm)	%	r_2 (nm)	w_2 (nm)	%	$F_{1\to2}$	$F_{2\to3}$	$P_{1\to2}$	$P_{2\to3}$
124MTSSL apo	17.9±0.8	0.63	3.0±0.2	0.5±0.5	100				1.13		0.21	
124MTSSL Zn	17.2±1.0	0.60	3.0±0.3	0.6±0.6	77	4.2±0.7	1.7±1.7	23	1.36	0.98	0.02	0.55
124MSL apo	14.6±0.2	0.50	3.1±0.2	0.9±0.4	89	5.3±1.0	3.0±2.5	11	3.50	0.98	0.00	0.54
124MSL Zn	15.6±0.8	0.54	3.1±0.3	0.9±0.6	79	4.2±1.0	2.1±2.4	21	1.84	0.95	0.00	0.62
15MTSSL apo	17.1±0.6	0.59	3.4±0.2	0.6±0.4	43	4.0±0.5	1.2±0.3	57	1.83	0.79	0.00	0.97
15MTSSL Zn	21.7±0.6	0.78	3.6±0.2	0.7±0.4	80	4.1±0.8	3.1±1.9	20	1.91	0.98	0.00	0.55
15MSL apo	12.5±0.5	0.42	4.0±0.3	1.5±0.4	75	4.6±1.1	4.9±2.5	25	2.19	0.99	0.00	0.53
15MSL Zn	24.0±2.0	0.87	4.1±0.5	0.8±0.7	38	4.7±1.0	4.3±2.4	62	1.46	0.99	0.01	0.52
15IASL apo	5.6±0.2	0.18	4.0±0.4	0.4±0.8	49	4.3±1.8	3.7±2.0	51	1.35	0.99	0.02	0.52
15IASL Zn	7.9±0.2	0.26	4.0±0.3	0.7±0.5	61	4.2±2.3	4.7±3.2	39	1.43	0.99	0.01	0.53
37MTSSL apo	19.1±0.9	0.67	4.8±0.4	1.0±1.3	23	5.5±1.1	5.0±1.0	77	1.61	1.12	0.00	0.23
37MTSSL Zn	14.4±0.2	0.49	3.4±0.4	2.7±1.1	100	-	-	-	1.20	-	0.12	-
37MTSSL ZnDNA	15.4±0.3	0.53	3.4±0.5	3.9±1.4	53	3.5±0.8	1.4±0.8	47	1.79	0.97	0.00	0.56
37MSL apo	13.8±0.4	0.47	4.4±0.5	4.6±1.1	100	-	-	-	1.13	-	0.19	-
37MSL Zn	17.4±0.2	0.61	3.2±0.2	2.1±0.5	66	5.4±0.4	3.9±1.1	34	3.91	1.01	0.00	0.47
37MSL ZnDNA	16.0±0.5	0.55	3.4±0.3	2.5±0.5	92	6.3±2.1	4.2±4.2	8	1.49	0.97	0.02	0.56
37IASL apo	12.4±1.0	0.42	4.2±1.1	5.0±1.1	63	4.3±0.4	1.6±0.8	37	1.37	1.00	0.02	0.50
37IASL Zn	14.8±0.5	0.51	3.5±0.4	3.1±1.1	100	-	-	-	1.08	-	0.30	-
37IASL ZnDNA	13.8±0.4	0.47	3.3±0.5	1.3±0.7	31	3.6±0.4	3.4±0.8	69	1.91	0.98	0.00	0.53

Δ is the modulation depth, which is defined as the percentage ratio of intensity of the pure echo modulation to total echo intensity; f_Δ is the corresponding fraction of coupled spins in the sample, calculated from modulation depth of calibrated sample (biradical); r is the center distance, w is the width, and % is the percentage contribution of a Gaussian population; F and P are the statistical F-test values comparing 1 Gaussian model to 2 Gaussians model in the fitting (subscript 1→2), or 2 Gaussians to 3 (2→3).

the DEER experiment (r > ~6 nm). The other spin labels attached to site 15 display larger modulation depths, therefore conformers responsible for the large separation are specific to IASL sample. This is probably not due to unfolding of the protein caused by spin labeling since DNA shift assays showed complete binding of AntR15IASL to target sequence (Figure 4-3), but due to a "stretched-out" conformation of the IASL label where the nitroxides are separated by more than 6 nm.

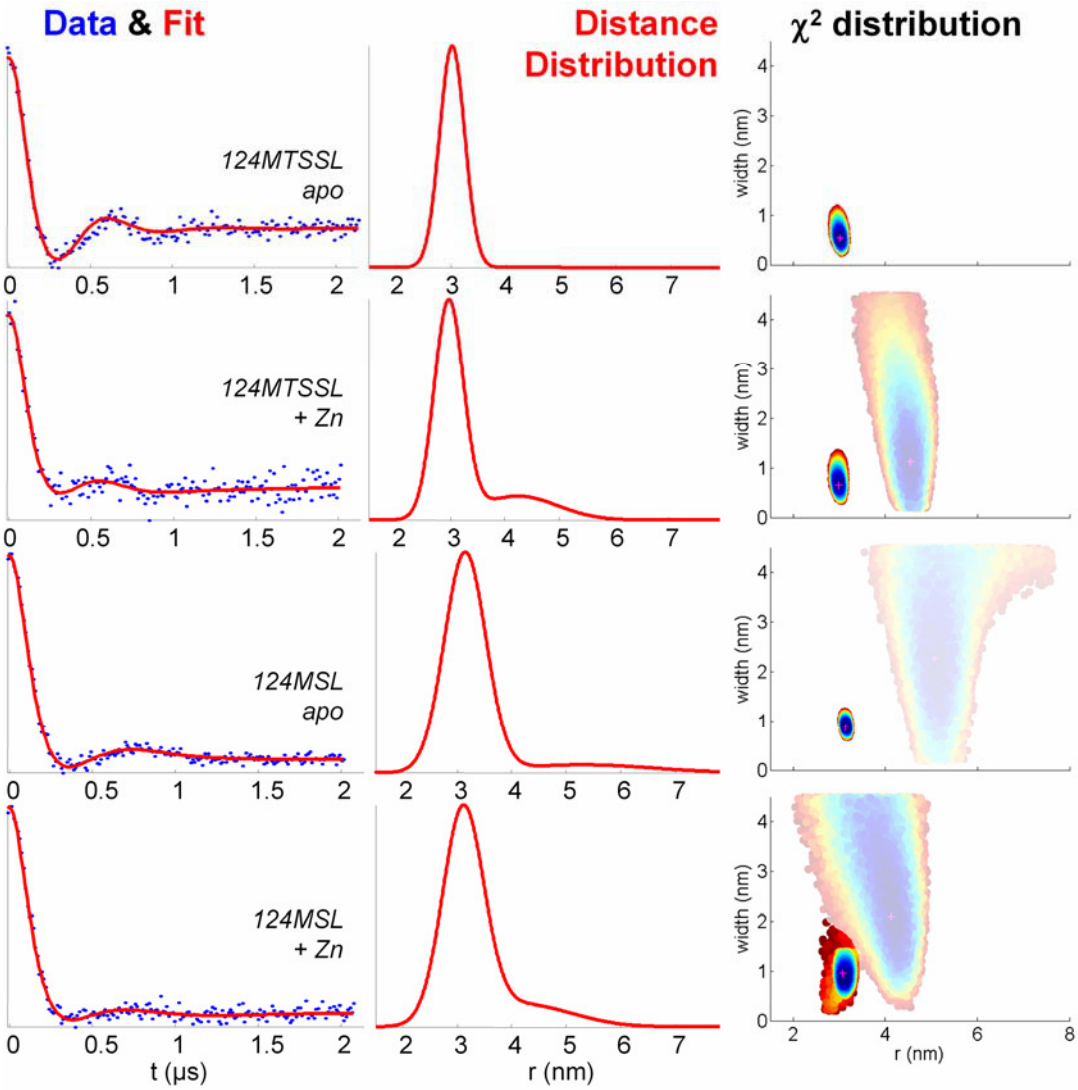

Figure 4-15: Distances across AntR dimer. DEER data (left panel, blue points), fits (left panel, red line), resulting distance distributions (center panel), χ^2 surface (right panel), for each spin labeled AntR mutant. Labeling site and spin label type are indicated on left column.

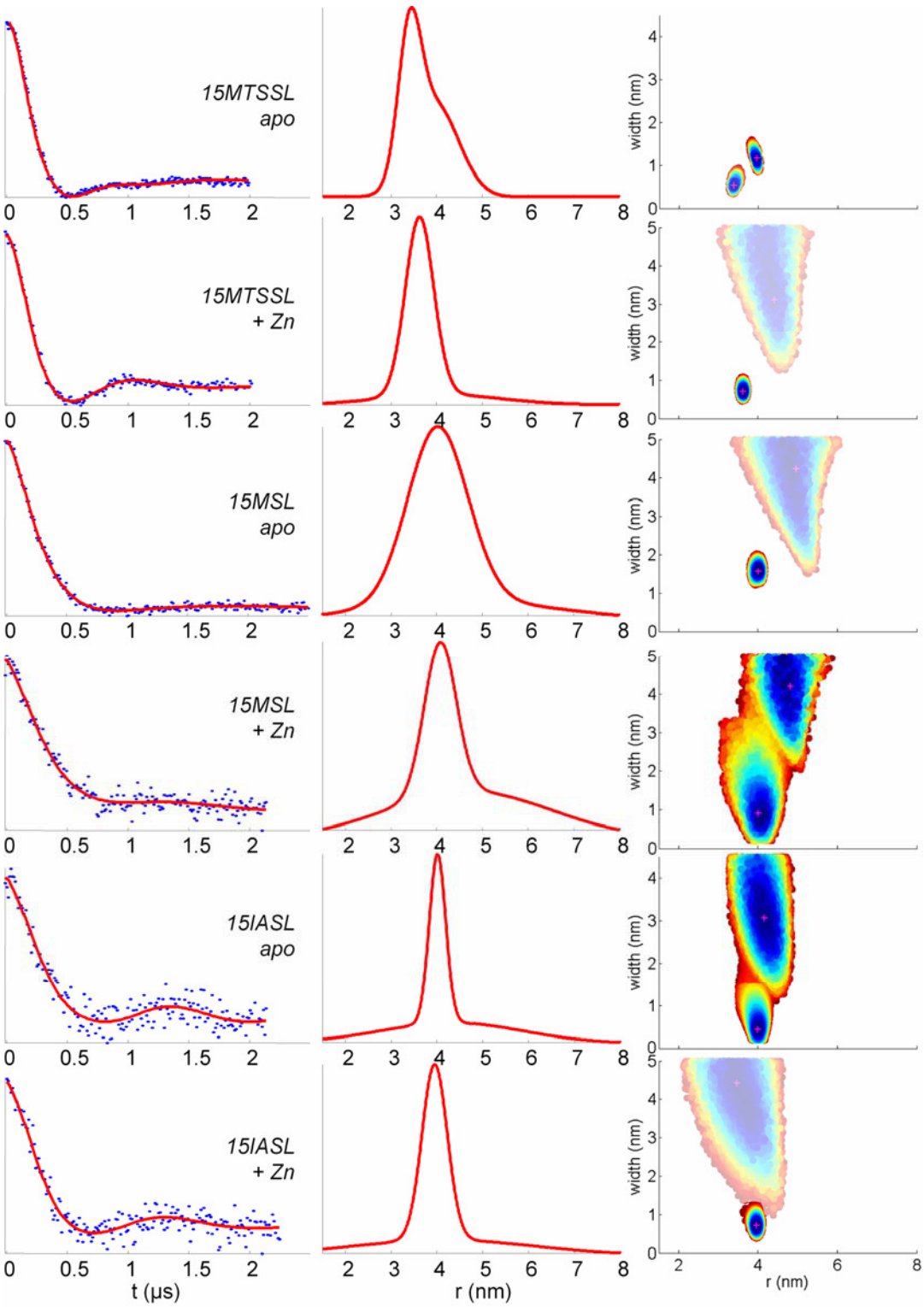

Figure 4-16: DEER data and analysis of spin labeled AntR15C (see figure 4-15 legend)

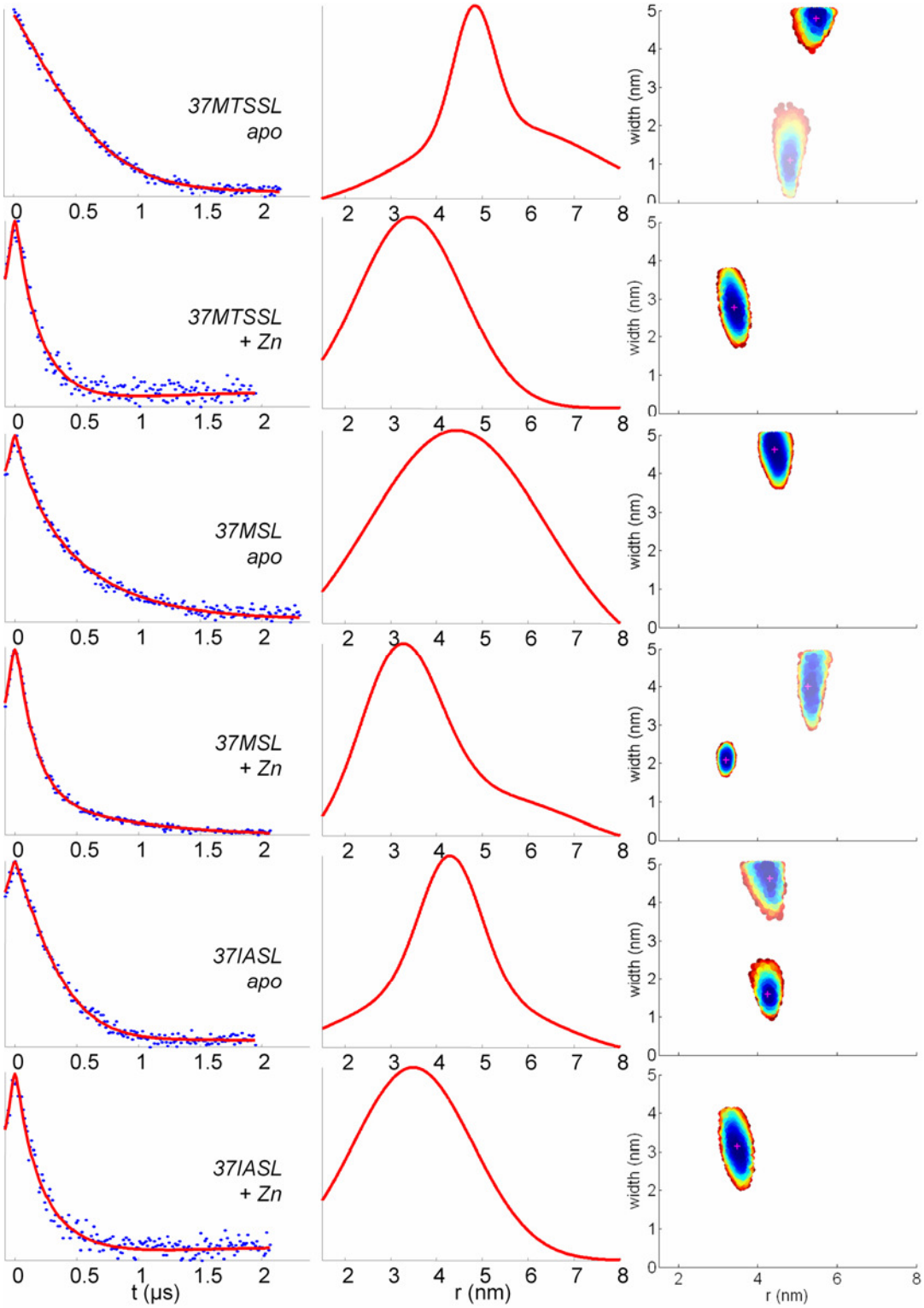

Figure 4-17: DEER data and analysis of spin labeled AntR37C (see figure 4-15 legend)

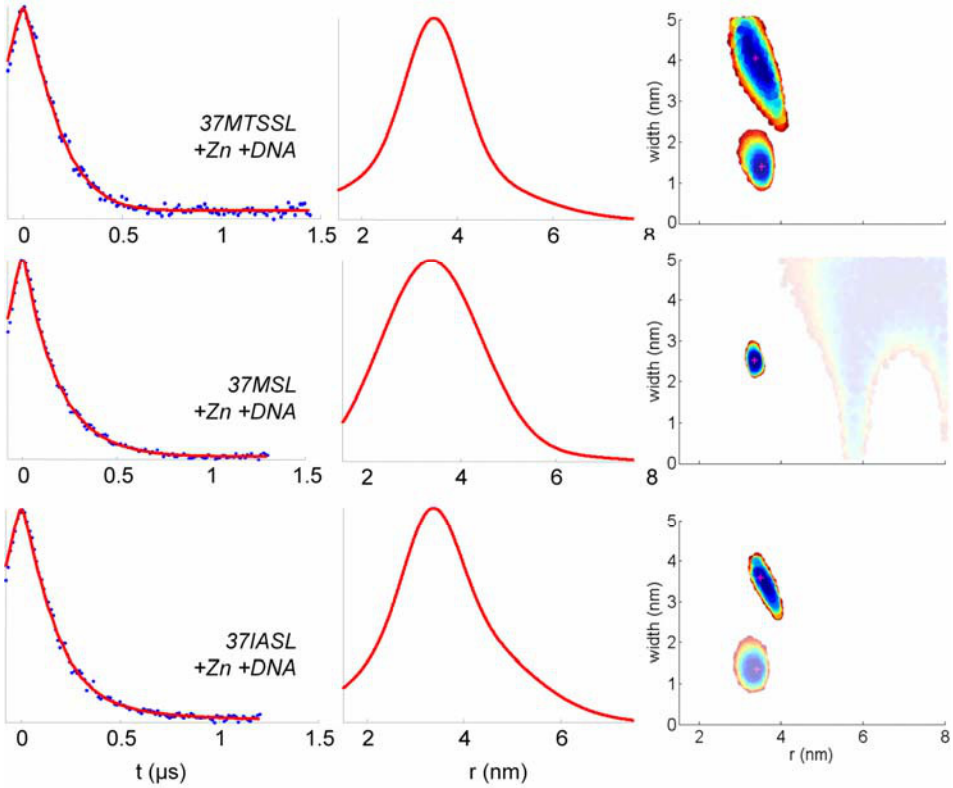

Figure 4-18: DEER data and analysis of spin labeled AntR37C in presence of Zn(II) and target DNA

4.3.4. Modeling of Spin Label Conformations.

The source of the experimentally observed distance width is the heterogeneity of the backbone conformations, as well as the presence of multiple conformers of spin labels. To account for multitude of label conformers and the resulting spread of distances we have modeled possible label rotamers using crystal structure of homologous MntR. The lowest energy spin label rotamers were determined by a) Metropolis Monte Carlo Minimization (MMCM) within rigid structure of a protein and by b) Molecular Dynamics (MD) which allows movement of the protein side chains and backbone.

The distance between the spin labels from MMCM is plotted as a Boltzmann weighted probability while the MD distances are pooled from 2-4 ns trajectories as described in the Methods section. For spin labels on site 124 (Figure 4-19) the simulations differ by 0.7-1.0 nm from the shorter distance of the experimental results. As seen in the figure, computationally

generated rotamers do not account for the minor, broad populations. The experimental distances for these small populations are associated with large errors (Table 4-2) and are not well defined. On site 15, for all spin labels there is ~1.0 nm difference between the simulated and experimental distances, within range of the combined errors of data (±0.2 to 0.5 nm, Table 4-2) and modeling (±0.3 to 0.5 nm, (Sale et al., 2005)). The simulated distances on site 15 have narrower distributions than the experimentally observed distances. . As with site 124, the broad population in the experimental data are not well-defined, and hence do not constitute a disagreement between modeling and data. On site 37, the modeled mean distances are shorter than seen in the experimental data, but within the error range. Here, both the simulated and the experimental distances are broad, although wider distributions are observed in the experimental data. There seems to be a larger backbone heterogeneity at the DNA binding region than the dimerization interface and metal binding sites, because of these broad distance distributions.

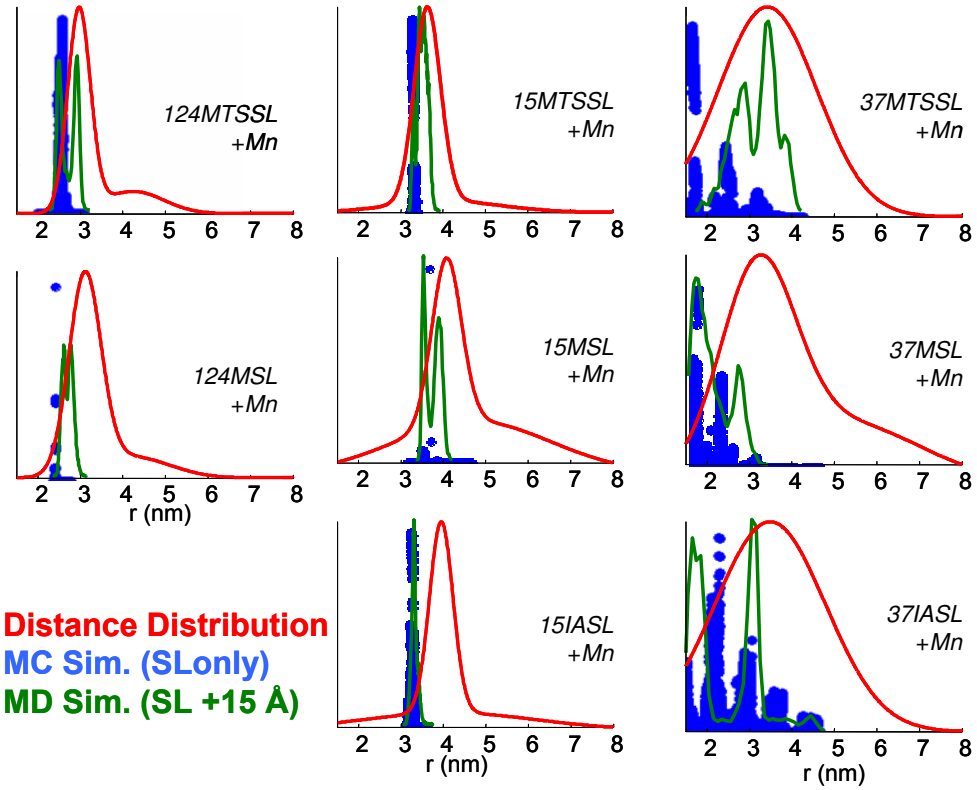

Figure 4-19: Distances across metal activated AntR dimer. Experimental distance distributions (red), distances from Monte Carlo (blue points) and molecular dynamics (green) simulations are shown for each spin labeled AntR mutant.

4.4. Discussion

The conformational changes associated with metal binding in the activation of the Anthracis Repressor were determined by measuring side chain dynamics and the distances between equivalent positions in dimeric AntR. Both the size exclusion chromatography and the pulsed EPR experiments indicated that the repressor is a dimer in the absence of the activating metal. Thus, metal binding is not necessary for a formation of a dimer as seen in DtxR and IdeR. Our studies clearly show that the main effect of the metal binding is the restriction of side chain and backbone dynamics. This effect is most dramatic in residues forming the DNA binding region as the distances between two out of three site pairs in a dimer remain constant but the third (DNA binding region) decreases considerably.

Our finding of the dimeric structure of AntR is not surprising since as all DtxR family proteins function as metal-activated dimeric proteins. It seems that in some of these repressors the dimerization is regulated by metal binding. For example, the affinity of DtxR increases 100-fold in the presence of metal (from K_D of ~ 3 μM to 33 nM (Spiering et al., 2003)), similar to IdeR (Semavina et al., 2006). In contrast, MntR and MDR1 appear to be largely dimeric in the apo state, with little change in dimer affinity upon metal binding (Lieser et al., 2003; Sen et al., 2006). Our size exclusion chromatography and DEER experiments indicate that AntR resembles MntR rather then DtxR. The apo protein eluted from the size exclusion column at the size corresponding to a dimer with no observable amount of monomers, (Figure 4-4). DEER experiments on singly labeled apo-AntR monomer showed strong modulation of the echo intensity from singly spin labeled (Figure 4-15) which implies oligomer formation. The fraction of the protein in the dimeric form can be estimated from the modulation depth and was varying between 0.42 and 0.87 depending on the samples. Importantly, there was no significant shift in the modulation depths of holo-AntR samples as compared to apo-AntR. Thus, apo AntR is a dimer and metal binding is not needed for dimerization as expected for other repressors (Semavina et al., 2006; Spiering et al., 2003).

As suggested by Lieser *et al.* on the basis of MntR, and now with the added case of AntR, there appears to be a general trend that the single-domain members of the DtxR family (AntR, MntR) exhibit a higher affinity for dimer formation in the apo state than the two-domain proteins (DtxR, IdeR), and that the amount of dimer is not regulated by metal binding. The increased dimerization of single-domain members most likely results from the more extensive dimer interface observed in crystal structures of single domain proteins, compared to that of the two-domain subfamily. The increased interface is due to presence of an extra helix in MntR that is lacking in DtxR and IdeR. We presume that a similar extended dimer interface would exist in AntR due to high sequence homology with MntR.

Although the activation scheme DtxR and MntR was a subject of several biochemical studies (Golynskiy *et al.*, 2005; Lieser *et al.*, 2003; Love, 2003; Manabe *et al.*, 2005; Marin *et al.*, 2003; Que *et al.*, 2000; Rangachari *et al.*, 2004; Schmitt, 2002; Spiering *et al.*, 2003; Tao *et al.*, 1995), the structural pathway is mostly unknown. One structural scenario, disorder-to-order transition induced my metal binding and leading to dimerization, was advanced for DtxR (Twigg *et al.*, 2001). AntR, however, is already a dimer in the absence of metal and clearly a somewhat different mechanism for metal induced activation is expected. One possibility is the conformational change within a monomer, another is the rearrangement of the monomers within the dimer, and a final possibility is the change of protein dynamics.

The second scenario is unlikely in the observed insensitivity of distances to metal binding for spin labels at sites 15 and 124 (Figure 4-15 and Figure 4-16). It was particularly surprising to see similar distances at residue 15 in apo and holo forms due to its close proximity to the metal binding site. The absence of change on two sites argues against a rigid body reorientation of the monomers. The first scenario is more plausible since the distances between the DNA binding region change by ~1-2 nm for all three labels. The spin labels have different structures and lengths, and thus the changes experienced by all three is most probably due to protein conformational change, rather than some local structural ordering that only affects the spin label conformation. Such a large change between the DNA binding helices while keeping the other two distances constant requires a structure change within the monomer. One can only speculate

that bringing the DNA binding helices into proximity of each other facilitates DNA binding in a pincer-like fashion.

The third scenario is supported by data from both cw EPR and from the width of the distance distributions determined by DEER. Binding of metal resulted in the decreased flexibility for all three labels at all the three sites indicating a general decrease in backbone motion. Furthermore, close inspection of the distance distributions from DEER on DNA binding region reveals general trend of decreasing conformational heterogeneity as reflected in the width of distance distribution. Taken together, the data support the decrease of protein dynamics accompanying the metal binding.

Interestingly, the DNA binding did not induce any additional conformational changes over those induced by metal binding. Apparently, metal binding poised the structure of the repressor in the functionally competent state.

In summary, the work presented here offers an interesting activation scenario: the repressor exists as a dimer even in the absence of the metals. The dimer is quite flexible exhibiting nanosecond backbone dynamics. Metal binding brings the DNA binding regions of the two monomers in the proximity that facilitates DNA binding. The metal binding also decreases protein dynamics – protein stiffens up. DNA binding does not induce any further structural changes. Thus, the activation of AntR repressor is one of the growing examples of proteins regulated primarily by the protein dynamics in addition to conformational changes.

APPENDIX A.

DNA AND PROTEIN SQUENCES

A.1. AntR's Amino Acid Sequence

MPTPSMEDYIEQIYLLIDEKGYARVSDIAEALSVHPSSVTKMVQKLDKDEYLIYEKYRGL
VLTSKGKKIGERLVYRHELLEQFMRIIGVDESKIYNDVEGIEHHLSWEAIDRIGDLVQYFE
QDEVRVETLRGVQKANEEKSN

A.2. AntR's Nucleic Acid Sequence

5'ATGCCTACCCCTAGTATGGAAGATTATATTGAACAAATTTATTTGTTGATTGATGA
AAAGGGTTATGCCCGCGTATCTGATATTGCTGAAGCGCTTAGTGTACATCCATCCTC
TGTAACAAAAATGGTGCAAAAATTAGACAAAGATGAATATCTAATTTATGAAAAAT
ATAGAGGGCTTGTATTAACATCAAAAGGTAAAAAAATTGGAGAACGTCTCGTATAT
CGTCATGAATTGTTAGAGCAATTTATGCGTATTATCGGTGTGGATGAAAGTAAGATT
TACAATGATGTAGAAGGAATTGAACATCATTTAAGCTGGGAAGCAATTGATCGTATT
GGTGACTTAGTGCAATACTTTGAACAAGATGAGGTTCGAGTGGAAACACTTCGTGGC
GTTCAAAAAGCAAATGAAGAGAAAAGTAAT-3'

A.3. Primers used in Mutagenesis

37C
5' TTAGTGTACATCCATGCTCTGTAACAAAAATGGTGCAAAAA
5' TTTTTGCACCATTTTTGTTACAGAGCATGGATGTACACTAA

15C
5' TTATATTGAACAAATTTATTGTTTGATTGATGAAAA
5' TTTTCATCAATCAAACAATAAATTTGTTCAATATAA

124C
5' AATACTTTGAACAAGATTGTGTTCGAGTGGAAA
5' TTTCCACTCGAACACAATCTTGTTCAAAGTATT

A.4. Sequence alignment of DtxR, IdeR, MntR, and AntR

```
          1           11          21          31          41
DtxR  MKDLVDTTEM  YLRTIYELEE  EGVTPLRARI  AERLEQSGPT  VSQTVARMER
IdeR  MNELVDTTEM  YLRTIYDLEE  EGVTPLRARI  AERLDQSGPT  VSQTVSRMER
AntR  --MPTPSMED  YIEQIYLLID  EKGYARVSDI  AEALSVHPSS  VTKMVQKLDK
MntR  --MTTPSMED  YIEQIYMLIE  EKGYARVSDI  AEALAVHPSS  VTKMVQKLDK
        |           |           |           |           |
        1           9          19          29          39
          51          61          71          81          91
DtxR  DGLVVVASDR  SLQMTPTGRT  LATAVMRKHR  LAERLLTDII  GLDINKVHDE
IdeR  DGLLRVAGDR  HLELTEKGRA  LAIAVMRKHR  LAERLLVDVI  GLPWEEVHAE
AntR  DEYLIYEKYR  GLVLTSKGKK  IGERLVYRHE  LLEQFMR-II  GVDESKIYND
MntR  DEYLIYEKYR  GLVLTSKGKK  IGKRLVYRHE  LLDQFLR-II  GVDEEKIYND
          |           |           |           |           |
          49          59          69          79          88
          101         111         121         131         141
DtxR  ACRWEHVMSD  EVERRLVKVL  KDVSRSPFGN  PIPGLDELGV  GNSDAA--AP
IdeR  ACRWEHVMSE  DVERRLVKVL  NNPTTSPFGN  PIPGLVELGV  GPEPGADDAN
AntR  VEGIEHHLSW  EAIDRIGDLV  QYFEQD----  ----------  ----------
MntR  VEGIEHHLSW  NSIDRIGDLV  QYFEED----  ----------  ----------
          |           |           |
          98          108         118
          151         161         171         181         191
DtxR  GTRVIDAATS  MPRKVRIVQI  NEIFQVETDQ  FTQLLDADIR  VGSEVEI-VD
IdeR  LVRLTELPAG  SPVAVVVRQL  TEHVQGDIDL  ITRLKDAGVV  PNARVTVETT
AntR  ----------  -EVRVETLRG  VQKANEEKSN  ----------  ----------
MntR  ----------  -DARKKDLKS  IQKKTEHHNQ  ----------  ----------
                    |           |
                    124         133
          201         211         221
DtxR  RDGHITLSHN  G-KDVELLDD  LAHTIRIEEL  Primary metal binding site of DtxR
IdeR  PGGGVTIVIP  GHENVTLPHE  MAHAVKVEKV  Ancillary metal binding site of DtxR
AntR  ----------  ----------  ------      Conributes to Primary and Ancillary
MntR  ----------  ----------  ------      Putative binding site
```

Alignment was performed at the ExPASy (Expert Protein Analysis System) proteomics server (Gasteiger et al., 2003).

American Chemical Society's Policy on Theses and Dissertations

Thank you for your request for permission to include **your** paper(s) or portions of text from **your** paper(s) in your thesis. Permission is now automatically granted; please pay special attention to the implications paragraph below. The Copyright Subcommittee of the Joint Board/Council Committees on Publications approved the following:

> Copyright permission for published and submitted material from theses and dissertations
> ACS extends blanket permission to students to include in their theses and dissertations their own articles, or portions thereof, that have been published in ACS journals or submitted to ACS journals for publication, provided that the ACS copyright credit line is noted on the appropriate page(s).
> Publishing implications of electronic publication of theses and dissertation material
> Students and their mentors should be aware that posting of theses and dissertation material on the Web prior to submission of material from that thesis or dissertation to an ACS journal may affect publication in that journal. Whether Web posting is considered prior publication may be evaluated on a case-by-case basis by the journal's editor. If an ACS journal editor considers Web posting to be "prior publication", the paper will not be accepted for publication in that journal. If you intend to submit your unpublished paper to ACS for publication, check with the appropriate editor prior to posting your manuscript electronically.

If your paper has **not** yet been published by ACS, we have no objection to your including the text or portions of the text in your thesis/dissertation in **print and microfilm formats**; please note, however, that electronic distribution or Web posting of the unpublished paper as part of your thesis in electronic formats might jeopardize publication of your paper by ACS. Please print the following credit line on the first page of your article: "Reproduced (or 'Reproduced in part') with permission from [JOURNAL NAME], in press (or 'submitted for publication'). Unpublished work copyright [CURRENT YEAR] American Chemical Society." Include appropriate information.

If your paper has already been published by ACS and you want to include the text or portions of the text in your thesis/dissertation in **print or microfilm formats**, please print the ACS copyright credit line on the first page of your article: "Reproduced (or 'Reproduced in part') with permission from [FULL REFERENCE CITATION.] Copyright [YEAR] American Chemical Society." Include appropriate information.

Submission to a Dissertation Distributor: If you plan to submit your thesis to UMI or to another dissertation distributor, you should not include the unpublished ACS paper in your thesis if the thesis will be disseminated electronically, until ACS has published your paper. After publication of the paper by ACS, you may release the entire thesis (**not the individual ACS article by itself**) for electronic dissemination through the distributor; ACS's copyright credit line should be printed on the first page of the ACS paper.

Use on an Intranet: The inclusion of your ACS unpublished or published manuscript is permitted in your thesis in print and microfilm formats. If ACS has published your paper you may include the manuscript in your thesis on an intranet that is not publicly available. Your ACS article cannot be posted electronically on a publicly available medium (i.e. one that is not password protected), such as but not limited to, electronic archives, Internet, library server, etc. The only material from your paper that can be posted on a public electronic medium is the article abstract, figures, and tables, and you may link to the article's DOI or post the article's author-directed URL link provided by ACS. This paragraph does not pertain to the dissertation distributor paragraph above.

Questions? Call +1 202/872-4368/4367. Send e-mail to copyright@acs.org or fax to +1 202-776-8112. 10/10/03, 01/15/04, 06/07/06

REFERENCES

Adhikari, B.B., Somerset, J., Stull, J.T., and Fajer, P.G. 1999. "Dynamic modulation of the regulatory domain of myosin heads by pH, ionic strength, and RLC phosphorylation in synthetic myosin filaments". *Biochemistry* **38**(10):3127-3132.

Antanaitis, B.C., Brown, R.D., Chasteen, N.D., Freedman, J.H., Koenig, S.H., Lilienthal, H.R., Peisach, J., and Brewer, C.F. 1987. "Electron-Paramagnetic Resonance and Magnetic-Susceptibility Studies of Dimanganese Concanavalin-a - Evidence for Antiferromagnetic Exchange Coupling". *Biochemistry* **26**(24):7932-7937.

Baumann, B.A.J., Hambly, B.D., Hideg, K., and Fajer, P.G. 2001. "The regulatory domain of the myosin head behaves as a rigid lever". *Biochemistry* **40**(26):7868-7873.

Bell, S.D., Cairns, S.S., Robson, R.L., and Jackson, S.P. 1999. "Transcriptional regulation of an archaeal operon in vivo and in vitro". *Mol Cell* **4**(6):971-982.

Braun, V. 2001. "Iron uptake mechanisms and their regulation in pathogenic bacteria". *International Journal of Medical Microbiology* **291**(2):67-79.

Braun, V., and Killmann, H. 1999. "Bacterial solutions to the iron supply problem". *Trends in Biochemical Sciences* **24**(3):104-109.

Brown, J.S., and Holden, D.W. 2002a. "Iron acquisition by Gram-positive bacterial pathogens". *Microbes and Infection* **4**(11):1149-1156.

Brown, L.J., Sale, K.L., Hills, R., Rouviere, C., Song, L.K., Zhang, X.J., and Fajer, P.G. 2002b. "Structure of the inhibitory region of troponin by site directed spin labeling electron paramagnetic resonance". *Proceedings of the National Academy of Sciences of the United States of America* **99**(20):12765-12770.

Butler, A. 2003. "Iron acquisition: straight up and on the rocks?" *Nature Structural Biology* **10**(4):240-241.

Cammack, R., Chapman, A., Lu, W.P., Karagouni, A., and Kelly, D.P. 1989. "Evidence That Protein-B of the Thiosulfate-Oxidizing System of Thiobacillus-Versutus Contains a Binuclear Manganese Cluster". *Febs Letters* **253**(1-2):239-243.

Chae, M.Y., Omburo, G.A., Lindahl, P.A., and Raushel, F.M. 1993. "Antiferromagnetic Coupling in the Binuclear Metal Cluster of Manganese-Substituted Phosphotriesterase". *Journal of the American Chemical Society* **115**(25):12173-12174.

Chen, C.S.Y., White, A., Love, J., Murphy, J.R., and Ringe, D. 2000. "Methyl groups of thymine bases are important for nucleic acid recognition by DtxR". *Biochemistry* **39**(34):10397-10407.

Chou, C.J., Wisedchaisri, G., Monfeli, R.R., Oram, D.M., Holmes, R.K., Hol, W.G.J., and Beeson, C. 2004. "Functional studies of the Mycobacterium tuberculosis iron-dependent regulator". *Journal of Biological Chemistry* **279**(51):53554-53561.

Cornish-Bowden, A. 1995. "Inhibition and Activation of Enzymes". *In* Fundamentals of Enzyme Kinetics. Portland Press, London. 102.

D'Souza V, M., Brown, R.S., Bennett, B., and Holz, R.C. 2005. "Characterization of the active site and insight into the binding mode of the anti-angiogenesis agent fumagillin to the manganese(II)-loaded methionyl aminopeptidase from Escherichia coli". *Journal of Biological Inorganic Chemistry* **10**(1):41-50.

D'Souza, V.M., Bennett, B., Copik, A.J., and Holz, R.C. 2000. "Divalent metal binding properties of the methionyl aminopeptidase from Escherichia coli". *Biochemistry* **39**(13):3817-3826.

Ding, X., Zeng, H., Schiering, N., Ringe, D., and Murphy, J.R. 1996. "Identification of the primary metal ion-activation sites of the diphtheria, tox repressor by X-ray crystallography and site-directed mutational analysis". *Nature Structural Biology* **3**(4):382-387.

Drum, C.L., Yan, S.-Z., Bard, J., Shen, Y.-Q., Lu, D., Soelaiman, S., Grabarek, Z., Bohm, A., and Tang, W.-J. 2002. "Structural basis for the activation of anthrax adenylyl cyclase exotoxin by calmodulin". *Nature* **415**(6870):396-402.

Eisenstadt, E., Fisher, S., Der, C.L., and Silver, S. 1973. "Manganese Transport in Bacillus-Subtilis W23 During Growth and Sporulation". *Journal of Bacteriology* **113**(3):1363-1372.

Fajer, M., Fajer, P.G., and Sale, K.L. in press-a. "Molecular Modeling of Spin Labels". Berliner MHaL, editor. Springer Verlag.

Fajer, P.G. 1994. "Determination of Spin-Label Orientation within the Myosin Head". *Proceedings of the National Academy of Sciences of the United States of America* **91**(3):937-941.

Fajer, P.G., Bennett, R.L.H., Polnaszek, C.F., Fajer, E.A., and Thomas, D.D. 1990a. "General-Method for Multiparameter Fitting of High-Resolution Epr-Spectra Using a Simplex Algorithm". *Journal of Magnetic Resonance* **88**(1):111-125.

Fajer, P.G., Brown, L., and Song, L. in press-b. "Practical Pulsed Dipolar EPR (DEER)". Hemminga M, Berliner L, editors. Springer Verlag.

Fajer, P.G., Fajer, E.A., Matta, J.J., and Thomas, D.D. 1990b. "Effect of Adp on the Orientation of Spin-Labeled Myosin Heads in Muscle-Fibers - a High-Resolution Study with Deuterated Spin Labels". *Biochemistry* **29**(24):5865-5871.

Finney, L.A., and O'Halloran, T.V. 2003. "Transition metal speciation in the cell: Insights from the chemistry of metal ion receptors". *Science* **300**(5621):931-936.

Gasteiger, E., Gattiker, A., Hoogland, C., Ivanyi, I., Appel, R.D., and A., B. 2003. "ExPASy: the proteomics server for in-depth protein knowledge and analysis". *Nucleic Acids Res.* **31**:3784-3788.

Glasfeld, A., Guedon, E., Helmann, J.D., and Brennan, R.G. 2003. "Structure of the manganese-bound manganese transport regulator of Bacillus subtilis". *Nature Structural Biology* **10**(8):652-657.

Golombek, A.P., and Hendrich, M.P. 2003. "Quantitative analysis of dinuclear manganese(II) EPR spectra". *Journal of Magnetic Resonance* **165**(1):33-48.

Golynskiy, M.V., Davis, T.C., Helmann, J.D., and Cohen, S.M. 2005. "Metal-Induced Structural Organization and Stabilization of the Metalloregulatory Protein MntR". *Biochemistry* **44**(9):3380-3389.

Gonick, L., and Smith, W. 1993. "The Cartoon guide to Statistics". Harper Perennial, New York.

Grabski, A., Mehler, M., and Drott, D. 2003. *InNovations* **17**:3-6.

Hemminga, M.A., Dejager, P.A., Marsh, D., and Fajer, P. 1984. "Standard Conditions for the Measurement of Saturation-Transfer Electron-Spin-Resonance Spectra". *Journal of Magnetic Resonance* **59**(1):160-163.

Hoel, P.G., Port, S.C., and Stone, C.J. 1971. "Testing Hypotheses". *In* Introduction to Statictical Theory. Houhgton Mifflin, New York. 52-110.

Humphrey, W., Dalke, A., and Schulten, K. 1996. "VMD: Visual molecular dynamics". *Journal of Molecular Graphics* **14**(1):33-&.

Jakubovics, N.S., and Jenkinson, H.F. 2001. "Out of the iron age: new insights into the critical role of manganese homeostasis in bacteria". *Microbiology-Sgm* **147**:1709-1718.

Jeschke, G., Koch, A., Jonas, U., and Godt, A. 2002. "Direct conversion of EPR dipolar time evolution data to distance distributions". *Journal of Magnetic Resonance* **155**(1):72-82.

Khairy, K., Budil, D., and Fajer, P. 2006. "Nonlinear-least-squares analysis of slow motional regime EPR spectra". *Journal of Magnetic Resonance* **183**(1):152-159.

Khangulov, S.V., Pessiki, P.J., Barynin, V.V., Ash, D.E., and Dismukes, G.C. 1995. "Determination of the Metal-Ion Separation and Energies of the 3 Lowest Electronic States of Dimanganese(Ii,Ii) Complexes and Enzymes - Catalase and Liver Arginase". *Biochemistry* **34**(6):2015-2025.

Klauder, J.R., and Anderson, P.W. 1962. "Spectral Diffusion Decay in Spin Resonance Experiments". *Physical Review* **125**(3):912.

Kliegman, J.I., Griner, S.L., Helmann, J.D., Brennan, R.G., and Glasfeld, A. 2006. "Structural basis for the metal-selective activation of the manganese transport regulator of Bacillus subtilis". *Biochemistry* **45**(11):3493-3505.

Lacy, D.B., Wigelsworth, D.J., Melnyk, R.A., Harrison, S.C., and Collier, R.J. 2004. "Structure of heptameric protective antigen bound to an anthrax toxin receptor: A role for receptor in pH-dependent pore formation". *PNAS* **101**(36):13147-13151.

Lambert, C., Leonard, N., De Bolle, X., and Depiereux, E. 2002. "ESyPred3D: Prediction of proteins 3D structures". *Bioinformatics* **18**(9):1250-1256.

Levitt, M.H. 2001. "Spin dynamics: basics of nuclear magnetic resonance,". John Wiley & Sons, Inc., Chichester, UK.

Li, H.C., and Fajer, P.G. 1994. "Orientational Changes of Troponin-C Associated with Thin Filament Activation". *Biochemistry* **33**(47):14324-14332.

Lieser, S.A., Davis, T.C., Helmann, J.D., and Cohen, S.M. 2003. "DNA-binding and oligomerization studies of the manganese(II) metalloregulatory protein MntR from Bacillus subtilis". *Biochemistry* **42**(43):12634-12642.

Love, J.F. 2003. Mechanism of activation of the diphtheria toxin repressor. *In* Secondary "Mechanism of activation of the diphtheria toxin repressor". Boston University School of Medicine, Boston, MA.

Love, J.F., VanderSpek, J.C., Marin, V., Guerrero, L., Logan, T.M., and Murphy, J.R. 2004. "Genetic and biophysical studies of diphtheria toxin repressor (DtxR) and the hyperactive mutant DtxR(E175K) support a multistep model of activation". *Proceedings of the National Academy of Sciences of the United States of America* **101**(8):2506-2511.

Manabe, Y.C., Hatem, C.L., Kesavan, A.K., Durack, J., and Murphy, J.R. 2005. "Both Corynebacterium diphtheriae DtxR(E175K) and Mycobacterium tuberculosis

IdeR(D177K) Are Dominant Positive Repressors of IdeR-Regulated Genes in M. tuberculosis". *Infect. Immun.* **73**(9):5988-5994.

Marin, V. 2005. Domain-domain Interactions on the Pathway of Activation of Diphtheria Toxin Repressor Protein (DtxR). *In* Secondary "Domain-domain Interactions on the Pathway of Activation of Diphtheria Toxin Repressor Protein (DtxR)". Florida State University, Tallahassee.

Marin, V., Semavina, M., Sen, K.I., Love, J.F., Guerrero, L.R., Caspar, D.L.D., Murphy, J.R., and Logan, T.M. 2003. "Interdomain interactions are required for repressor function in diphtheria toxin repressor". *Biophysical Journal* **84**(2):496A-496A.

McConnell, H.M. 1958. "Reaction Rates by Nuclear Magnetic Resonance". *Journal of Chemical Physics* **28**(3):430-431.

Metropolis, N., Rosenbluth, A.W., Rosenbluth, M.N., Teller, A.H., and Teller, E. 1953. "Equation of State Calculations by Fast Computing Machines". *Journal of Chemical Physics* **21**(6):1087-1092.

Milov, A.D., Ponomarev, A.B., and Tsvetkov, Y.D. 1984. "Electron Electron Double-Resonance in Electron-Spin Echo - Model Biradical Systems and the Sensitized Photolysis of Decalin". *Chemical Physics Letters* **110**(1):67-72.

Pannier, M., Veit, S., Godt, A., Jeschke, G., and Spiess, H.W. 2000. "Dead-time free measurement of dipole-dipole interactions between electron spins". *Journal of Magnetic Resonance* **142**(2):331-340.

Petosa, C., Collier, R.J., Klimpel, K.R., Leppla, S.H., and Liddington, R.C. 1997. "Crystal structure of the anthrax toxin protective antigen". *Nature* **385**(6619):833-838.

Pohl, E., Holmes, R.K., and Hol, W.G.J. 1998. "Motion of the DNA-binding domain with respect to the core of the diphtheria toxin repressor (DtxR) revealed in the crystal structures of apo- and holo-DtxR". *Journal of Biological Chemistry* **273**(35):22420-22427.

Pohl, E., Holmes, R.K., and Hol, W.G.J. 1999. "Crystal Structure of a Cobalt-activated Diphtheria Toxin Repressor-DNA Complex Reveals a Metal-binding SH3-like Domain". *Journal of Molecular Biology* **292**(3):653-667.

Pohl, E., Qiu, X.Y., Must, L.M., Holmes, R.K., and Hol, W.G.J. 1997. "Comparison of high-resolution structures of the diphtheria toxin repressor in complex with cobalt and zinc at the cation-anion binding site". *Protein Science* **6**(5):1114-1118.

Poyner, R.R., and Reed, G.H. 1992. "Structure of the Bis Divalent-Cation Complex with Phosphonoacetohydroxamate at the Active-Site of Enolase". *Biochemistry* **31**(31):7166-7173.

Qiu, X.Y., Pohl, E., Holmes, R.K., and Hol, W.G.J. 1996. "High-resolution structure of the diphtheria toxin repressor complexed with cobalt and manganese reveals an SH3-like third domain and suggests a possible role of phosphate as co-corepressor". *Biochemistry* **35**(38):12292-12302.

Que, Q., and Helmann, J.D. 2000. "Manganese homeostasis in Bacillus subtilis is regulated by MntR, a bifunctional regulator related to the diphtheria toxin repressor family of proteins". *Molecular Microbiology* **35**(6):1454-1468.

Rangachari, V., Guerrero, L., Bienkienwicz, E.A., Love, J.F., Murphy, J., and Logan, T.M. 2004. "Sequence of metal binding and conformational ordering leading to diphtheria toxin repressor (DtxR) activation". *Biophysical Journal* **86**(1):617A-617A.

Ratledge, C., and Dover, L.G. 2000. "Iron metabolism in pathogenic bacteria". *Annual Review of Microbiology* **54**:881-941.

Reczkowski, R.S., and Ash, D.E. 1992. "Epr Evidence for Binuclear Mn(Ii) Centers in Rat-Liver Arginase". *Journal of the American Chemical Society* **114**(27):10992-10994.

Reiter, T.A., Reiter, N.J., and Rusnak, F. 2002. "Mn2+ is a native metal ion activator for bacteriophage lambda protein phosphatase". *Biochemistry* **41**(51):15404-15409.

Sale, K., Sar, C., Sharp, K.A., Hideg, K., and Fajer, P.G. 2002. "Structural determination of spin label immobilization and orientation: A Monte Carlo minimization approach". *Journal of Magnetic Resonance* **156**(1):104-112.

Sale, K., Song, L.K., Liu, Y.S., Perozo, E., and Fajer, P. 2005. "Explicit treatment of spin labels in modeling of distance constraints from dipolar EPR and DEER". *Journal of the American Chemical Society* **127**(26):9334-9335.

Schiering, N., Tao, X., Zeng, H.Y., Murphy, J.R., Petsko, G.A., and Ringe, D. 1995. "Structures of the Apo-Activated and the Metal Ion-Activated Forms of the Diphtheria Tox Repressor from Corynebacterium-Diphtheriae". *Proceedings of the National Academy of Sciences of the United States of America* **92**(21):9843-9850.

Schmitt, M.P. 2002. "Analysis of a DtxR-like metalloregulatory protein, MntR, from Corynebacterium diphtheriae that controls expression of an ABC metal transporter by an Mn2+-dependent mechanism". *Journal of Bacteriology* **184**(24):6882-6892.

Schweiger, A., and Jeschke, G. 2001. "Principles of pulse electron paramagnetic resonance spectroscopy". Oxford University Press, Oxford.

Semavina, M., Beckett, D., and Logan, T.M. 2006. "Metal-Linked Dimerization in the Iron-Dependent Regulator from Mycobacterium tuberculosis". *Biochemistry* **45**(41):12480-12490.

Sen, K.I., Sienkiewicz, A., Love, J.F., vanderSpek, J.C., Fajer, P.G., and Logan, T.M. 2006. "Mn(II) binding by the anthracis repressor from Bacillus anthracis". *Biochemistry* **45**(13):4295-4303.

Sienkiewicz, A., Ferreira, A.M.D., Danner, B., and Scholes, C.P. 1999. "Dielectric resonator-based flow and stopped-flow EPR with rapid field scanning: A methodology for increasing kinetic information". *Journal of Magnetic Resonance* **136**(2):137-142.

Smith, T., McCracken, J., Shin, Y.K., and DeWitt, D. 2000. "Arachidonic acid and nonsteroidal anti-inflammatory drugs induce conformational changes in the human prostaglandin endoperoxide H-2 synthase-2 (cyclooxygenase-2)". *Journal of Biological Chemistry* **275**(51):40407-40415.

Song, L. 2005. Conformation of Troponin and Myosin in Muscle Contraction. *In* Secondary "Conformation of Troponin and Myosin in Muscle Contraction". Florida State University, Tallahassee.

Spiering, M.M., Ringer, D., Murphy, J.R., and Marletta, M.A. 2003. "Metal stoichiometry and functional studies of the diphtheria toxin repressor". *Proceedings of the National Academy of Sciences of the United States of America* **100**(7):3808-3813.

Sun, L., vanderSpek, J., and Murphy, J.R. 1998. "Isolation and characterization of iron-independent positive dominant mutants of the diphtheria toxin repressor DtxR". *Proceedings of the National Academy of Sciences of the United States of America* **95**(25):14985-14990.

Szczesna, D., and Fajer, P.G. 1995. "The Tropomyosin Domain Is Flexible and Disordered in Reconstituted Thin-Filaments". *Biochemistry* **34**(11):3614-3620.

Tao, X., Boyd, J., and Murphy, J.R. 1992. "Specific Binding of the Diphtheria Tox Regulatory Element Dtxr to the Tox Operator Requires Divalent Heavy-Metal Ions and a 9-Base-Pair Interrupted Palindromic Sequence". *Proceedings of the National Academy of Sciences of the United States of America* **89**(13):5897-5901.

Tao, X., Schiering, N., Zeng, H.Y., Ringe, D., and Murphy, J.R. 1994. "Iron, Dtxr, and the Regulation of Diphtheria-Toxin Expression". *Molecular Microbiology* **14**(2):191-197.

Tao, X., Zeng, H.Y., and Murphy, J.R. 1995. "Transition-Metal Ion Activation of DNA-Binding by the Diphtheria Tox Repressor Requires the Formation of Stable Homodimers". *Proceedings of the National Academy of Sciences of the United States of America* **92**(15):6803-6807.

Twigg, P.D., Parthasarathy, G., Guerrero, L., Logan, T.M., and Caspar, D.L.D. 2001. "Disordered to ordered folding in the regulation of diphtheria toxin repressor activity". *Proceedings of the National Academy of Sciences of the United States of America* **98**(20):11259-11264.

Wieghardt, K., Bossek, U., Nuber, B., Weiss, J., Bonvoisin, J., Corbella, M., Vitols, S.E., and Girerd, J.J. 1988. "Synthesis, Crystal-Structures, Reactivity, and Magnetochemistry of a Series of Binuclear Complexes of Manganese(Ii), Manganese(Iii), and Manganese(Iv) of Biological Relevance - the Crystal-Structure of [L'mniv(Mu-O)3mnivl'](Pf6)2.H2o Containing an Unprecedented Short Mn...Mn Distance of 2.296 As". *Journal of the American Chemical Society* **110**(22):7398-7411.

Wylie, G.P., Rangachari, V., Bienkiewicz, E., and Logan, T.M. 2003. "Structure and thermodynamics of SH3-like C-terminal domain of Diphtheria toxin repressor (DtxR) binding to proline-rich linker: Understanding the role of SH3 domain in activation". *Biophysical Journal* **84**(2):505A-505A.

Wylie, G.P., Rangachari, V., Bienkiewicz, E.A., Marin, V., Bhattacharya, N., Love, J.F., Murphy, J.R., and Logan, T.M. 2005. "Prolylpeptide binding by the prokaryotic SH3-like domain of the diphtheria toxin repressor: A regulatory switch". *Biochemistry* **44**(1):40-51.

BIOGRAPHICAL SKETCH

Kadir Ilker Sen was born in Izmir, Turkey in 1979. He was raised in the city of Ankara, where he recieved his Bachelor of Science degree in physics from Bilkent University in 2001. During his undergraduate study, he participated in an internship at the University of Twente, the Netherlands. Since Fall 2001, he is pursuing doctoral study at Florida State University's Institute of Molecular Biophysics. Dr. Sen will continue his academic career as a postdoctoral associate at Albert Einstein College of Medicine of Yeshiva University.